Electrons and Exotic Ions in Superfluid Helium-4

by

Yiming Xing

M.Sc., Brown University, 2018

B.Sc., University of Science and Technology of China, 2016

A dissertation submitted in partial fulfillment of the requirements for the Degree of Doctor of Philosophy in the Department of Physics at Brown University

PROVIDENCE, RHODE ISLAND

MAY 2023

This dissertation by Yiming Xing is accepted in its present form
by the Department of Physics as satisfying the
dissertation requirement for the degree of Doctor of Philosophy.

Date ____________ ________________________________
Humphrey J. Maris, Advisor

Recommended to the Graduate Council

Date ____________ ________________________________
George M. Seidel, Reader

Date ____________ ________________________________
James M. Valles, Reader

Date ____________ ________________________________
Wei Guo, Reader

Approved by the Graduate Council

Date ____________ ________________________________
Thomas A. Lewis,
Interim Dean of the Graduate School

Curriculum Vitae

Yiming Xing was born in Dec. 1993 in Hebei, China. After receiving his B.Sc. degree at the University of Science and Technology of China, he started his graduate studies in the Department of Physics at Brown University in fall 2016. He earned his M.Sc. degree in 2018.

His scientific publications include:

Y. Xing and H. J. Maris, “Negative Ions Produced in Superfluid Helium by Alpha Particles,” J. Low Temp. Phys. **208**, 435 (2022).

Y. Xing, S. Sirisky, W. Wei, L. N. Cooper, and H. J. Maris, “Experimental Investigation of the Quantum Measurement Process Using Electrons in Superfluid Helium,” J. Low Temp. Phys. **207**, 11 (2022).

Y. Xing and H. J. Maris, “Properties of Few-Electron Bubbles in Superfluid Helium-4,” J. Low Temp. Phys. **202**, 399 (2021).

Y. Xing and H. J. Maris, “Electrons and Exotic Ions in Superfluid Helium-4,” J. Low. Temp. Phys. **201**, 634 (2020).

S. Sirisky, Y. Xing, G. M. Seidel, and H. J. Maris, “Investigation of the Fast Negative Ion in Superfluid Helium-4,” J. Low. Temp. Phys. **201**, 122 (2020).

S. Sirisky, Y. Xing, G. M. Seidel, and H. J. Maris, “Study of Positive Helium Ions in Superfluid Helium-4,” J. Low. Temp. Phys. **201**, 114 (2020).

Z. Wang, A. Wang, S. Wang, Y. Xing, Z. Deng, X. Ma, and H. Ming, "High Optical Efficiency Lensless 2D–3D Convertible Integral Imaging Display Using an Edge-Lit Light Guide Plate," J. Display Technol. **12**, 1706 (2016).

Acknowledgments

First and foremost, I would like to express my sincere gratitude to my advisor, Professor Humphrey Maris. Without his guidance, support, patience and encouragement, this thesis work would not have been possible, especially for me as a student who joined the lab without too much experience in cryogenics.

I would like to thank Professor George Seidel, who was always willing to join the group meetings and give invaluable suggestions on the experiments. I would like to extend my thanks to Professor James Valles for his help and support during my preparation for the final examination and to Professor Wei Guo at Florida State University for many helpful discussions. I am also thankful to all of them for taking the time to read this thesis.

My thanks must be extended to the fellow graduate students in the lab. I would especially like to thank Drs. Stephen Sirisky and Yiming Yang for instructing me in the basic cryogenic techniques and helping me with the experiments. I would also like to convey my thanks to Drs. Wanchun Wei and Zhuolin Xie for their previous studies on the exotic ions. In addition, I would like to thank Wanchun Wei for building the cryostat used for the experiments and sharing his knowledge of cryogenics. I am thankful to Dr. Ambarish Ghosh as well for inspiring discussions on the experiments.

I would like to give my thanks to Mr. Michael Packer and the rest of the JEPIS staff for machining all the experimental parts. I would also like to thank Dr. Thomas Grimsley at RITEC, who helped me on the electronics.

I want to thank all the friends I met at Brown. In particular, I would like to thank my friend Dr. Chang Liu for all the great discussions we had at Yan's Cuisine over these years. Finally, I am deeply grateful to my parents and grandparents. Without their love and support, I could not have done this work.

To my parents and grandparents

Contents

List of Tables

List of Figures

Chapter 1

Introduction

1.1 Properties of Liquid Helium-4

It is well known that liquid helium-4 experiences a phase transition at 2.17 K under saturated vapor pressure (SVP), the so-called lambda transition [1]. This name comes from the divergent behavior of the specific heat near the transition point, as shown in Figure 1.1 [2]. Above the lambda point, liquid helium-4 is in the normal fluid phase (helium I). And below the lambda point, liquid helium-4 is in the superfluid phase (helium II). Helium II has nearly zero viscosity and high thermal conductivity.

It was first proposed by Landau [3][4] that the properties of helium II could be explained in terms of elementary excitations. The dispersion curve for elementary excitations in helium II, which describes the relation between energy and wave number k, is shown in Figure 1.2. In the region close to the origin, the dispersion relation is described by the phonon relation $\epsilon = c\hbar k$, where c is the sound velocity. In the region near the local minimum in energy, the dispersion relation can be described by the equation $\epsilon = \Delta + \frac{\hbar^2 (k-k_0)^2}{2\mu}$. And these excitations are the so-called "rotons." The roton energy gap

Δ and roton effective mass μ at SVP have been measured over a wide temperature range [5][6]. The measured values at low temperatures are: $\Delta = 8.65\,K$ and $\mu = 0.16\,M_{He}$, where M_{He} is the mass of a helium atom. At zero temperature, the helium is in its ground state, and its viscosity is assumed to only arise from the creation of excitations. Landau showed that the fluid velocity must exceed a critical value of $v_c = \dfrac{\Delta}{\hbar k_0} \sim 60\,m/s$ (the so-called Landau critical velocity) for any elementary excitations to be created. This argument explains the superfluidity of helium II[1].

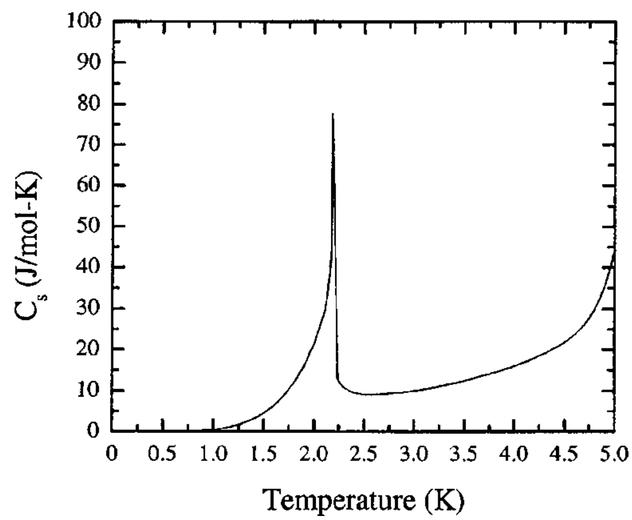

Figure 1.1: The specific heat of liquid helium-4 at SVP, taken from Donnelly and Barenghi [2].

1.2 Negative and Positive Ions in Superfluid Helium-4

[1] However, Landau did not obtain the correct critical velocity because he did not consider the excitation of quantized vortices.

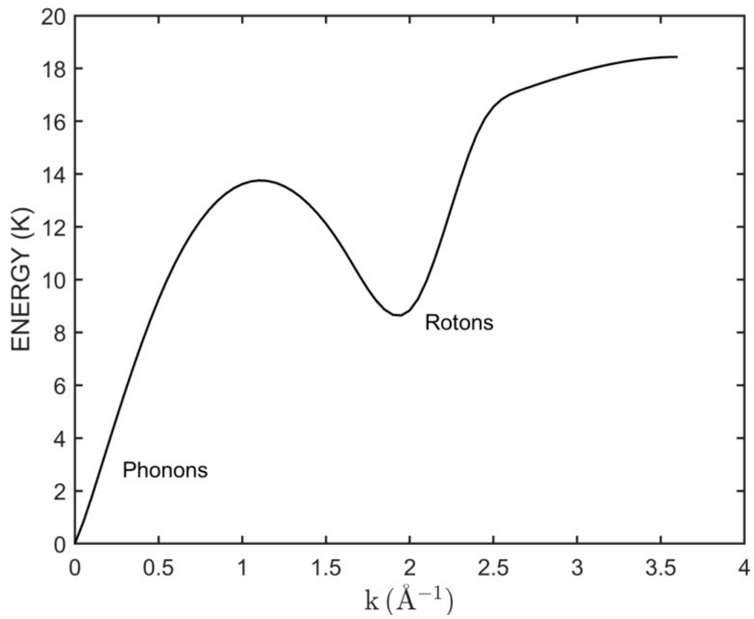

Figure 1.2: The dispersion curve for helium II at low temperatures and at SVP, plotted using data from ref. [2].

An electron in liquid helium repels helium atoms and forces open a spherical cavity. This structure is referred to as an “electron bubble” or a normal electron bubble (NEB) [7][8]. A bubble is formed because the liquid helium appears as an energy barrier of approximately 1 eV to electrons [9]. A simple theory for the total energy E of an electron bubble of radius R is given by taking the sum of the zero-point energy of the electron, the surface energy, and the volume energy

$$E = \frac{h^2}{8m_e R^2} + 4\pi R^2 \sigma + \frac{4\pi}{3} R^3 P \tag{1.1}$$

where m_e is the electron mass, σ is the surface tension, and P is the pressure in the liquid. This equation neglects the penetration of the electron wave function into the liquid and the polarization energy. At zero pressure Equation (1.1) gives an equilibrium radius of

$r = \left(\dfrac{h^2}{32\pi m_e \sigma} \right)^{1/4}$, which is about 19 Å. For a positive ion He^+ in liquid helium, Atkins [10] proposed a "snowball" structure. Due to the electrostriction on helium atoms, the He^+ ion in liquid helium forms a solid sphere with a radius of approximately 7 Å. Reif and Meyer [11][12][13], and Schwarz [14] measured the mobilities of both electron bubbles and positive helium ions in liquid helium over a wide temperature range at SVP. These measurements agree well with the theory of roton-limited mobility in superfluid helium by Baym *et al*. [15].

In 1969 Doake and Gribbon [16] observed a new type of negative ion in liquid helium, which has a mobility about six times higher than that of the normal electron bubble. They named this new ion the "fast ion." In the experiment they used an alpha radioactive source (^{210}Po or ^{241}Am) immersed in the liquid to produce ions. The drift velocity of the fast ion and the normal electron bubble were measured by the Cunsolo method [17]. The measured drift velocities as a function of drift field are shown in Figure 1.3. They found that above a critical velocity of approximately 30 m/s, the normal electron bubbles started to nucleate vortex rings and experienced an abrupt decrease in the drift velocity. But the fast ion could reach a velocity of 54 m/s without suffering such a decrease in the velocity.

Soon after the experiments of Doake and Gribbon, Ihas and Sanders performed a series of time-of-flight mobility measurements to investigate negative ions in liquid helium [18][19][20]. By using a tritium β source, they were successful in observing the fast ion. More interestingly, they detected additional types of negative ions by using a glow discharge in the vapor above the liquid, and each of them had a mobility higher than that of the normal electron bubble. They named these ions the "exotic ions." The name "exotic ions" refers to all the negative ions which have a mobility higher than that of the NEB. Ihas and Sanders used the name "intermediate ions" to refer to the ions which have a mobility that is between that of the fast ion and the NEB. Ihas and Sanders measured the mobility of the exotic ions over a temperature range from 0.95 K to 1.10 K. They reported that they found at least 13 different exotic ions in their experiments. In Figure 1.4 we show a data trace from their experiments, which was taken at 1.005 K.

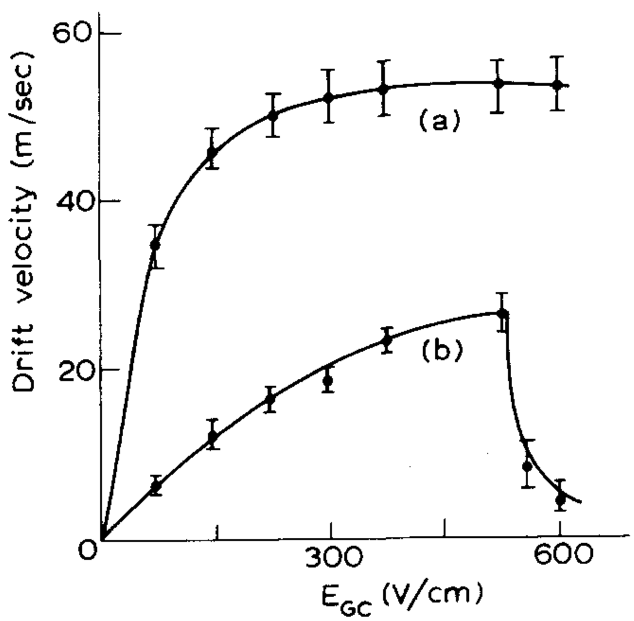

Figure 1.3: The drift velocity of negative ions as a function of drift field at 0.92 K, taken from Doake and Gribbon [16]. (a) The fast ion (b) The normal electron bubble.

Eden and McClintock [21][22][23] also detected the exotic ions with a glow discharge in the vapor. They reported that they observed the fast ion and 13 different intermediate ions. They used a short time-of-flight cell with a drift length of 10 mm in order to achieve a high drift field. They measured the mobility of exotic ions up to a field of 3×10^{3} V/cm. Their results are shown in Figure 1.5. Their results for the fast ion were in agreement with the experiments of Doake and Gribbon. Eden and McClintock found that at least three intermediate ions could nucleate vortex rings above a critical field. And the critical field was found to be lower for the intermediate ion with higher mobility.

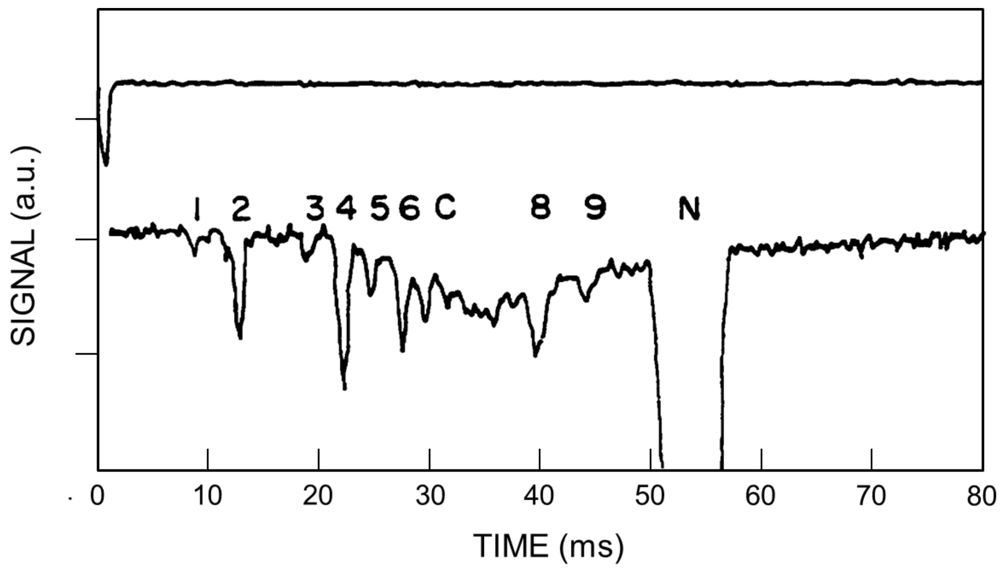

Figure 1.4: A data trace taken from the thesis of Ihas [19]. The temperature was 1.005 K, and the drift field was 30.8 V/cm. The drift length was 6.5 cm. This data trace shows the signals from the exotic ions and NEB.

Most recent experiments were performed by Wei *et al.* [24][25][26][27]. They used tungsten tips or carbon nanotube tips to maintain a plasma discharge in the vapor. Their time-of-flight cell was similar to that of Ihas and Sanders. And stronger exotic ion signals were obtained in the experiments with carbon nanotube tips [25]. At least 18 exotic ions were observed in addition to the NEB. Wei *et al.* measured the mobility of these ions over a temperature range from 0.991 K to 1.16 K. Two representative data traces from their experiments are shown in Figure 1.6.

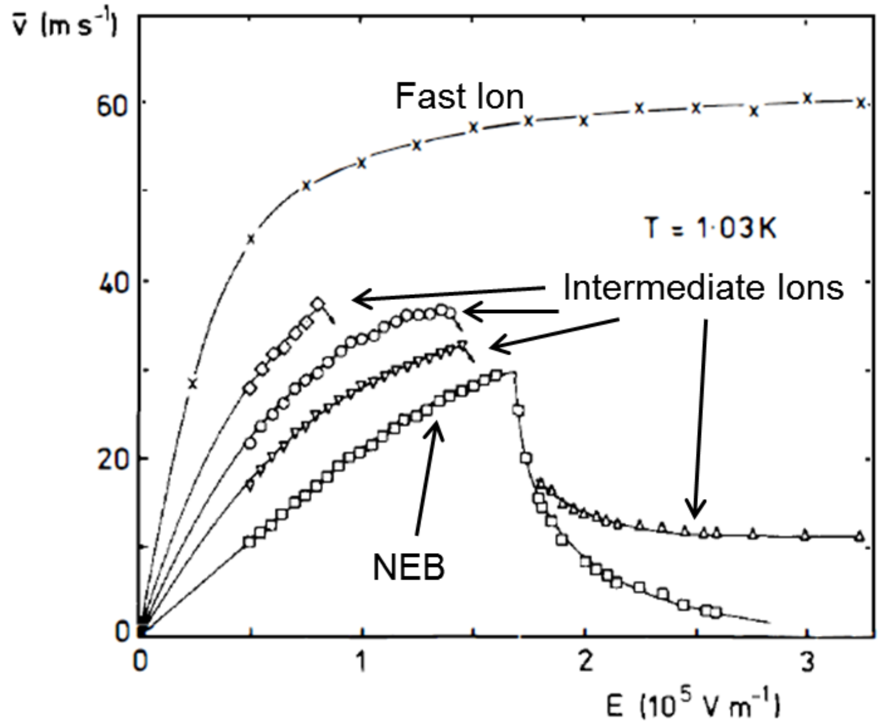

Figure 1.5: Measured mobilities of different types of negative ions as a function of drift field at 1.030 K, adapted from Eden and McClintock [21].

In this thesis I discuss a series of studies that were conducted to investigate different charge carriers in superfluid helium-4. In Chapter 2, numerical simulations about the stability of bubbles containing three and eight electrons will be presented. The pressure ranges within which these bubbles are stable were determined. I will report on experimental results from three different time-of-flight mobility measurements in Chapter 3. These include: (1) measurement of the pressure dependence of the fast ion mobility, (2) observation of multiple positive helium ions, and (3) observation of the exotic ions with an americium-241 source. In Chapter 4, I will discuss two different types of continuous background signals observed in mobility measurements: backgrounds A and B. They are of great interest because they come from negative ions that have a continuous distribution of mobility. Finally, experiments performed to study the 1S→1P photo-excitation of electron bubbles using a CO_2 laser will be detailed in Chapter 5.

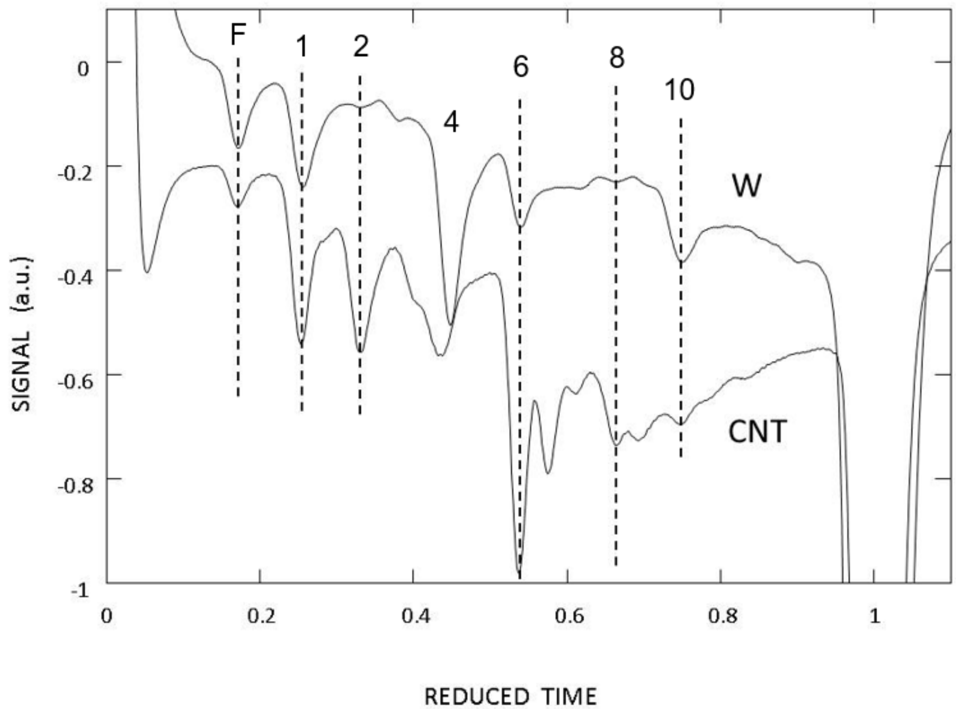

Figure 1.6: Exotic ion data traces taken from Wei *et al.* [24]. (W) data taken with tungsten tips. (CNT) data taken with carbon nanotube tips. Note that the numbering by Wei *et al*. is different from that by Ihas and Sanders.

Chapter 2

Stability of Few-Electron Bubbles in Superfluid Helium-4

Bubbles containing only a small number of electrons are so-called "few-electron bubbles" (FEB). FEBs do not have a spherical shape. The bubble shape and size depend on the number of electrons contained in the bubble and the pressure in the liquid as well. In this chapter a calculation for bubbles containing 3 and 8 electrons will be presented. The pressure range within which these FEBs are stable is determined. The content of this chapter was published as "Properties of Few-Electron Bubbles in Superfluid Helium-4" in the Journal of Low Temperature Physics [28].

2.1 Introduction

Volodin *et al*. [29] first observed the formation of multi-electron bubbles (MEB). They developed instability on the helium liquid-vapor interface by charging the surface with electrons of high surface density. Electrons then left the interface and formed bubbles containing 10^7-10^8 electrons in the liquid. Following their experiment, there have been many other studies on the MEBs [30][31][32][33][34]. An MEB containing a large number Z of electrons could be treated classically, considering that the zero-point energy is much smaller than the Coulomb repulsion energy. In the simplest model, all the electrons are assumed to be localized at the surface of bubble within an infinitesimal layer, and the shape of the MEB is also taken to be nearly spherical. The total energy including the Coulomb energy, the surface energy and the pressure-volume energy is then given as

$$E = \frac{Z^2 e^2}{2\epsilon R} + 4\pi R^2 \sigma + \frac{4\pi}{3} R^3 P \tag{2.1}$$

where ϵ is the dielectric constant of liquid helium, σ is the surface tension, and P is the applied pressure in the liquid. This gives an equilibrium radius

$$R_0 = (\frac{e^2 Z^2}{16\pi\sigma\epsilon})^{1/3} \tag{2.2}$$

The radius is about 0.5 mm when $Z = 10^8$. From Equation (2.1), one can find a negative critical pressure P_c at which the bubble grows without limit.

$$P_c = -(\frac{27\pi\epsilon\sigma^4}{2Z^2 e^2})^{1/3} \tag{2.3}$$

There have been more sophisticated models for the MEB. Shikin [35] proposed a model in which the electrons would form a thin layer with a finite thickness $\delta \ll R$. Salomaa and Williams [36] have used a density functional formalism to calculate the electron density profile in MEBs.

However, if Z is small, the zero-point energy must be considered. Hence, the so-called "few-electron bubbles" do not have spherical shapes. The shape and size of an FEB are subject to the value of Z and the pressure in the liquid. There are two critical pressures for an FEB. The FEB will break into smaller bubbles when the pressure is above the maximum pressure P_{max}. And the bubble will grow without limit when the pressure is below the minimum pressure P_{min}. Dexter and Fowler [37] investigated the stability of bubbles with $Z = 2$. They performed a variational calculation to determine the energy of a spherical bubble containing two electrons. They showed that the calculated energy was larger than the energy of two single electron bubbles and concluded that the two-electron bubble would generally be unstable. However, they did not show whether there could be a process during which the bubble could continuously change its shape to lower the energy and split into two bubbles. By investigating the stability of the two-electron bubble against the $l = 2$ perturbation, Maris [38] later demonstrated that this process could actually happen. His calculation was made by solving the Schrödinger equation with a diffusion algorithm and showed that there was no energy barrier to keep the bubble from splitting into two. The bubble with $Z = 3$ was investigated by Shung and Lin [39] with the assumption that the bubble shape was spherical. The calculations for the stability of FEBs with $Z = 4,6,12$ have also been performed in previous works by Wei *et al.* [40][41]. The shapes of these bubbles were assumed to have certain symmetry, and the critical pressures P_{max} and P_{min} were determined.

FEBs have been experimentally investigated by Yadav *et al.* [42]. Their experiments were performed at 1.5 K. They used sharp tungsten tips or beta radioactive source in the vapor to deposit a layer of electrons on the surface of liquid helium. By causing instability on the surface, a pulse of electrons can be driven to enter the liquid, and these electrons can form different types of bubbles: NEB, MEB or FEB. Then an ultrasonic sound transducer was used to measure the negative critical pressure P_c at which the bubbles become unstable and cause cavitations. It was possible to determine the value of Z by comparing the measured P_c value with the calculated $P_{\min}$ value. The results of their experiments will be discussed later.

2.2 Calculation Method

The calculation method used in the present calculation has been described in the previous works [40][41]. It was based on a simplified version of the Hartree approximation. We summarize the calculation steps as follows:

(a) We start with an initial guess for the size and shape of the bubble. This shape is given by expressing the distance $R(\theta,\phi)$ from the bubble center to the bubble surface in the direction θ,ϕ as

$$R(\theta,\phi)=\sum A_n f_n(\theta,\phi) \tag{2.4}$$

where $\{f_n\}$ are a set of "basis functions," and $\{A_n\}$ are amplitudes. The basis functions can be expressed in terms of spherical harmonics Y_{lm} or equivalent trigonometric functions. The basis functions are chosen as the functions which independently satisfy the symmetry that is proposed for the bubble, and which are constructed out of spherical harmonics using the lowest possible values of l.

(b) We then guess an initial position for each electron and find the potential acting on each electron. This potential is calculated by adding up the Coulomb repulsion with the other electrons localized at their positions.

(c) The ground state wave function of each electron is then found by solving the Schrödinger equation with the imaginary time propagation and the finite difference method. The wave function is set to be zero at the wall of the bubble, i.e., the penetration of the wave function into the liquid is not considered. Allowing for the penetration only results in a small change in the total energy of the bubble[2].

(d) The position of each electron is then changed to be the average position as calculated from the ground state wave function. The positions of the electrons are related by the symmetry proposed for the bubble.

These new positions are then used to recalculate the Coulomb potential and the wave function of each electron. The process is repeated until a convergence is reached. This procedure gives the ground state energy E_g of each electron. The kinetic energy of each electron is given as $\langle K_e \rangle = E_g - \langle V_e \rangle$, where $\langle V_e \rangle$ is the expectation of the Coulomb potential energy. To find the total energy of the bubble, it is necessary to include the surface energy $A\sigma$, where A is the surface area, and the pressure-volume energy PV, where V is the volume. For example, the total energy of the eight-electron bubble is given by

$$E_{tot} = 8\langle K_e \rangle + 4\langle V_e \rangle + PV + \sigma A \tag{2.5}$$

[2] Our estimation shows that this penetration will only decrease the total energy by less than 2%. And note that the effect of penetration becomes less important as the bubble grows larger.

Note that the polarization energy is not included. There are only 28 bonds between 8 electrons, and thus only $4\langle V_e \rangle$ should be included. Then the total energy is calculated for a large number of different values of the amplitudes $\{A_n\}$. The set of amplitudes which give the lowest value of the total energy is found, and the calculation is repeated to find how this energy varies with pressure.

Note that the wave function of each electron typically distributes over a region that is significantly smaller than the bubble size. As a result, it is reasonable to calculating the Coulomb potential acting on one electron by taking each other electrons as located at their average position. The effect of spin was neglected because the overlap of the wave function of one electron with another is very small. The surface tension of helium used in this calculation was taken to be the value measured at very low temperatures, 0.375 $\mathrm{erg \cdot cm^{-2}}$ [43].

2.3 Two-Electron Bubble Revisited (Z=2)

As mentioned in section 2.1, the calculation for whether the two-electron bubble ($Z = 2$) is stable against non-spherical perturbations has been performed [38], but it was only for zero pressure. Here we use the method just described in section 2.2 to investigate the stability of the $Z = 2$ bubble at non-zero pressures. The shape was taken to be

$$R(\theta,\phi) = \frac{1}{3}(R_{\max} + 2R_{\min}) + \frac{1}{3}(R_{max} - R_{\min})(3\cos^2\theta - 1) \tag{2.6}$$

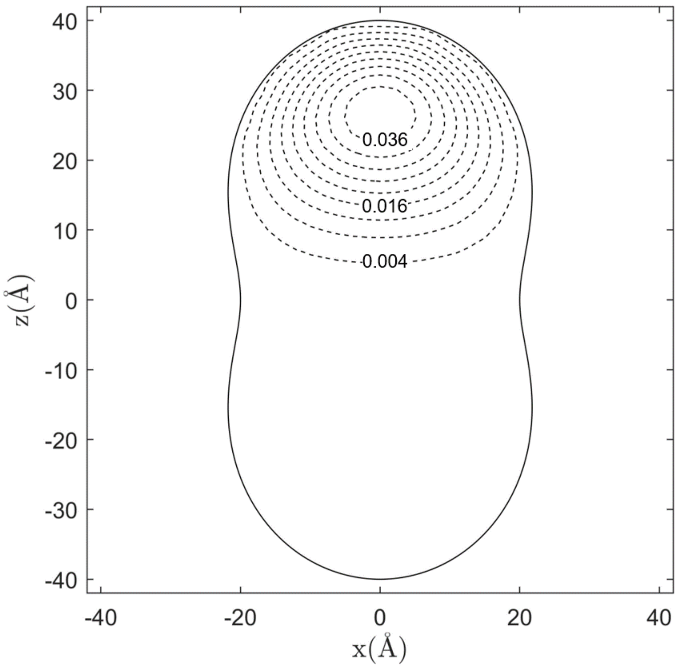

Figure 2.1: Contour plot of the wave function magnitude in the x-z plane ($y = 0$) for a $Z = 2$ bubble with $R_{\max} = 40\ \mathring{A}$ and $R_{\min} = 20\ \mathring{A}$. The pressure is zero. The dashed lines are the contour lines, and the solid line shows the bubble surface.

This shape has two lobes along the z-axis. In Figure 2.1 we show a contour plot for the ground state wave function of one of the electrons in the $Z = 2$ bubble with $R_{max} = 40$ Å and $R_{\min} = 20$ Å. We see that the wave function of the electron is strongly concentrated in the upper lobe and barely overlaps with the other. The total energy of the bubble was calculated for a large range of $R_{\max}$ and $R_{\min}$. No stable local minimum was found, i.e., the lowering of the total energy always led to the $R_{\max}$ and $R_{\min}$ values that resulted in bubble splitting into two or bubble growing without limit. It turned out that this argument was true at any pressure. In Figure 2.2 we show the results for the total energy of the $Z = 2$ bubble at pressure of -0.5 bar as an example. It is clearly shown in the contour plot that the downhill direction of the total energy is towards the $R_{\min} = 0$ axis, i.e., it is energetically favorable for the bubble to split into two.

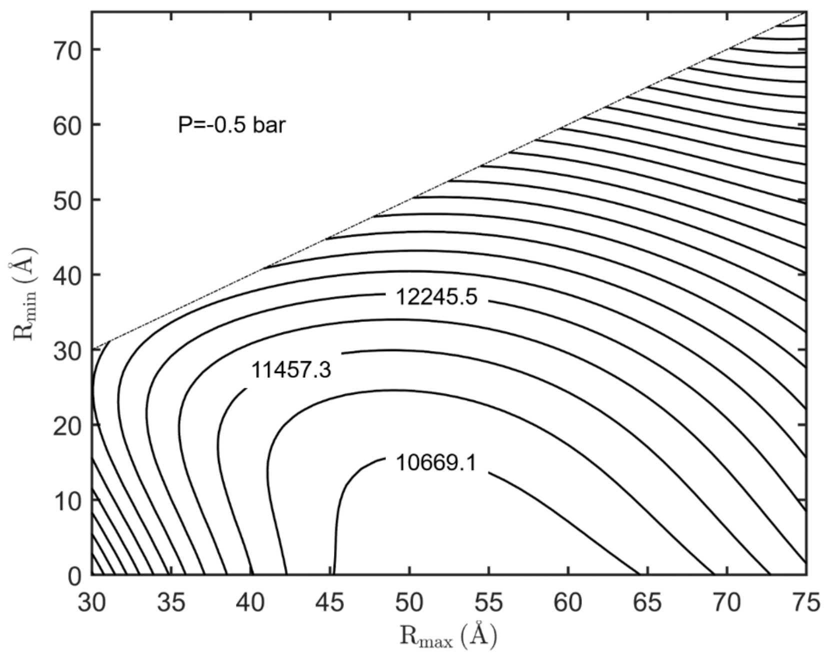

Figure 2.2: Contour plot of the total energy (in 10^{-16} ergs) of the $Z = 2$ bubble as a function of $R_{\max}$ and $R_{\min}$.

2.4 Three-Electron Bubble (Z=3)

For the three-electron ($Z = 3$) bubble, we considered two possible geometries as shown in Figure 2.3. In (a) the three electrons are positioned in a straight line along z-axis. And in (b) the three electrons are positioned at the vertices of an equilateral triangle lying in the x-y plane. One could consider the equilibrium of geometry (a) as follows. The electron at the top experiences the Coulomb repulsion force F_C from the two lower electrons. This force has to be balanced with the surface tension F_{ST}, so this requires the equilibrium condition

$F_{ST} = F_C$. We already know that this condition cannot be met in the $Z = 2$ bubble at any pressure. Thus, it also cannot be met in the $Z = 3$ bubble, considering that the Coulomb repulsion is larger in the case of the $Z = 3$ bubble due to the extra electron. We therefore conclude that geometry (a) is unstable at any pressure.

Now we consider the geometry of (b). It has threefold rotational symmetry with respect to the z-axis and mirror symmetry with respect to the x-y plane. The shape function is given as

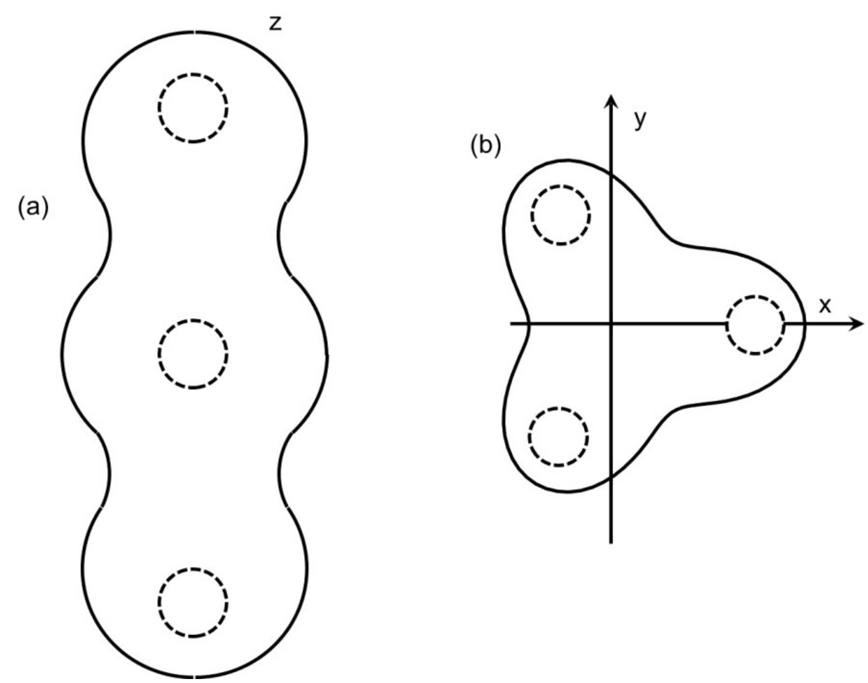

Figure 2.3: Two possible configurations for the $Z = 3$ bubble. The dotted cycles show the approximate electron positions. And the solid curves show the surface of the bubble.

$$R(\theta,\phi) = A_1 + A_2 \sin^3(\theta)\cos(3\phi) + A_3 \sin^2(\theta) \tag{2.7}$$

The values of A_1, A_2 and A_3 that minimize the total energy were found at different pressures. A stable energy minimum can be only found from -0.90 to -0.78 bar. The A_1, A_2 and A_3 values as a function of pressure are shown in Table 2.1 and are also plotted in Figure 2.4. The bubble shapes at several selected pressures are shown in Figure 2.5. As expected, the bubble size grows as the pressure becomes more negative. Below -0.90 bar the bubble grows without limit. This pressure is higher than the critical pressure of a single electron bubble, which is about -1.9 bars. The value of A_1 decreases rapidly as the pressure increases. At pressures above -0.78 bar, the $Z = 3$ bubble becomes unstable against collapsing along the z-axis. This raises an interesting question whether this type of collapse results in a donut-shaped bubble for $Z = 3$, which cannot be described by Equation (2.7).

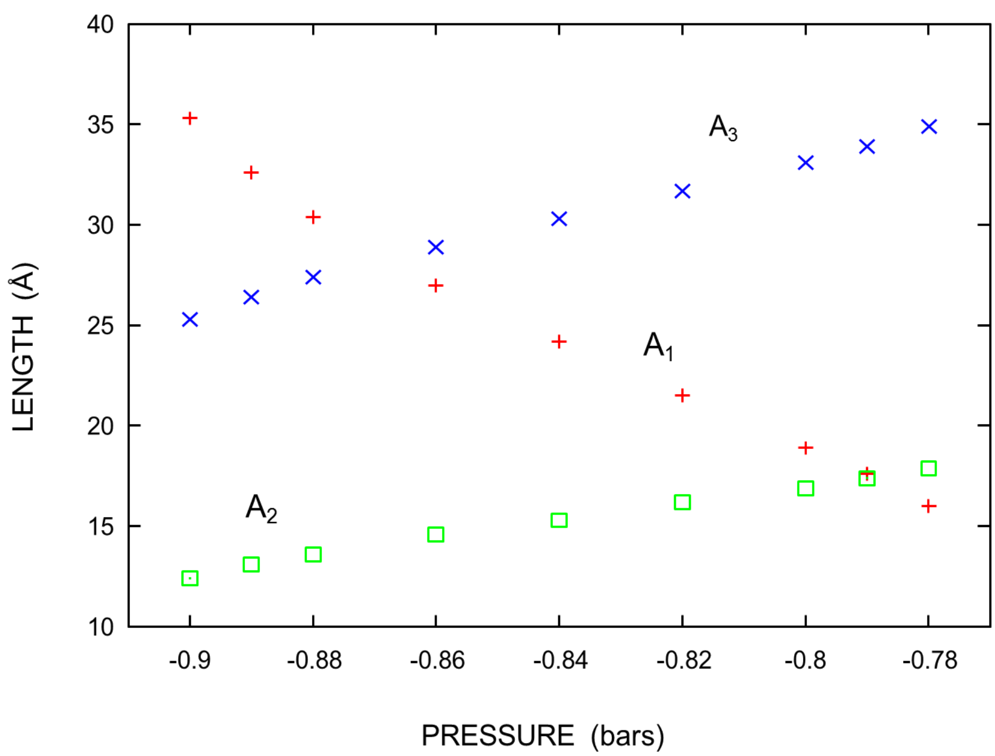

Figure 2.4: The A_1, A_2 and A_3 values for the $Z = 3$ bubble as a function of pressure.

To investigate the possibility for the formation of a donut-shaped $Z = 3$ bubble, we used basis functions different from Equation (2.7). We define a "major radius" $\rho(\phi)$ in the direction ϕ as the distance from the z-axis to the center of the donut cross-section in this direction. At each value of ϕ, we assume the cross-section of the donut to be a circle with a "minor radius" $s(\phi)$ which varies as a function of ϕ. We then consider two choices for the basis functions:

$$\rho(\phi) = A_1 + A_3 \cos(3\phi) \qquad s(\phi) = A_2 + A_3 \cos(3\phi) \tag{2.8}$$

$$\rho(\phi) = A_1 \qquad s(\phi) = A_2 + A_3 \cos(3\phi) \tag{2.9}$$

Pressure (bars)	A_1 (Å)	A_2 (Å)	A_3 (Å)	Energy (10^{-12} erg)
-0.78	16.0	17.9	34.9	1.947
-079	17.6	17.4	33.9	1.943
-0.80	18.9	16.9	33.1	1.940
-0.82	21.5	16.2	31.7	1.932
-0.84	24.2	15.3	30.3	1.923
-0.86	27.0	14.6	28.9	1.914
-0.88	30.4	13.6	27.4	1.904
-0.89	32.6	13.1	26.4	1.898
-0.90	35.3	12.4	25.3	1.892

Table 2.1: The calculated values of A_1, A_2 and A_3, and the total energy for the $Z = 3$ bubble as a function of liquid pressure.

With both basis functions, we calculated the total energy for a large number of values of A_1, A_2 and A_3. Then we searched for a stable local minimum in the total energy and did not find one outside of the pressure range previously investigated. It is possible to choose other basis functions to describe the donut shape. However, it seems unlikely that a stable minimum can exist.

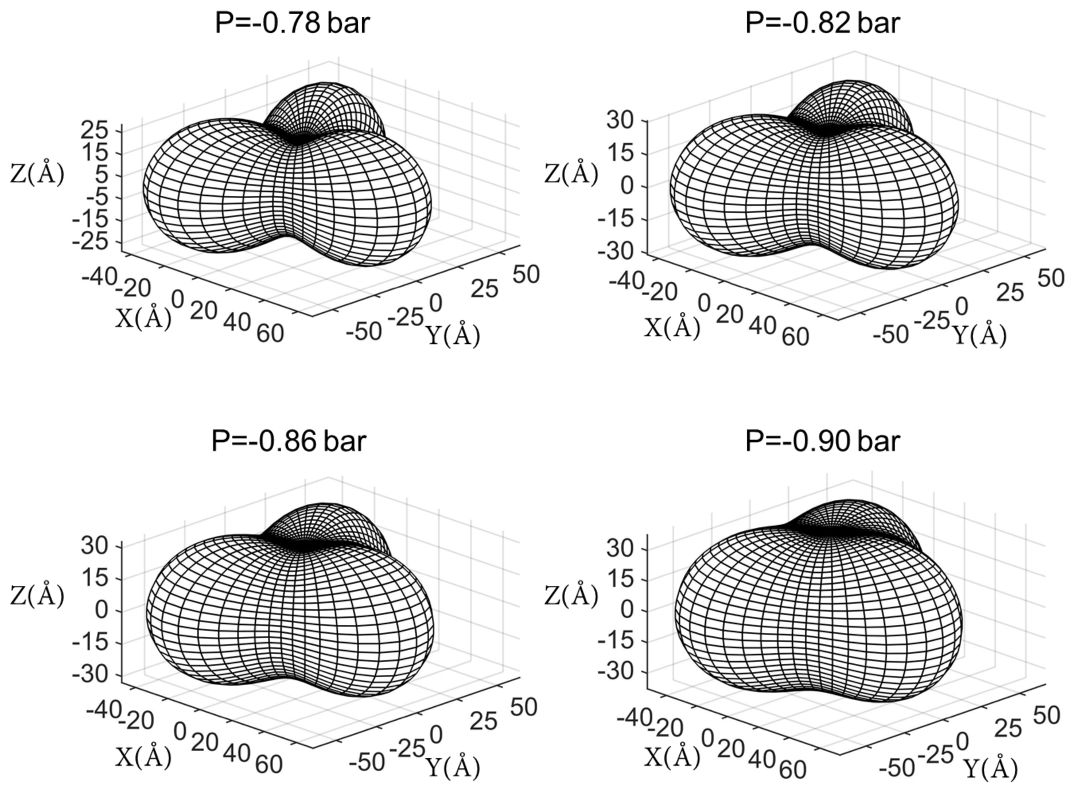

Figure 2.5: Calculated shapes for the $Z = 3$ bubble at different pressures.

2.5 Eight-Electron Bubble (Z=8)

For bubbles containing eight electrons, there are as well two possible geometries to consider. They are drawn in Figure 2.6. The obvious possibility is to position all the electrons at the vertices of a cube. We will call this the "cubic model," as shown in (a) of Figure 2.6. To describe the geometry of the cubic model, we chose the basis function as

$$R(\theta,\phi) = A_1 + A_2\left[\sin^4\theta\left(\cos^4\phi + \sin^4\phi\right) + \cos^4\theta\right] + A_3 \sin^4\theta \cos^2\theta \cos^2\phi \sin^2\phi \quad (2.10)$$

This gives eight lobes with the cubic symmetry. Within the pressure range between -0.42 and 0 bars, stable local energy minimums can be found. The calculated values of A_1, A_2 and A_3, and the total energy at different pressures are given in Table 2.2.

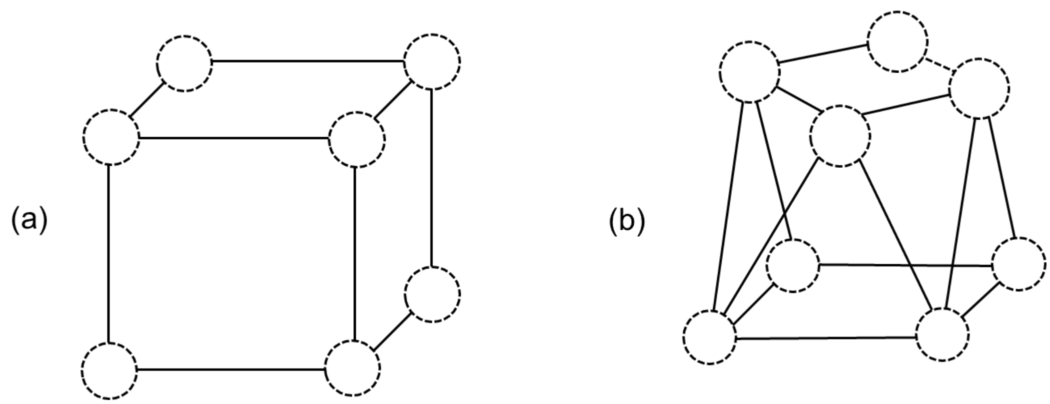

Figure 2.6: Two possible geometries for the $Z = 8$ bubble: (a) Cubic model, and (b) Squares model. Dashed circles represent the approximate positions of electrons.

Another possible geometry was proposed by previous works on the so-called "surface Coulomb problem," which is about finding the least energy configuration of unit point charges confined on a sphere. Results for different number of point charges have been summarized by refs. [44] and [45]. For $Z = 8$, it was found that the least energy configuration was two parallel squares each containing four electrons and being normal to the z-axis. One square is rotated around the z-axis by 45 degrees with respect to the other square, as shown in (b) of Figure 2.6. The total Coulomb energy of this configuration was found to be $\frac{19.675e^2}{R}$ (in cgs units) [44]. We call this geometry the "squares model."

Pressure (bars)	A_1 (Å)	A_2 (Å)	A_3 (Å)	Energy (10^{-12} erg)
0	51.4	-8.4	1665.9	9.547
-0.05	60.5	-10.3	1425.6	9.475
-0.10	66.5	-11.3	1279.8	9.392
-0.20	77.3	-12.3	1047.6	9.191
-0.30	89.1	-12.1	837.0	8.922
-0.40	109.4	-10.5	588.6	8.517
-0.41	113.4	-10.0	550.8	8.460
-0.42	119.3	-9.3	502.2	8.395

Table 2.2: The calculated values of A_1, A_2 and A_3, and the total energy of the Z=8 bubble with cubic symmetry as a function of the liquid pressure.

The "squares model" has symmetry operations such as rotation by $\pi/2$ around the z-axis and mirror reflection with respect to the x-y plane followed by rotation by $\pi/4$ around the z-axis. The shape function used for investigating the squares model was chosen as

$$R(\theta,\phi) = A_1 + A_2 \sin^4\theta\cos\theta\cos 4\phi + A_3 \sin^4\theta\left(13\cos^3\theta - 3\cos\theta\right)\cos 4\phi \qquad (2.11)$$

We found stable energy minimums within the pressure range from -0.41 bar to 0.13 bar. The calculated values of A_1, A_2 and A_3 are given in Table 2.3. In Figure 2.7 we show the bubble shapes at two selected pressures for both the cubic model and the squares model.

Table 2.2 and Table 2.3 show that over the pressure range in which a stable minimum in the energy is found, the total energy of the cubic model is ~2 % less than that of the squares model. For the $Z = 8$ bubble, the cubic model appears to be energetically favorable. This is different from what was found for the classical surface charge problem.

Pressure (bars)	A_1 (Å)	A_2 (Å)	A_3 (Å)	Energy (10^{-12} erg)
0.13	70.1	94.3	17.3	10.199
0.10	72.3	88.6	14.2	10.150
0.05	74.9	82.7	11.7	10.059
0	77.4	77.5	10.0	9.960
-0.05	79.9	72.7	8.7	9.853
-0.10	82.6	68.0	7.7	9.736
-0.15	85.5	63.5	6.9	9.607
-0.20	88.8	58.8	6.2	9.465
-0.25	92.7	53.9	5.5	9.305
-0.30	97.6	48.5	4.8	9.122
-0.35	104.3	42.4	4.2	8.906
-0.40	117.0	34.0	3.3	8.627
-0.41	122.8	31.1	3.0	8.554

Table 2.3: The calculated A_1, A_2 and A_3 values, and the total energy for the squares model as a function of pressure.

The number of basis functions was limited to three in the present calculation, which may introduce some error to the results. Two basis functions were used in the previous work [40], and it was found that increasing the number of basis functions from 2 to 3 could only lower the total energy by 0.7% at zero pressure. Using three basis functions may give a similar or even smaller error. For example, increasing the number of functions from 3 to 4 for the cubic model lowers the total energy by only ~0.5% at zero pressure. However, the effect of higher order basis functions quickly increases as the pressure increases, as shown in Figure 2.4. This indicates that limiting the number of basis functions has a larger effect on P_{max} than on P_{min}.

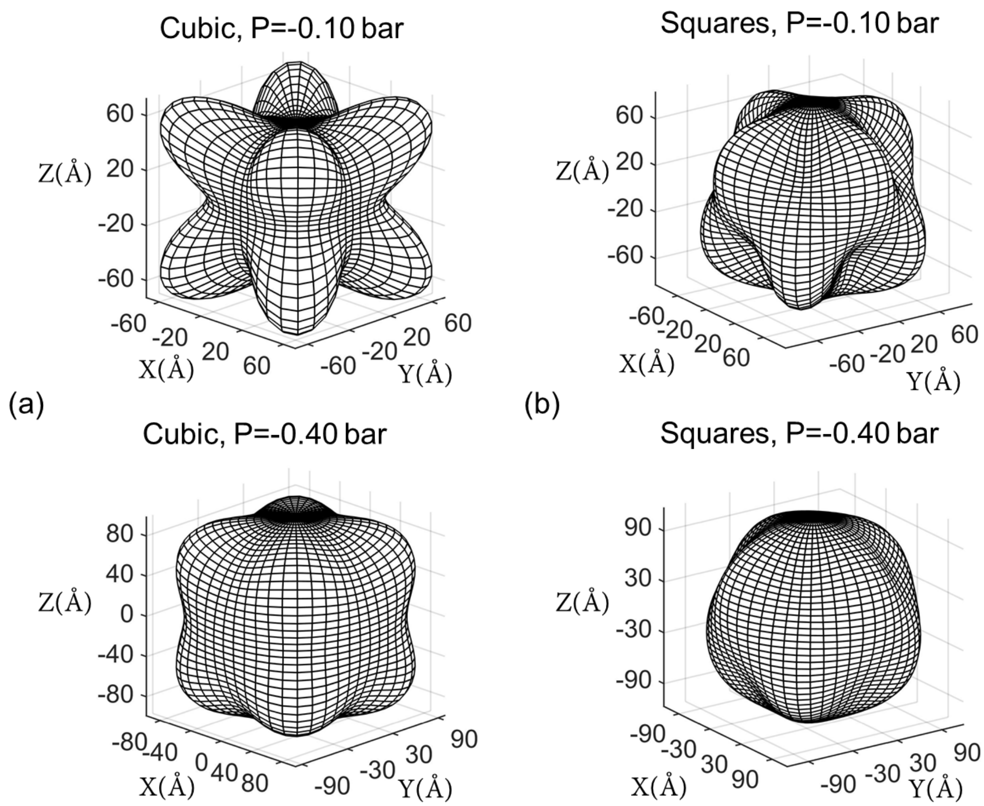

Figure 2.7: Calculated shapes for (a) the cubic model and (b) the squares model at different pressures.

2.6 Discussion

The calculations for the stability of the $Z = 3$ and $Z = 8$ bubbles have been presented in this chapter. The $Z = 3$ bubble was found to be unstable at zero pressure. Thus, one cannot experimentally study the stability of the $Z = 3$ bubble by introducing a pulse of electrons into the liquid at SVP. For the $Z = 8$ bubble, we considered two possible geometries, and the lowest energy was found with the cubic model. A summary of the results is shown in Table 2.4. The calculations reported in this chapter are for zero temperature. At finite temperatures, the surface tension of the liquid will be smaller, and there will be thermal fluctuations. Note that at a low temperature such as 1.5 K, the surface tension is only down a few percent, and the thermal energy scale $k_B T$ is very small compared to the total energy of the bubble.

Z	P_{max} (bars)	P_{min} (bars)	P_c from Eqn. 2.3 (bars)
3	-0.78	-0.90	-0.75
4	-0.45	-0.77	-0.62
6	0.0	-0.60	-0.47
8	0.0	-0.42	-0.39
12	0.5	-0.32	-0.30

Table 2.4: Summary of the results including those for Z =4, 6 and 12 from ref. [40]. P_{max} is the pressure above which the bubble breaks into parts each containing some of the electrons. P_{min} is the pressure at which the bubble begins to grow without limit. P_c is the pressure calculated from Eqn. (2.3) with $\sigma = 0.375$ erg cm^{-2} and $\epsilon = 1.057$.

Yadav *et al*. [42] reported that they observed stable six-electron bubbles and eight-electron bubbles in their cavitation experiments. They determined the number of electrons contained in the bubbles by comparing their measured cavitation threshold pressures with the calculated critical pressures $P_{\min}$ in Table 2.4. Their measurements agree very well with the calculations for $Z = 6$ and $Z = 8$. They found that six-electron bubbles were more easily to be produced by using tips to maintain a corona discharge. And using ultrasound to create a surface instability aided in producing eight-electron bubbles, with a layer of electrons deposited on the liquid surface by using either tungsten tips or beta radioactive source.

Chapter 3

Mobility Measurements of Exotic Ions and Positive Helium Ions

Mobility measurements of negative and positive ions in superfluid helium have been used as a probe to investigate the property of liquid helium and the structure of the ions themselves. In this chapter three different mobility measurements performed by using a time-of-flight method will be presented. These include: (a) pressure dependence of the fast negative ion mobility, (b) observation of multiple positive helium ions, and (c) observation of the exotic ions. Part of the content in this chapter was published as "Investigation of the Fast Negative Ion in Superfluid Helium-4" and "Study of Positive Helium Ions in Superfluid Helium-4" in the Journal of Low Temperature Physics [46][47].

3.1 Cryostat

The design and construction of the cryostat used for the experimental work of this thesis have been thoroughly described in the theses of Dr. Wanchun Wei [26] and Dr. Zhuolin Xie [27]. In this section I only present a brief summary of some key features. The structure of the cryogenic system is shown in Figure 3.1. The cryostat has four different temperature regions: (1) the 1 K region, including the experimental cell and the 1 K pot, (2) the 4 K region at 4 K or higher, including the helium bath, the 4 K shield, as well as the radiation shields above the helium bath, (3) the 77 K region at 77 K or higher, including the liquid nitrogen bath and the 77 K shield, and (4) the room temperature jacket. This design avoids the temperature disturbance to the central region while one transfers the cryogenic liquids into the cryostat. Optical access to the experimental cell is provided by the optical windows on the cell and each tail.

Below 4 K, the cooling power is provided by the 1 K pot. The 1 K pot is a cylindrical vessel with a volume of 221 cm^3. During the experiment, the 1 K pot is continuously filled with liquid helium via a very fine capillary connected to the helium bath. An Edwards roots pump combined with an Alcatel backing pump is used to pump the 1 K pot. They together can provide a cooling power of 31 mW at 1 K. In order to reduce the temperature difference between the 1 K pot and the cell, an OFHC copper plate with a thermal conductivity of 20 W/cm at 1 K is used as the bottom plate of the 1 K pot and as well as the top plate of the cell. The temperature difference between the 1 K pot and the cell is estimated to be only several millikelvins.

The cylindrical experimental cell has a volume of 352 cm^3. It has two separate fill lines to increase the filling speed and also lower the risk of clogs. UHP helium gas is used to fill the cell in order to have pure liquid helium for experiments. The helium gas passes through several thermal anchors and heat exchangers for precooling and condensation. After condensation the liquid helium enters the cell via fine stainless-steel capillaries. Electrical feed-throughs are mounted on the bottom plate of the cell. All the feed-throughs are sealed with indium O-rings. These feed-throughs can provide both high voltage and low voltage inputs. To measure the cell temperature, a germanium thermometer is mounted on a flange on the cell side wall and monitored by a Conductus LTC-20 temperature controller. The cell temperature is controlled by the LTC-20 via a 3.69 kΩ heater mounted on the top of the 1 K pot.

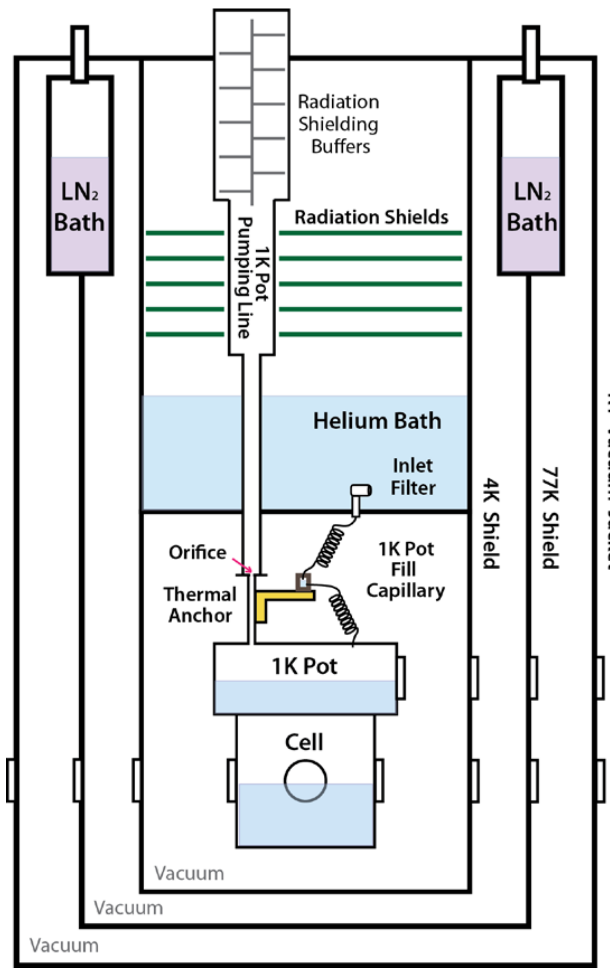

Figure 3.1: Schematic of the cryostat, taken from Dr. Wanchun Wei's thesis [26].

3.2 Time-of-Flight Method

3.2.1 Cell Configuration

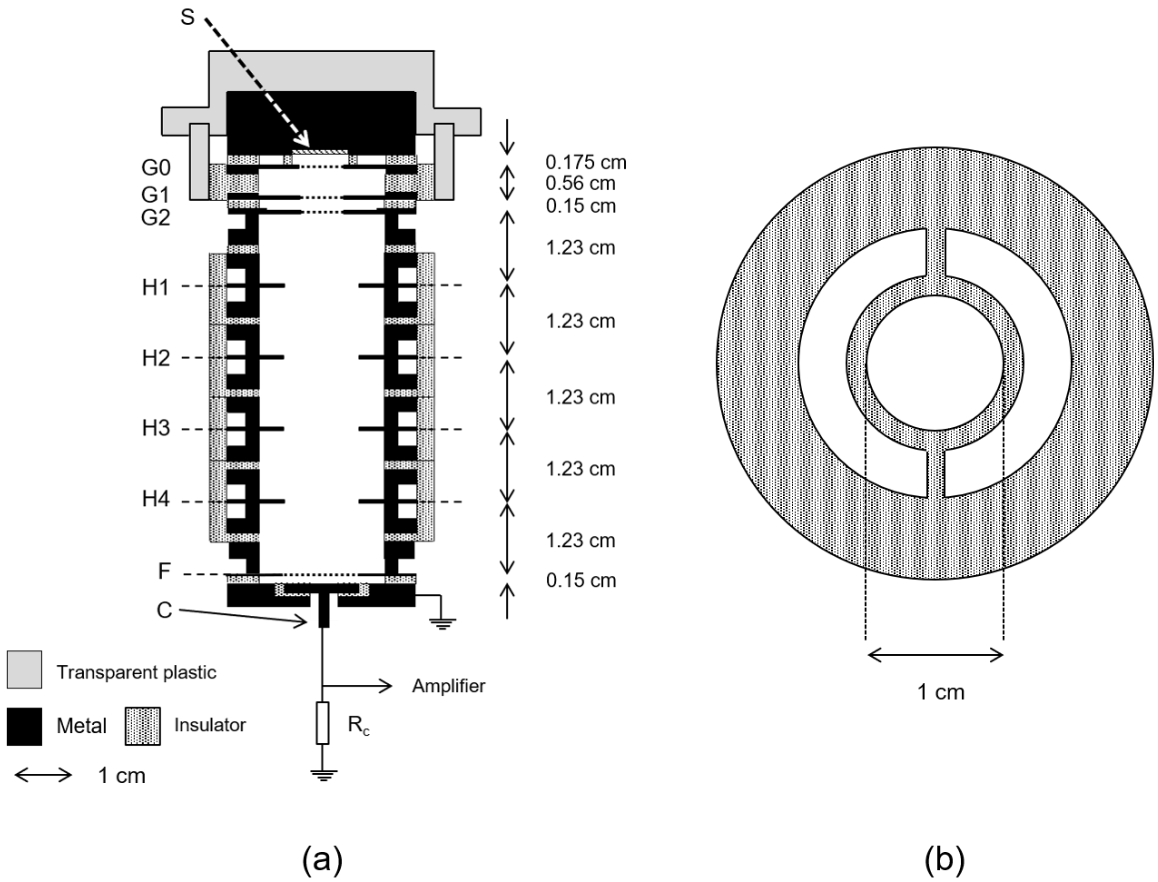

Figure 3.2: (a) Cross section of the time-of-flight cell. The liquid level is between grids G0 and G1. (b) The nylon spacer between the source S and grid G0. This part is used to laterally confine the plasma. Other parts of the cell are described in the text.

The time-of-flight cell was a modified version of that used in the previous experiments of Wei *et al.* [25][26][27] and have been described in refs. [47] and [48]. The details of the cell configuration were slightly different in different experiments. The typical configuration of the cell is shown in Figure 3.2. At the top of the cell, there is a 300 μCi americium-

241 alpha source S. The active area of the source has a diameter of 0.5 cm. The source is separated from the grid G0 by a 0.175 cm thick nylon spacer. In the experiments, liquid helium is usually filled up to a level between the grids G0 and G1. The spacing between G0 and G1 is about 0.56 cm. The energy of the emitted alpha particles is 5.5 MeV. The alpha particles ionize the helium atoms in the vapor both above and below G0. By applying negative dc voltages to the source and G0, a plasma discharge can be maintained in the vapor. The voltage on G0 is more negative with respect to that on G1, and thus electrons from the plasma will be driven towards G1.

The grids G1 and G2 serve as two gate grids, which are separated by a 0.15 cm thick nylon spacer. Grids G0, G1 and G2 were constructed by spot-welding wire grids onto 0.05 cm thick metal ring disks. The wire grids on G0, G1 and G2 have a density of 70 wires per inch and are made of nickel. The dc voltage on G1 is more positive with respect to the voltage on G2 so that electrons cannot pass through G2. Applying a negative voltage pulse to G0 and G1 can make a pulse of electrons pass through G2, and then electrons will move towards the collector C under the influence of the drift field between G2 and the Frisch grid F. Four homogenizer plates H1-H4 are positioned in order to help make the drift field as uniform as possible. They are evenly spaced between G2 and F. The total length of the drift region from G2 to F is 6.15 cm. The inner diameter of the Frisch grid and four homogenizers H1-H4 is 1.27 cm. Note that the field becomes more inhomogeneous as the distance from the central vertical axis increases. To make the electrons more concentrated on the central axis and thus experience a uniform field, the grids G0, G1 and G2 are designed to have a smaller diameter of 0.8 cm. Electrons arriving at the metal plate collector C reach the ground via a 2.5 $\mathrm{M\Omega}$ (measured at 1 K) load resistor R_c. In the experiments the voltage across R_c was recorded and averaged over 1000-20000 pulses applied to G0 and G1. The typical repetition rate of the pulse applied to G1 was 10 per second. The effective capacitance of the collector cable combined with R_c typically gives an RC time constant of ~170 μs.

The purpose of including the Frisch grid F is to make sharp signal pulses. Without the Frisch grid, electrons approaching the collector would produce an image charge on it, and the image charge would give rise to a current flowing through the resistor R_c. Using the Frisch grid can efficiently shield the image charge and has the consequence that the measured signal mostly comes from electrons that have already passed the Frisch grid.

After we read the transit time Δt through the drift region from the signal detected at the collector, the mobility can be easily calculated as $\mu = \frac{d}{E \cdot \Delta t}$, where E is the drift field, and d is the length of the drift region.

3.2.2 Electronics and Data Acquisition

The circuit diagram of the electronics used for the experiments is shown in Figure 3.3. Four high voltage power supplies are used to provide the voltages on the source, G0, G1 and G2. For the source, a 12 MΩ resistor is used to limit the discharge current. In the lines for G0 and G1, the resistors of 1.2 MΩ are used to protect the power supplies in case any shorts occur. TTL signals are used to trigger the General Radio 1217 pulse generator and the data acquisition device. The gate pulse from the pulse generator is passed to G0 and G1 through capacitors of 0.03 μF. A pair of electrolytic capacitors of 100 μF and a grounding resistor of 5.37 kΩ are installed to protect the pulse generator. The 50 kΩ resistors are used to protect the power supplies for G2 and F. And the two capacitors of 0.005 μF are installed

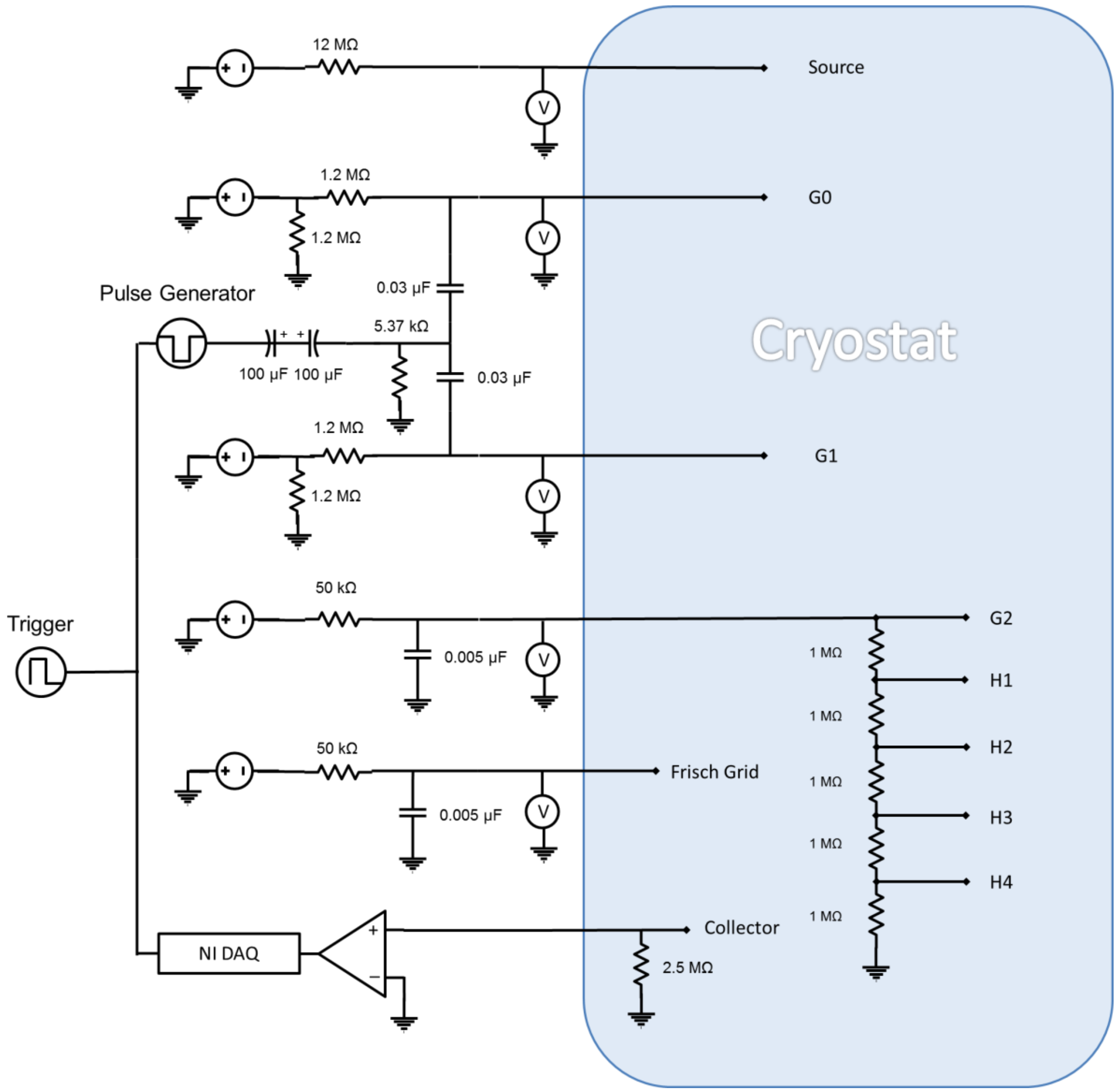

Figure 3.3: Circuit diagram of the electronics used for the time-of-flight cell.

to filter out any possible noise from the power supplies. A Hewlett-Packard low voltage power supply is used to provide the voltage for the Frisch grid. The voltages on the source, G0, G1 and G2 are applied across 1000:1 voltage dividers and then get measured by digital voltmeters. Each voltage divider has a total resistance of 20 MΩ. The voltage on the Frisch grid is measured by an Agilent 34401A multimeter.

The signal on the collector is amplified by a Stanford Research Systems SR560 preamplifier. The gain of the preamplifier is usually set to be on the order of 1000. The preamplifier contains a 30 kHz, -12 dB/oct low pass filter to eliminate high frequency noise. After amplification, the signal is passed to the data acquisition device, which consists of a National Instruments BNC-2120 terminal block and a National Instruments PCIe-6361 card. The sampling rate of the card is typically set to 40000 samples/sec.

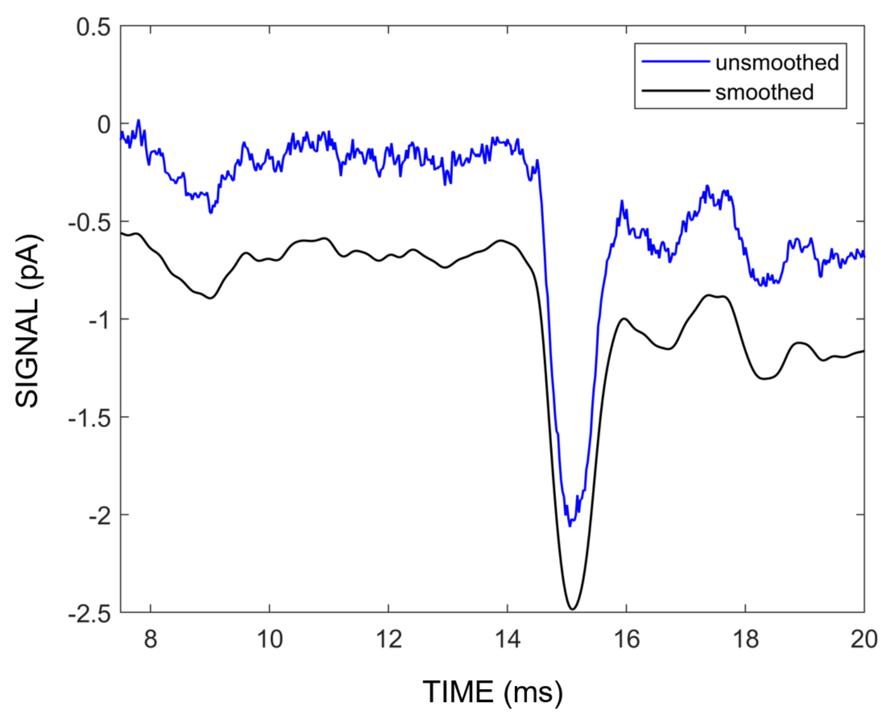

Figure 3.4: An example trace showing the smoothing effect. The blue curve shows the unsmoothed data, and the black curve shows the smoothed data with a width of 0.5 msec. The black curve is offset by 0.5 pA for clarity. Note that the signal becomes significantly less noisy after smoothing without distortion.

To obtain a good signal to noise ratio, 1000-20000 data traces are usually recorded and averaged. To eliminate high frequency ripples, the averaged signal is then further smoothed by convolving it with a cosine-squared function. The argument of the cosine-squared function goes over $-\pi/2$ to $\pi/2$, and the width of the cosine-squared function is manually adjusted to obtain a better smoothing without distortion in signal. For example, if the width is set to 0.5 msec, it equals to $2m+1=21$ adjacent data points for a sampling rate of 40000 samples/sec. The smoothing algorithm is given by the following equation

$$I_{smooth}(k) = \frac{\sum_{n=-m}^{m} \cos^2(n \cdot \pi / 2m) \cdot I(k+n)}{\sum_{n=-m}^{m} \cos^2(n \cdot \pi / 2m)} \tag{3.1}$$

where I_{smooth} is the smoothed data point, and I is unsmoothed data point. In Figure 3.4 we show an example of the smoothing with a width of 0.5 msec.

3.3 Pressure Dependence of the Fast Negative Ion Mobility

3.3.1 Introduction

As previously discussed in Chapter 1, there have been at least 19 different negative ions observed in liquid helium [16][18][19][21][24][25]. Only the structure of the normal electron bubble is fully understood. The structure of the other 18 exotic ions is still an open question. The exotic ion with the highest mobility is referred to as the “fast ion,” which was first discovered by Doake and Gribbon [16]. Only two properties of the exotic ions have been studied so far:

(1) The ion mobility has been measured over the temperature range from 1 K to about 1.2 K. The exotic ions were generated by a plasma discharge in the vapor above the liquid. It is difficult to maintain a stable plasma above 1.2 K because the vapor density significantly increases as the temperature increases. The vapor densities of helium at 1 K and 1.2 K are 1.1×10^{18} cm^{-3} and 5.9×10^{18} cm^{-3}, respectively. And the heat dissipation from the plasma limits the lowest temperature one can reach. The mobility varies with temperature as $\mu_n \propto \exp(\Delta_n / k_B T) / R_n^{\,2}$, where n denotes a particular exotic ion. The parameter Δ_n was found to be different for different ions [20][25], but was always fairly close to the roton energy gap of 8.6 K. This is consistent with the theory that the ion mobility at 1 K is mainly limited by the roton scattering [15]. The radius R_n of different ions ranged from 7.5 Å to 18.9 Å [25].

(2) The critical velocity at which the ion nucleates a vortex ring was measured by Eden and McClintock [21][22][23]. The critical velocities of the intermediate ions[3] were measured to be higher than that of the normal ion. It was found that the fast ion never became trapped on a vortex ring.

From these reports it is not clear whether the fast ion is simply the exotic ion that has the highest mobility or whether it is an ion that has a different structure from the other exotic ions. In favor of the latter view we note that in the experiment of Doake and Gribbon [16] a radioactive α source in the liquid instead of a plasma in the vapor was used to generate ions, and only the fast ion and the NEB were observed. In another experiment, it was found

[3] As mentioned in Chapter 1, the name "intermediate ions" refers to the negative ions which have a mobility between that of the fast ion and the NEB.

that when negative ions were generated by means of a sharp tip immersed in the liquid, rather than a tip in the vapor, only the fast ion and the NEB were seen [49].

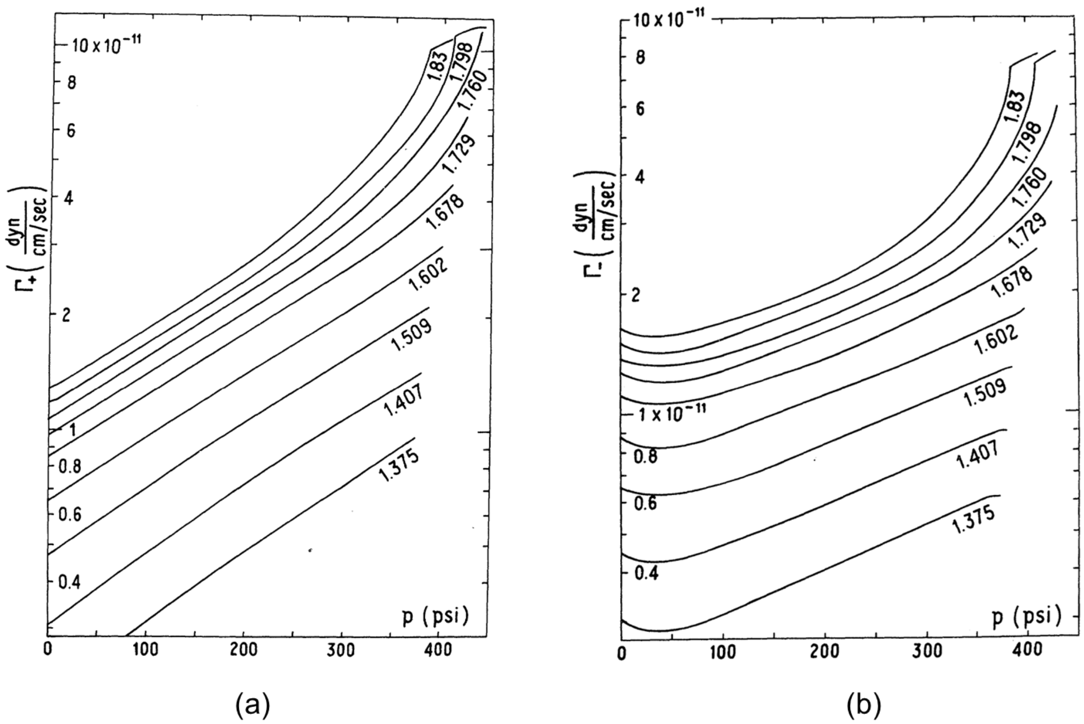

Figure 3.5: Pressure dependences of mobility for (a) the positive helium ion, and (b) the normal electron bubble. The curves are labelled by the temperature. The friction coefficients $\Gamma_{\pm}$ are defined as $e/\mu_{\pm}$, where e is the electric charge. This figure is taken from Brody [50].

To add to the information about the exotic ions, we report here measurements of the variation of the fast ion mobility with liquid pressure. The mobility μ varies approximately as $\mu \propto \exp(\Delta/kT)/R^2$. The pressure dependence measurement may provide information about how the ion radius changes with pressure, i.e., how the ion structure changes with pressure.

The pressure dependences of the mobility of both the normal electron bubble and the positive helium ion have been measured by Brody [50] over a temperature range from 1.375 to 1.83 K. Brody used a time-of-flight device with a drift distance of 5.39 cm. A radioactive source immersed in liquid was used to produce electrons and helium ions by ionizing the helium atoms. The measurements were made at a drift field of 100 V/cm. His results are shown in Figure 3.5. Obviously, the NEB mobility μ_- and the positive helium ion mobility μ_+ have different pressure dependences. This is not a surprise because the structure of positive helium ions is different from that of the NEB. Positive helium ions form solid "snowballs" in liquid helium, as proposed by Atkins [10].

3.3.2 Experiments

The time-of-flight cell used in the experiment was as described in the section 3.2. The alpha source was immersed in the liquid. Measurements were made with a drift field of 65 V/cm. The experimental cell was not designed for work at high pressure, and so we had to limit the pressure range to less than 6 bars. We were able to detect strong signals from the NEB and from positive helium ions. The signal from fast ions was smaller by a factor of about 10. We were unable to detect any signal from the intermediate ions. For the measurements of the normal electron bubble and the fast ion, the 0.175 cm thick nylon spacer between the source and G0 was replaced by a 0.15 cm thick nylon spacer.

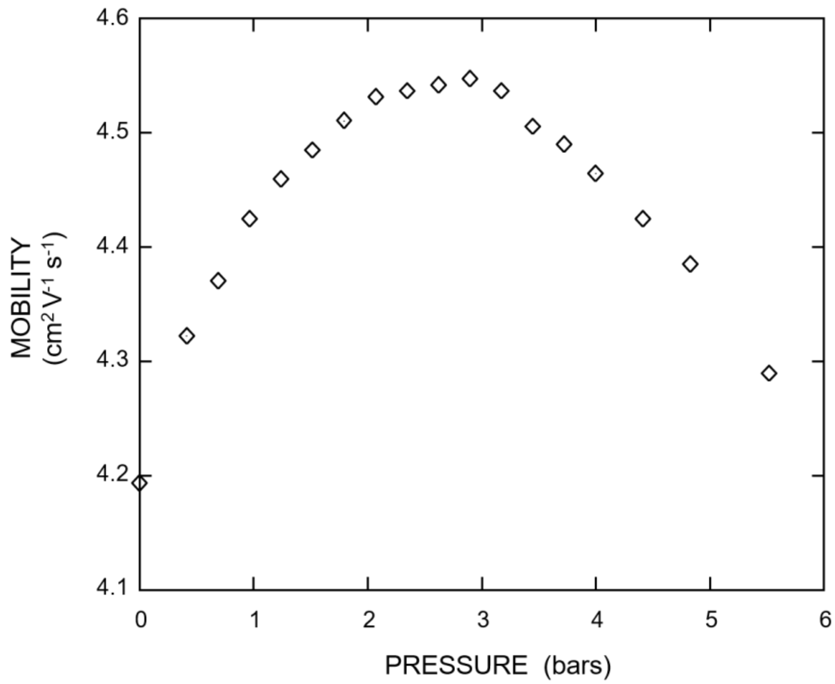

Figure 3.6: Mobility data of the normal electron bubble (NEB) at 0.987 K as a function of pressure.

In Figure 3.6, we plot the mobility of the NEB as a function of pressure. The temperature is 0.987 K. Figure 3.7 shows the mobility of the positive helium ion as a function of pressure, also at 0.987 K. The results in these figures show the same general behavior as that has been found by Brody at higher temperatures [50], i.e., the mobility of the NEB first increases when the pressure is increased and then decreases, while the mobility of the positive ion decreases monotonically as the pressure increases. One can understand the results for the NEB by noting that the mobility μ_{NEB} should vary as

$$\mu_{NEB} = \frac{e}{4\pi R^2 D_{NEB}} \tag{3.2}$$

where D_{NEB} is the drag exerted by rotons on the ion surface per unit area and unit velocity, and R is the radius of the bubble. At temperatures around 1 K, the drag will be proportional to the roton number density and thus can be described by

$$D_{NEB} \propto \exp\left(-\Delta / kT\right) \tag{3.3}$$

where Δ is the roton energy gap. Since Δ decreases with increasing pressure[4], the drag D_{NEB} increases with pressure.

At the same time, the radius R decreases as the pressure increases. When the pressure is small, the rate of decrease in R is sufficiently high so that the mobility increases despite the increase in D_{NEB}. However, as the pressure increases, the bubble becomes less compressible while D_{NEB} continues to increase, and so the mobility decreases. Recall Equation (1.1) for the energy of the NEB

$$E = \frac{h^2}{8m_e R^2} + 4\pi R^2 \sigma + \frac{4\pi}{3} R^3 P \tag{3.4}$$

where σ is the surface tension (0.3677 erg cm^{-2} at 1 K), and m_e is the electron mass. From this equation one can solve for the bubble radius. The bubble radius as a function of pressure is shown as the solid curve in Figure 3.8. Using this result combined with the measured mobility data gives the drag coefficient D_{NEB} shown in Figure 3.8 as the dashed curve.

[4] See, for example, O. W. Dietrich, E. H. Graf, C. H. Huang, and L. Passell, Phys. Rev. A **5**, 1377 (1972).

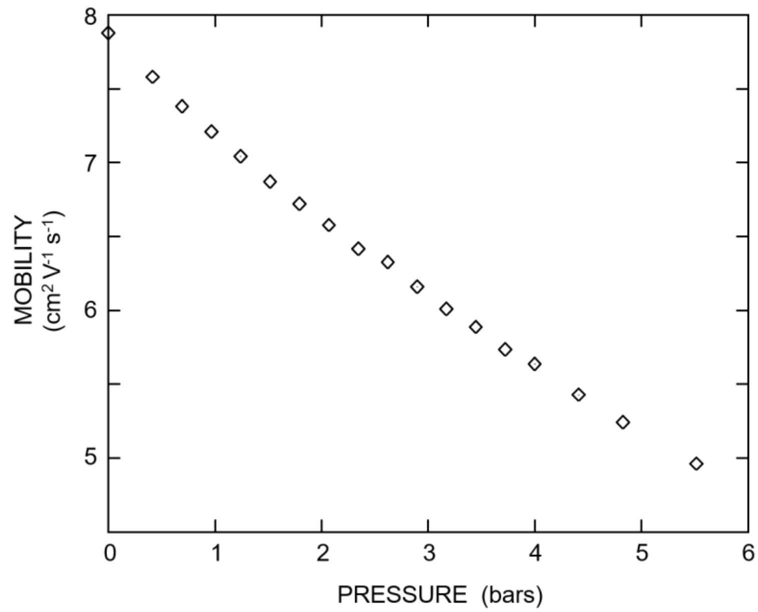

Figure 3.7: Mobility data of the positive helium ion at 0.987 K as s function of pressure.

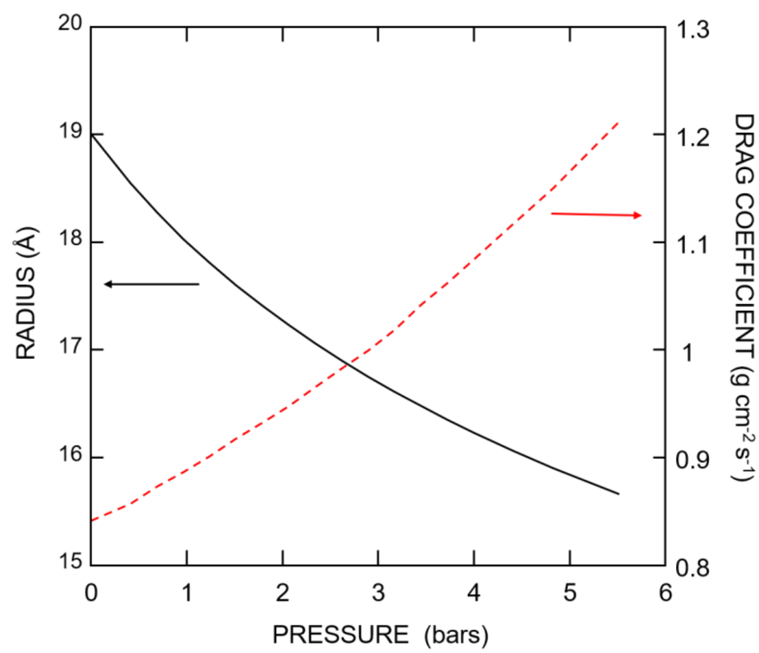

Figure 3.8: Solid curve shows the calculated radius R of the normal electron bubble using Equation (3.4). The dashed curve shows the drag coefficient D_{NEB} calculated from the mobility of the normal electron bubble using the procedure described in the text.

In Figure 3.9 we show the measurements of the fast ion mobility μ_{fast}. If the drag coefficient for the fast ion is D_{fast}, then the radius R_{fast} of the fast ion is given by

$$\begin{aligned} R_{fast} &= \sqrt{\frac{e}{4\pi\mu_{fast}D_{fast}}} \\ &= R_{NEB}\sqrt{\frac{\mu_{NEB}D_{NEB}}{\mu_{fast}D_{fast}}} \end{aligned} \tag{3.5}$$

If we assume that the drag coefficient for the fast ion is the same as the coefficient for the NEB, we find the radius of the fast ion to be 7.4 Å with no significant variation with pressure (as shown in Figure 3.10a). However, since the structure of the fast ion is still not known, we cannot be sure that D_{NEB} and D_{fast} are equal.

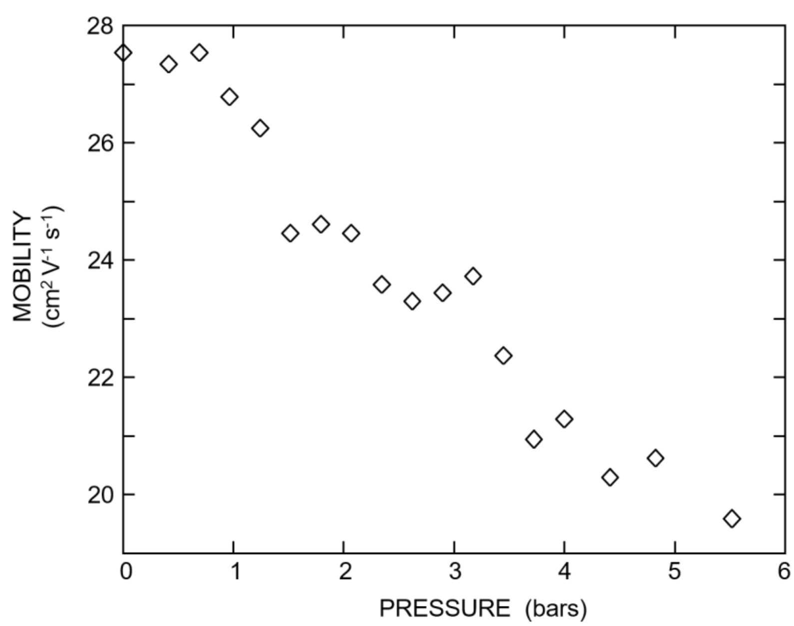

Figure 3.9: Mobility data of the fast ion at 0.987 K as a function of pressure.

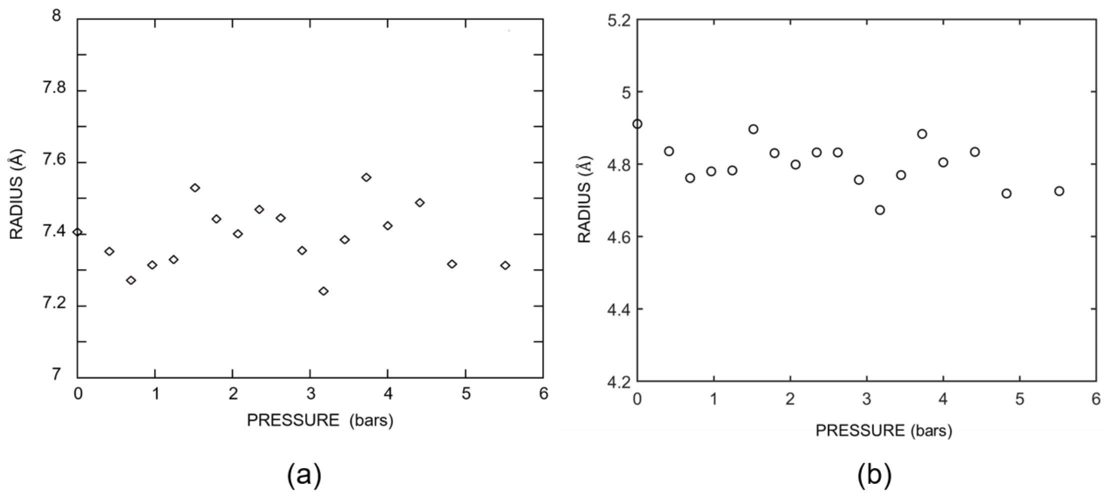

Figure 3.10: Radius of the fast ion calculated as a function of pressure by using the procedures described in the text.

Similarly, if we assume that the drag coefficient for the fast ion is equal to that for the positive ion, then we obtain

$$R_{fast} = R_{He^+}\sqrt{\frac{\mu_{He^+}}{\mu_{fast}}} \tag{3.6}$$

where R_{He^+} and μ_{He^+} are the mobility and radius of the positive ion, respectively. The radius of the positive ion can be calculated as a function of pressure/density using the Atkins' model [10]. As derived by Schwarz [51], the radius R_{He^+} is given by[5]

$$B_1 \ln\left(\frac{\rho_2}{\rho_1}\right) + B_2\left(\rho_2 - \rho_1\right) + B_3(\rho_2^{\ 2} - \rho_1^{\ 2}) = \frac{\beta e^2}{2R_{He^+}^{\ 4}\left(1 + 4\pi\beta\rho_2\right)^2} \tag{3.7}$$

[5] Then we added a constant value to the calculated radii so that the radius at zero pressure equals to 9.18 Å, which is the positive ion radius Baym *et al*. [15] found by fitting their theory to mobility experiments.

where ρ_2 is the liquid density at the melting pressure[6], ρ_1 is the liquid density at a given pressure[7], $\beta = 0.031$, $B_1 = 2.03\times10^9$, $B_2 = -4.23\times10^{10}$, and $B_3 = 1.11\times10^{11}$, all in cgs units. The fast ion radii calculated using Equation (3.6) are shown in Figure 3.10b. The radius is found to be 4.8 Å with no significant variation over the pressure range from 0 to 5.5 bars.

3.3.3 Discussion

The absence of a signal from the intermediate ions in this experiment supports the idea already indicated by previous experiments that the fast ion may have a different structure from the intermediate ions. The fast ion and intermediate ions have both been observed when negative charges enter the liquid from a plasma discharge in helium vapor, but only the fast ion is observed when an alpha particle enters the liquid [16] or when a sharp tip is immersed in the liquid [49]. Although the present experiment does provide new information about the fast ion, the structure of the fast ion is still not fully understood.

The possibility that the fast ion is the $1s2s2p\,^4P$ negative helium ion was considered by Ihas and Sanders [18][19][20] and was rejected because the lifetime is much less than the time for the fast ion to transit the drift cell.

The absence of a significant change in the radius of the fast ion when pressure is varied is not difficult to understand. Assuming that the fast ion is a bubble, in order to have a radius

---

6 Note that the surface tension effect on the melting pressure was considered.

7 The equation of state used by Schwarz is given by $P = A_1(\rho-\rho_0) + A_2(\rho-\rho_0)^2 + A_3(\rho-\rho_0)^3$, where $\rho_0 = 0.14513$, $A_1 = 5.68\times10^8$, $A_2 = 1.11\times10^{10}$, and $A_3 = 7.41\times10^{10}$, all in cgs units.

of 7.4 Å, there must be a very strong bond between the extra electron and whatever forms the core of this ion. As a result, the variation of the bubble size with changes in pressure will be small.

Superfluid helium contains only a very small number of impurities, but one may consider the possibility that the fast ion comes from impurities frozen onto the wall of the cell, such as air components. In the present experiment there is no plasma discharge, and so the impurities cannot be knocked off the wall by collisions with helium atoms with high kinetic energy. It is possible that helium ions or excited helium atoms produced by an alpha particle can diffuse through the liquid and deposit enough energy to make an impurity go off the wall. The alpha particles also produce high energy photons that travel freely through the liquid and deposit energy on the wall. This may also make some impurities go off the wall.

3.4 Observation of Multiple Positive Helium Ions

3.4.1 Introduction

As previously discussed in Chapter 1, electrons in liquid helium were proposed to be trapped in a spherical cavity, the so-called electron bubbles. For the structure of the positive ion in liquid helium, Atkins [10] proposed what has become known as the "snowball" model. He pointed out that the electric field around a positive ion polarizes the neighboring helium atoms and thus produces a pressure sufficiently high to form a solid cluster in the vicinity of the ion. In superfluid helium, the ion mobility is determined by the rate at which the moving ion loses momentum as a result of collisions with the phonons and rotons.

Above a critical velocity, ions can lose momentum as a result of the nucleation of quantized vortices. The mobility of He^+ has been measured over a wide range of temperature and pressure [14][50].

Positive impurity ions are also considered to form snowballs. Ihas and Sanders [52] used a hot tungsten filament that was intrinsically doped with potassium to inject K^+ ions into liquid helium and measured their mobility. Glaberson and Johnson [53][54] developed a technique to introduce various positive impurity ions into liquid helium, and they successfully measured the mobilities of the K^+, Rb^+, Cs^+, Sr^+, Ba^+, and Ca^+ ions. In their experiments, a continuous plasma discharge was maintained in the helium vapor by using a wire electrode. A tungsten filament was coated with a solution/suspension of a chemical compound that contains the positive ion of interest. The filament was heated to introduce the compound into the vapor, and then the positive ions were driven to the mobility measurement cell.

Here we report on a further experimental investigation of positive helium ions in superfluid helium-4. We observed three different positive helium ions with slightly different mobility, and possibly a fourth. As far as we are aware, there was only one previous experiment which indicated that there was probably more than one positive helium ion in liquid helium-4 [27]. A very small signal from an ion with mobility 8 to 10% higher than that of the normal positive helium ion was detected. At the time, it was proposed that this may just be a positive tungsten ion produced from the sharp tungsten tip used to generate the plasma discharge. In the present experiment, an alpha radioactive source, instead of the tungsten tip, is used to maintain the plasma. The configuration of the experimental cell was as described in section 3.2. The liquid level was at approximately 1 mm above G1.

3.4.2 Experiments

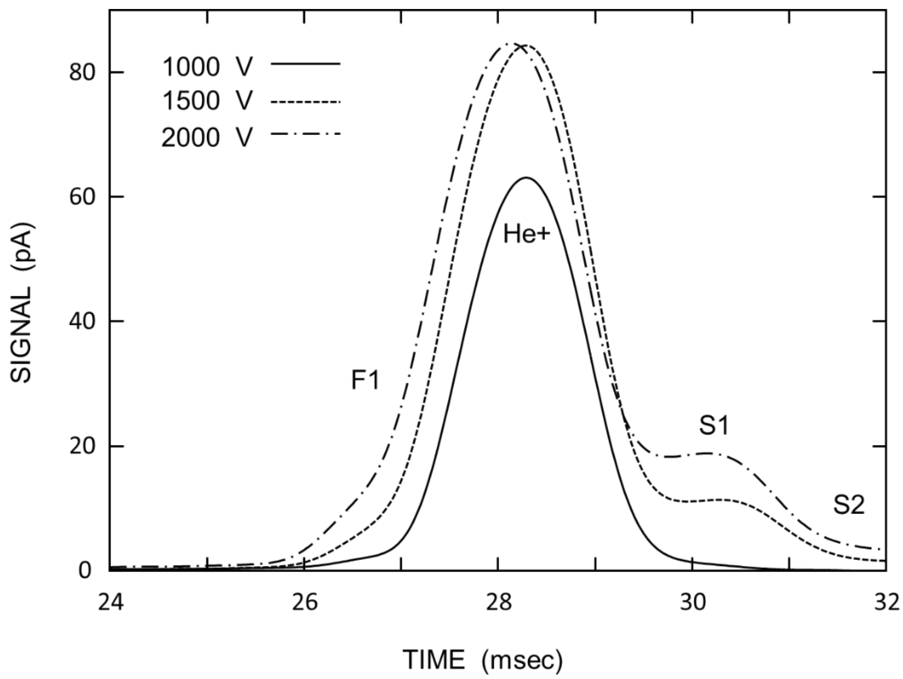

Figure 3.11: Current signal detected at the collector as a function of time. The temperature was 1.084 K, and the drift field was 65 V/cm. The curves are labelled by the voltage on the power supply for the source.

In Figure 3.11 we show data taken at 1.084 K with the power supply voltage for the alpha source set to 1000, 1500 and 2000 volts. The actual voltage V_S on the source was about 552 volts and varied by less than 2 volts as the power supply voltage was changed. The voltage V_0 on G0, the voltage V_1 on G1, and the voltage V_2 on G2 were held constant at 420, 390, and 400 volts, respectively. In the figure one can see a strong signal from an ion which we label He+, and a slower ion S1. The arrival time of the He+ ion varies by 0.5 % between the three traces. Note that around 1 K the ion mobility varies rapidly with temperature, and a temperature variation of only 0.5 mK is large enough to cause this variation. In addition, there is a weak indication of two other ions F1 and S2. The F1 ion will be seen more clearly in the data shown later. One can only obtain the evidence for the existence of S2 by making a fit to the S1 signal and then subtracting it from the data.

When the power supply voltage for the source was reduced to be 800 V, no visible glow was emitted from the cell, and the actual voltage on the source was 500 V[8]. The data taken under this condition is shown as the solid line in Figure 3.12. The F1 ion was more clearly seen as the magnitude of the signal from the He+ significantly decreased. Note that alpha particles still ionize helium atoms in the vapor, and thus the vapor is still somehow conductive.

The data we discussed above were taken with $V_S > V_0 > V_1$. This seems apparently to be the necessary condition to drive a positive charge flow through the experimental cell. Thus, we call this the "normal configuration." However, it was found with $V_S < V_0 > V_1$ that a stable plasma was still maintained, and a large signal could be detected at the collector. We refer to this as the "reverse configuration." A signal taken with the reverse configuration is shown as the dashed line in Figure 3.12. The power supply for the source was turned off. The voltages on S and G1 were 235 V and 420 V, respectively. It is striking that the F1 signal is even larger than the He^+ signal. We could also detect a signal at the collector with $V_S = V_0 > V_1$, which is shown as the dash-dotted line in Figure 3.12. The voltages on S and G1 were 420 V and 420 V, respectively.

[8] See the circuit diagram in section 3.2.2 for the origin of this voltage division.

In Figure 3.13 we show the ratio of the mobility of the F1 and S1 ions to that of the He^+ ion in the temperature range from 1.022 to 1.238 K. The drift field was kept constant at 65 V/cm. Over this temperature range, the mobility of the He^+ ion varies by a factor of ~4.5. In the figure it seems the F1/He^+ ratio slightly decreases as the temperature increases. The S1/He^+ ratio shows a significant oscillation so that we cannot determine whether there is a trend over temperature. This oscillation probably comes from the uncertainty in the S1 mobility. As one can see in Figure 3.11, the S1 signal is always small compared to the He^+ signal.

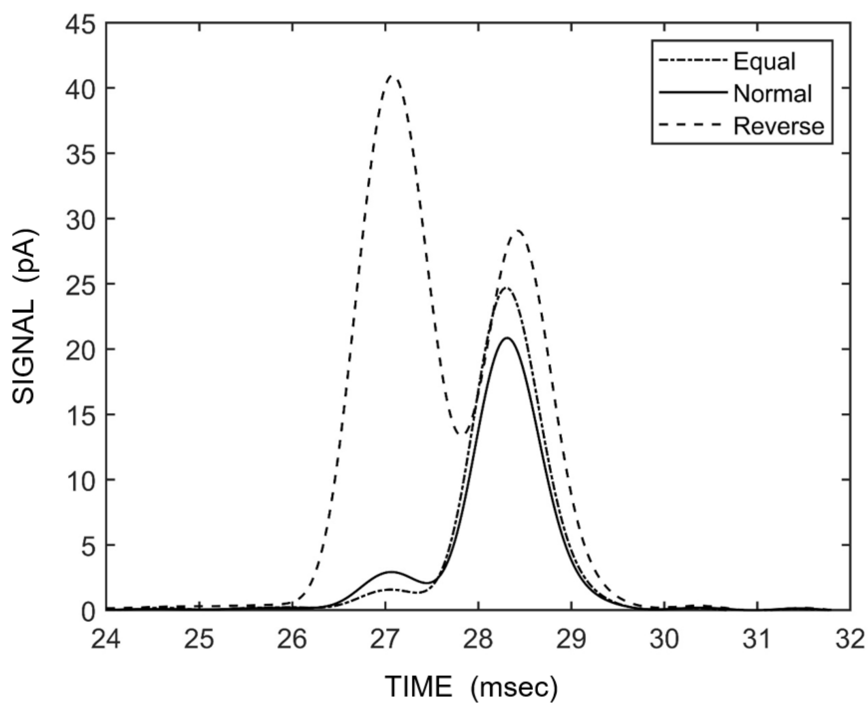

Figure 3.12: Current signal detected at the collector as a function of time. The temperature was 1.084 K, and the drift field was 65 V/cm. The solid line was taken with the power supply voltage for the source held at 800 volts. The dashed line was taken with the power supply voltage for the source held at zero. The dash-dotted curve was taken with an “equal” configuration, i.e., the voltage on the source was equal to that on G0.

3.4.3 Discussion

People have reported observations of multiple positive ions in liquid helium-3 [55][56][57][58]. However, the experiments suggest that the explanation for the origin of these ions is that some helium-4 impurities will attach to the snowballs composed of helium-3 atoms at very low temperatures. In the present experiment, the liquid does contain a small number of helium-3 impurities, but it seems unlikely that these will become attached to a snowball composed of helium-4.

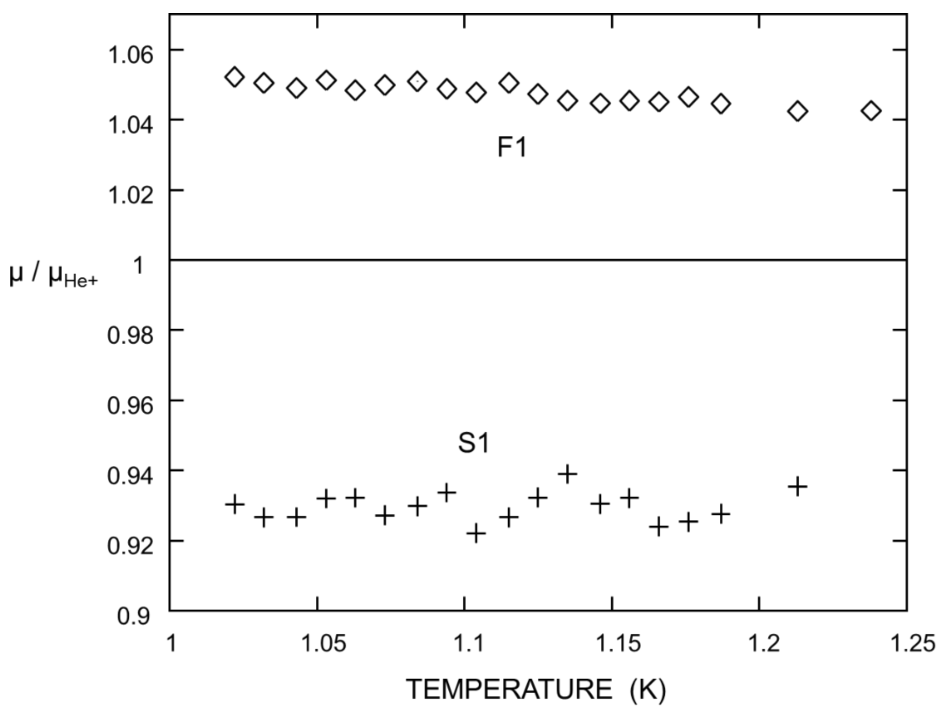

Figure 3.13: Ratio of the mobility of F1 and S1 to the mobility of He^{+} as a function of temperature.

The mobilities of those positive impurity ions measured by Johnson and Glaberson are shown in Figure 3.14. The variation of the relative mobility from one species to another seems to be larger than what was observed in the present experiment. Also, in the results of Johnson and Glaberson, the variation of the relative mobility with temperature appears larger.

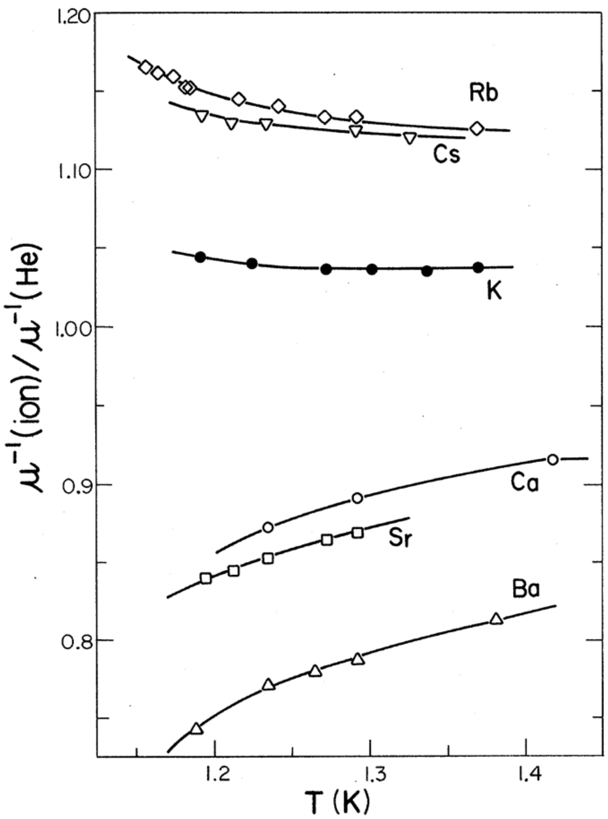

Figure 3.14: Relative ion mobility as a function of temperature, taken from Johnson and Glaberson [53].

In the experiments reported here, we speculate that when a positive helium ion enters the liquid and forms a snowball, it can form a number of different structures. For a particular structure to be stable, there needs to be an energy barrier that is sufficiently large to prevent a rearrange of the atoms. The energy barrier also needs to be large compared to the thermal energy scale $k_B T$. A barrier like this is more likely found between the states in which the core of the snowball has a different structure. The core of the helium snowball was studied by Mateo and Eloranta [59]. By performing a density functional theory calculation, they found that a linear triatomic He_3^+ core is energetically favorable. It would be interesting to extend their calculation to search for metastable states that are at a higher energy.

Measurements of the effective mass of a positive helium ion by Poitrenaud and Williams [60] give a snowball radius of 6 Å. This indicates there would be 26 atoms in the snowball if the helium number density in the snowball is the same as in solid helium at the freezing pressure. Given that the drag force on a moving ion in liquid helium is proportional to the square of the ion radius, the atom number in snowball needs to change by ~2 in order to have a mobility change of ~5%.

In summary, we have detected three, and possibly four, positive helium ions in liquid helium-4. The experimental conditions affect the magnitude of the detected signals in a complicated way, which is not fully understood at this point.

3.5 Observation of Exotic Ions with Alpha Source

Using the cell geometry as described in section 3.2, we were able to observe the exotic ion signals with the alpha source. The liquid level was positioned between grids G0 and G1. With suitable negative voltages applied to the source, G0 and G1, a stable plasma discharge was maintained in the vapor. There was no sign of the exotic ions with the normal configuration ($V_s < V_0 < V_1$). We could only see the exotic ions with the reverse configuration ($V_s > V_0 < V_1$). As an example, we show a data trace taken with alpha source in Figure 3.15 as the red curve. It clearly shows signals from multiple exotic ions. The data was taken at

1.030 K. The voltages applied to the source, G0, G1 and G2 were -323 V, -470 V, -380 V and -400 V, respectively. The drift field was 65 V/cm. And the liquid level was 1.5 mm above G1. The negative gate pulse applied to G0 and G1 was of amplitude 40 V and width 0.6 msec.

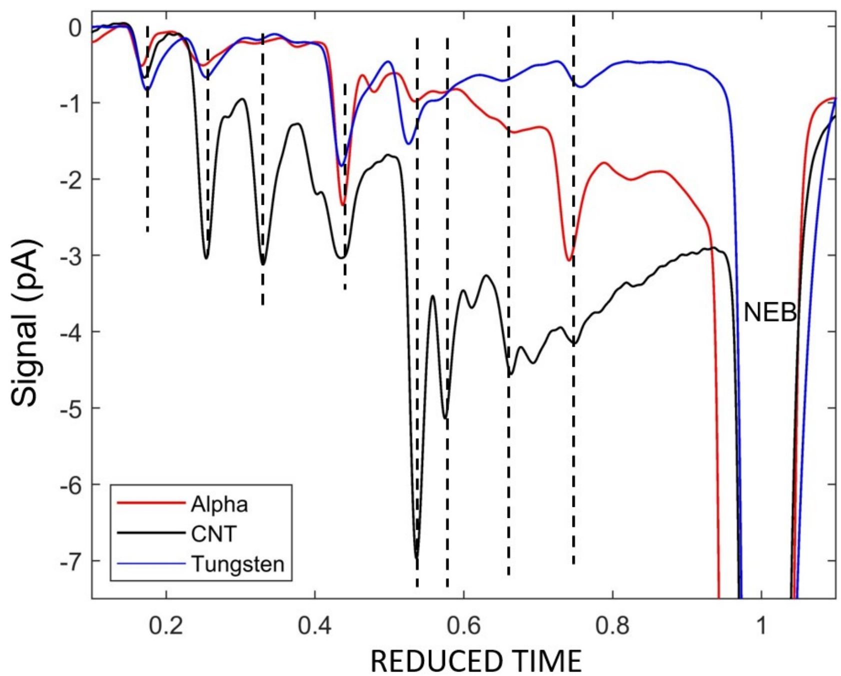

Figure 3.15: Current signals detected at the collector as a function of time. The arrival time of the NEB is normalized to be unity. The red curve shows the data taken at 1.030K with the alpha source. The black curve shows the data taken at 1.040 K with the carbon nanotube tips (CNT). And the blue curve shows the data taken at 0.991 K with the tungsten tips.

As a comparison, we also plot two data traces that were taken with the tungsten tips and the carbon nanotube tips. These two data races were from Wei and Xie's experiments [25][26][27]. The magnitudes of the exotic ion signals have been found to depend on a considerable number of experimental parameters [25]. Thus, it is not straightforward to make a comparison between the signal magnitudes obtained with the three sources. Generally speaking, the carbon nanotube tips could produce the strongest signals of the exotic ions. For the data taken with the alpha source, we have examined all the peaks above the noise level and found that all of them also appeared with either the tungsten tips or the carbon nanotube tips, or both. At least eight exotic ions can be seen with all the three sources, as indicated by the vertical dashed lines in Figure 3.15. This implies that the origin of the exotic ions is not relevant to the material of the source.

In Wei and Xie's experiments with sharp tips, they observed a signal degradation over time. The reason was assumed to be that the tips became blunt during the course of discharge. However, a time dependence of the signal and the plasma was also observed in our experiments with the alpha source. We found that the signals from the exotic ions quickly decayed, and almost completely disappeared after running for a day or two, although a large signal from the NEB was observed throughout the whole run. The time dependence associated with the alpha source has not been understood yet.

3.6 Discussion of Possible Explanations for Exotic Ions

As discussed in Chapter 1, there are at least eighteen different exotic ions observed in liquid helium. The intermediate ions can be only seen with a plasma discharge. The fast ion can be seen with either a plasma discharge or a source (radioactive source or sharp tips) immersed in liquid. Although the exotic ions have been studied for years, there is so far no accepted theory for the origin. In this section we present a brief overview of some possible explanations. Firstly, we summarize some points that Ihas made in his thesis [20] as follows:

a) A bubble that contains two electrons is unstable; therefore, it should be rejected as the explanation.

b) A bubble that contains an electron in an excited quantum state should be larger than an NEB. Thus, it should have a mobility that is lower than the NEB mobility. However, all the exotic ions have a mobility higher than that of the NEB. In addition, the lifetime of an excited state [38] is too short compared to the time for the exotic ions to travel through the time-of-flight cell.

c) The possibility that one of the exotic ions could be a helium anion He^- was considered by Ihas. The atomic structure is $1s2s2p\ ^4P_{1/2,3/2,5/2}$. The lifetime in vacuum is 11 μs for J=1/2 and 3/2, and 345 μs for J=5/2. The lifetime is not supposed to be longer in liquid helium. Ihas suggested that the lifetime of these anions is too short compared to the measured transit time of the exotic ions. Another candidate would be the helium negative dimer ion He_2^-, yet this also has a short life in vacuum, which is not supposed to be longer in liquid helium [25].

We also note that for several exotic ions, Eden and McClintock [21][22][23] measured the critical velocity for vortex nucleation. They found that the critical velocity of the exotic ions is higher than that of the normal electron bubble. And Williams *et al.* [61] pointed out that this would suggest the radius of the exotic ions is smaller than that of the NEB according to most theories for the ion-vortex-ring transition [62]. Any bubbles containing more than one electron should have a radius larger than that of the NEB and thus cannot be the nature of the exotic ions.

Then we discuss four other possible explanations proposed for the exotic ions.

3.6.1 Core-Shell Model

In order to explain the structure of the exotic ions, including the fast ion, Lawandy [63] proposed a core-shell model. His model is sketched in Figure 3.16. The core is supposed to be a positively charged He_n^+ solid cluster with an effective radius of a. In the shell region between the surface of the cluster and the surface of the bubble (of radius R), two electrons are trapped.

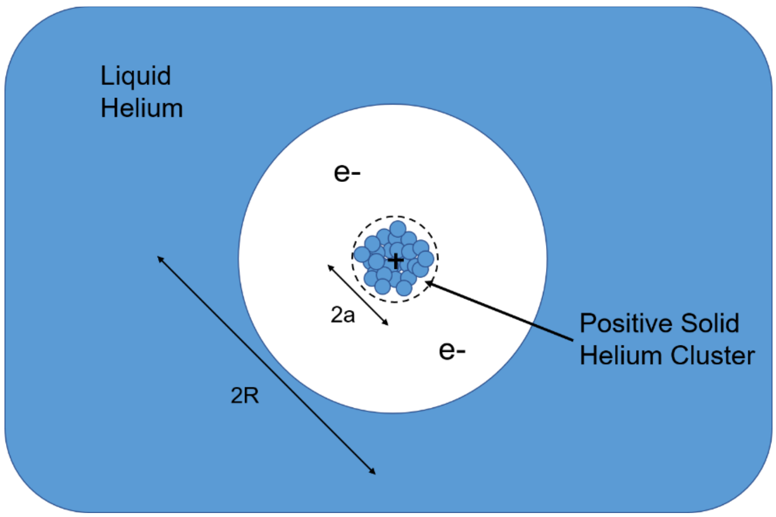

Figure 3.16: Schematic of the core-shell model proposed by Lawandy [63].

The electron wave function was taken to be zero at the cluster surface at $r = a$ and the bubble surface at $r = R$. The single electron unperturbed wavefunction was used to calculate the ground state energy. The total energy of the core-shell bubble was then given as

$$E = 2E_c + E_e + 2E_g + 4\pi R^2\sigma + \frac{4}{3}\pi R^3 P \tag{3.8}$$

where E_c is the energy correction for the electron-core interaction, E_e is the energy correction for the electron-electron interaction, and E_g is s-state energy of a single electron in the shell. From this equation, one can find the bubble radius at which the total energy is a minimum. Lawandy found that a range of values of the effective radius a from 0.88 Å to 6.0 Å gave bubble radii that could fit the exotic ion mobilities observed in the experiments. For the exotic ions, Lawandy also used this core-shell model to calculate the critical pressure at which the bubble explodes. For example, his calculated critical pressure for the fast ion was ~ -7 bars.

Clearly, the core must be positively charged in order to have a bubble that is smaller than the normal electron bubble. One possible issue seems to be that the core was calculated to be very small for those exotic ions with higher mobilities. For example, for the fast ion, a core radius of only 0.88 Å was given, which is even smaller than 1 Å. That a very small core radius was needed then brings up the question about stability, i.e., whether the electrons will penetrate the thin solid layer and combine with the positive charge at the core. Also, it is not obvious whether this core-shell structure is stable against non-spherical perturbations.

3.6.2 Electrons Trapped on Vortex Rings

Another type of structure was proposed by Elser [64] and further discussed by Khrapak and Bronin [65]. In superfluid helium, electron bubbles can be trapped on quantized vortex rings and lines. This is because an electron bubble replaces a certain volume of rotating superfluid around the vortex and reduces the system energy by an amount that is equal to the kinetic energy of the removed liquid [66]. Elser proposed that there could be states in which an electron is weakly bound to a vortex ring without being localized in a bubble. The helium density decreases as the distance r from the center of the vortex core decreases. This causes an attractive potential $V(r)$ to the electron, which binds the electron to the vortex ring. The electron in these states is highly delocalized and has an energy that is only slightly lower than 1 eV. Elser calculated the total energy E_{tot} of the electron-vortex-ring complex, including the electron binding energy E_{el} and the energy of the vortex ring E_{vor}, and determined how E_{tot} varied with the radius R of the ring. He showed that there was an equilibrium state at a ring radius of 6.7 Å. Elser considered this state as a candidate for the fast ion. He calculated the mobility of the ring to be 5.4 $cm^2\,V^{-1}\,s^{-1}$ at 1 K, which is far below the measured mobility 24 $cm^2\,V^{-1}\,s^{-1}$. However, Elser pointed out that his calculation underestimated the mobility.

Khrapak and Bronin [65] suggested Elser made an incorrect conclusion that the highly delocalized electron barely has any effect on the structure of the vortex core. They performed more detailed calculations for the total energy of the electron-vortex-ring complex. They found stable states with a range of the ring radius from 17 Å to 21 Å. Khrapak and Bronin mapped these stable states into exotics ions and found mobility ratios close to measured values[9]. For example, they calculated the ratio of the mobility of the fast ion to the mobility of No. 4 exotic ion[10] to be 4.4; the measured value is 5.4.

[9] Khrapak and Bronin followed Elser's calculation. They pointed out that this calculation could give a reliable estimation for the mobility ratio of two states, although it did not directly give accurate mobilities.
[10] The numbering by Wei *et al*., as shown in Figure 1.6.

It would be interesting to perform a more accurate calculation by density functional methods to examine the electron-vortex-ring structure, as pointed out by Elser. The calculations made so far took a greatly simplified form of the liquid density; the density was assumed to vanish within the vortex core ($r \leq 0$) and equal to the bulk density anywhere else. A natural guess is that the ground state of the electron-vortex-ring complex provides the explanation for the fast ion. Then one can continue to find other excited states and investigate if these states can give the structure of the intermediate ions. An accurate calculation for the mobilities of these states is also needed. The lifetime of these states must be longer than the typical transit time observed in the mobility experiments, which is about tens of milliseconds. It would be also important to study the effect of high electric fields on the proposed electron-vortex-ring complex. The previous experiments [21][22][23] show that the exotic ions were stable up to an electric field of at least 3×10^3 V/cm. And an explanation for the abrupt velocity reduction (as shown in Figure 1.5) at a critical field would be needed.

3.6.3 Fission Theory

The third theory to present here is the "fission theory", which was first introduced by Maris [67] and then further discussed by Wei *et al.* [25][68]. There is so far no complete theory for the bubble formation process in liquid helium. A general picture would be as follows [69]. When an energetic electron enters the liquid, it first loses kinetic energy by exciting and ionizing helium atoms. After the electron energy falls below the first excitation energy of helium (19.8 eV), the electron can only lose energy by elastic scattering from helium atoms. This will be very inefficient due to the large difference in mass between the electron and helium atom. The energy loss of the electron after a single collision with a helium atom is $\Delta E / E = 2m_e / M_{He}$, where m_e and M_{He} are the masses of the electron and helium atom, respectively. Supposedly, an electron only starts to form a bubble after its energy drops below 1 eV. This picture qualitatively agrees with the experiment [70] that measured the distance an electron travels from an initial position until a bubble is formed.

Further details about this picture are still not clear. What will be the electron wave function when the electron stops to form a bubble? If the wave function is distributed over some distance before the bubble is formed, does the whole wave function simply end up within a single bubble? Can the wave function be divided into two or more bubbles? If the interaction between the helium and electron constitutes a measurement to determine the position of the electron, one can argue that all the wavefunction must end up within one bubble. However, what constitutes a measurement is still an open question.[11] If we assume the wave function ψ can be divided into two bubbles, it was shown [25] that the integral f of $|\psi|^2$ over the volume of each bubble is likely to take a particular value from a discrete set $\{f_n\}$. Then it is possible that the bubbles will have discrete radius and mobility. Therefore, this could provide a possible explanation for the exotic ions.

3.6.4 Impurities

The last possible explanation we discuss here is that the exotic ions simply come from the impurities in the cell that are ionized in the plasma. The plasma formed in helium vapor

[11] We will discuss this in more detail in the next chapter.

may not be energetic enough to knock impurities off the cell wall. However, the excited helium atoms may deposit energy to the cell wall and knock off some impurities. High energy photons may do the same. The impurities on the wall include not only the material of the wall but also the air components (such as nitrogen, oxygen, and water vapor) frozen on the wall.

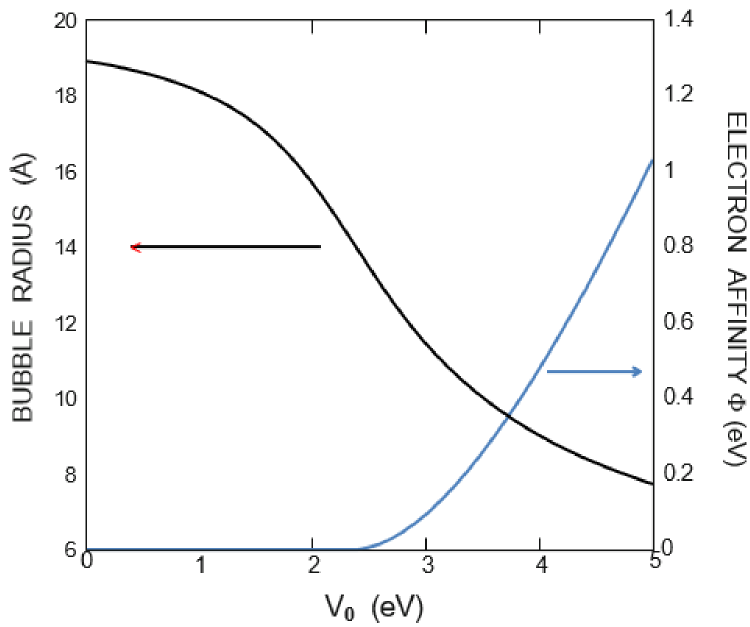

Figure 3.17: Bubble radius and electron affinity as a function of the potential depth V_0, adapted from Wei *et al.* [25].

The radii of the bubbles formed by the H^-, O^- and O_2^- ions have been calculated by Khrapak and Schmidt [71][72]. They took a simple pseudopotential as the interaction between the excess electron and the atom of the ion. The pseudopotential was constructed by a hard-core repulsion and a long-range polarization attraction. The radii they obtained for the H^-, O^- and O_2^- ions are 4.5 Å, 3.6 Å and 5.8 Å, respectively. Khrapak and Schmidt then considered the structure of O_2^- to be a small bubble and the structure of O^- to be a bubble surrounded by a solid layer of helium atoms. They proposed that H^- should be in a bubble surrounded by a layer of condensed but not solid helium. Wei *et al*. [25] used a similar but simpler model to calculate the radii of impurity ions in liquid helium. The impurity ion was treated as providing an attractive step potential $-V_0$ to the excess electron. They then found the radius of the ion for different electron affinities Φ. The results of Wei *et al*. are shown in Figure 3.17.

It would be interesting to use more accurate models to calculate the structure of those potential candidate ions, such as H^-, O^- and O_2^-. However, it seems unlikely that the impurities can explain all the 18 different exotic ions. Also, all the wavelengths of emitted light from the plasma in the experiment were found to come from the spectrum of helium [25].

Chapter 4

Experimental Investigations of Continuous Backgrounds A and B in Mobility Measurements

There have been 18 different exotic ions observed in liquid helium, each of which has a characteristic mobility higher than that of the normal electron bubble. The data obtained from the previous experiments revealed not only the components from the exotic ions but also two other components that vary continuously with time. These components are referred to as "background A" and "background B." In this chapter further experimental investigations of backgrounds A and B are presented. We will discuss under what conditions these backgrounds appear and possible explanations for their structures. Part of the content in this chapter was published as "Experimental Investigation of the Quantum Measurement Process Using Electrons in Superfluid Helium" in the Journal of Low Temperature Physics [73].

4.1 Previous Works

As discussed in Chapter 1 and Chapter 3, mobility measurements in liquid helium have been performed by different labs [16][18][19][20][21][22][23] [24][25]. The data obtained

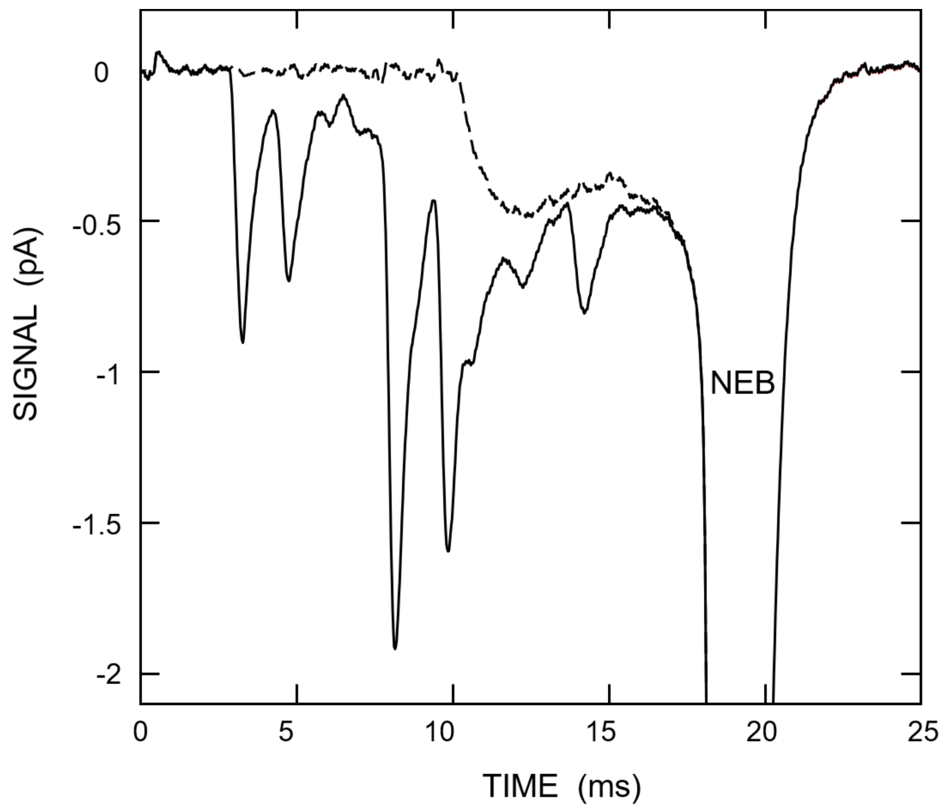

Figure 4.1: Solid curve shows current arriving at the collector as a function of time. The data was taken by Wei *et al*. [25]. The temperature was 0.991 K, and the drift field was 82.1 V/cm. The dash curve shows the result after subtracting each of the peaks from the data. The large peak labelled as "NEB" comes from the normal electron bubbles.

from these experiments have revealed several different components in the detected signal. The existence of different components has been discussed in refs. [25] and [74]. In Figure 4.1, we replot a data trace from the experiment of Wei *et al.* [25]. This experiment used sharp tungsten tips in the helium vapor to produce a plasma. The temperature was 0.991 K, and the drift field was 82.1 V/cm. The solid curve shows the current detected at the collector as a function of time. This curve shows a set of peaks, including the fast ion, intermediate ions, and normal electron bubbles. These have been discussed in previous chapters. One can make a fit to each peak coming from the exotic ions and then subtract the peak from the data. This process cannot be mathematically rigorous because there is no accepted theory for the shape of the peak. However, it is good enough to reveal that there is another component of the signal; this is the continuous background shown by the dashed line in Figure 4.1. The background signal has some remarkable features and has been discussed in refs. [25] and [74]. Key results include:

i. Under some conditions, the continuous background is present without any peaks from the exotic ions.

ii. The time dependence of the background signal varies with the experimental conditions. Figure 4.2 shows data taken from ref. [25]. When the current that is injected to maintain the plasma, i.e., the current from the sharp tips at the top of the cell or from a radioactive source, is small, the background is as shown by the solid curves in the Figure 4.2. We call this background type A. However, if the current is increased by changing the voltages applied across the plasma, for example, then at some point there is an abrupt change in the background and it becomes as shown by the dashed line in Figure 4.2. We call this extra background signal background B; the total background when this happens is the sum of backgrounds A and B.

iii. The amplitude of background A decreases monotonically with decreasing arrival time t of the signal as seen in Figure 4.2. It is possible that it becomes zero below a critical value of t but this is not established.

iv. Background B becomes zero before a critical arrival time τ_B, which is roughly half of the arrival time of the normal electron bubbles. At a time t that is slightly larger than τ_B, the background B signal is proportional to $\sqrt{t-\tau_B}$. The time τ_B varies with the temperature and with the applied drift field in just the same way as does the transit time of the exotic ion that has an arrival time close to τ_B. This indicates that the continuous background B is composed of ions.

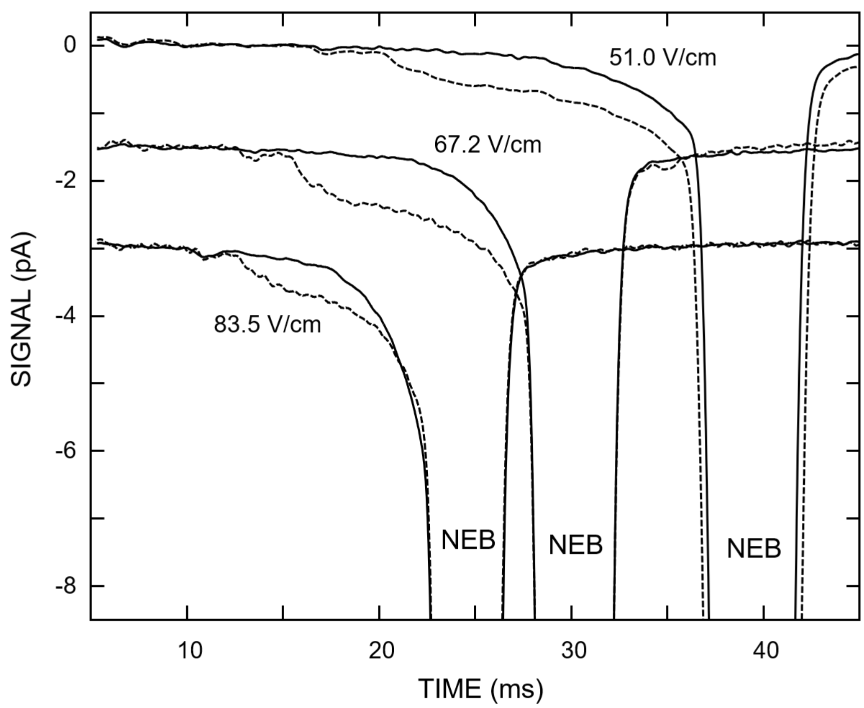

Figure 4.2: Current arriving at the collector as a function of time, adapted from Wei *et al.* [25]. The temperature was 1.025 K, and the curves are labelled by the drift field. The signal arising from the normal electron bubbles is labelled as "NEB." The dashed curves show the data taken when background A+B is present, and the solid curves are taken when the voltages for the plasma have been changed so that background B disappears.

It appears from the experiments performed so far that background A can be seen only if (a) there is a signal from the NEB, and (b) the background B and exotic ions do not mask background A.

4.2 Study of Background A

In this section we report on experiments to study background A. Electrons are produced by a plasma discharge in the vapor above the liquid surface. For electrons with energy only slightly higher than the 1 eV energy barrier, the wave function will experience a "reflection above the barrier." Only a part of the wave function is transmitted into the liquid. We investigate the possibility that this partial transmission leads to the formation of electron bubbles that contain only a fraction of the complete electron wave function. Our simulation of the mobility of these bubbles is in reasonable agreement with the measured signal in background A and supports the idea that the interaction between the electron and liquid helium does not constitute a quantum measurement. In quantum mechanics, what constitutes a measurement is still an open question. Our experiments help provide new information on this subject.

4.2.1 Introduction

In quantum mechanics, the state of a quantum system is described by the wave function Ψ. It is well known that the wave function changes in two different ways. One is described by $\frac{\partial \Psi}{\partial t}$ as governed by the Schrödinger equation. The other way to change Ψ is by quantum measurements. According to the well-known Copenhagen interpretation, if a physical quantity f gets measured, the result of the measurement must be one of the eigenvalues $\{f_n\}$ of the operator $\hat{f}$. If the result of the measurement turns out to be the eigenvalue f_n, the wave function will immediately change to the corresponding eigenfunction ϕ_n. This process is the so-called "collapse of the wave function."

However, there are several undetermined questions regarding the quantum measurement. The first question is: What constitutes a measurement? It was argued by Putnam that quantum mechanics "treats the universe as consisting of two kinds of objects – classical objects not subject to uncertainties and micro-objects – with the former measuring the latter" [75]. However, as indicated by Putnam, this argument is not in agreement with the principal that quantum mechanics applies to all objects in the universe. Similar questions have been discussed for many years, for example, in the papers by Putnam [76], by Bell [77], by Margenau and Wigner [78][79], and by Cooper and Van Vechten [81][82][83]. In his paper Bell gave a brilliant description of the ambiguity in the concept of quantum measurement, which we would like to repeat here:

"What exactly qualifies some physical systems to play the role of 'measurer'? Was the wavefunction of the world waiting to jump for thousands of millions of years until a single-celled living creature appeared? Or did it have to wait a little longer, for some better qualified system . . . with a PhD?"

Another obvious question is regarding the sudden change that appears in the wave function instantaneously after the measurement is made [84]. Suppose, for example, that at time t a measuring device is used to detect a particle at a location $\vec{r}$. If the particle is found at $\vec{r}$, then the wave function is supposed to instantaneously collapse to a delta function at $\vec{r}$, i.e., vanish anywhere else. This must happen since otherwise a measurement performed shortly later at another position $\vec{r}\,'$ that is at a large distance from $\vec{r}$ would have a chance of finding the particle. As previously mentioned, this change cannot be described by the Schrödinger equation.

As an alternative to the Copenhagen interpretation, there have been many other proposals regarding the measurement process. These include, for example, the pilot wave interpretation of de Broglie [85] and Bohm [86][87], the many worlds theory of Everett [88], the continuous spontaneous localization model of Ghirardi *et al.* [89], and the decoherence theory of Zeh [90] and Zurek [91][92]. But at the present time none of these proposals has been generally accepted [93].

In this section we report on experimental results that are relevant to one particular aspect of the measurement problem. Our results are related to the thought experiment first proposed by Einstein in 1927[12] and discussed later by many others [95]. Here, we follow a description of this general type of thought experiment as given by de Broglie [96][97]. A particle is placed in a box B , which has impenetrable walls. A partition is then used to divide the box into two boxes B_1 and B_2 , each containing a part of the wave function. These two boxes are separated and moved far apart; de Broglie takes B_1 as moved to Paris and B_2 moved to Tokyo. The wave function in B_1 is $c_1\Psi_1$ and $c_2\Psi_2$ in B_2 , where Ψ_1 and Ψ_2 are functions that are normalized within boxes B_1 and B_2 , respectively. According to

[12] This was mentioned in ref. [94]. A. Fine [95] gave the name "Einstein's Box" to this type of thought experiment.

the Copenhagen interpretation, if box B_1 is opened first, the probability of finding the particle in B_1 is $|c_1|^2$. But if B_2 is opened first and the particle is not found in B_2, then there is a 100% probability of finding the particle in B_1. In this case a measurement in which no particle is detected has influenced the wave function of the particle and changed the probability of finding the particle at a location far away. de Broglie considered that this is impossible. A schematic of this experiment is shown in Figure 4.3.

There are further questions to consider for this type of experiment. In the above discussion de Broglie considered measurements made by some device which looks for a particle that is found after one of the boxes is opened. But it might also be possible that the walls of the boxes B_1 and B_2 make a measurement at some time after the box B has been divided, but before the boxes B_1 or B_2 are opened to look for the particle. The experiment described here looks to find out if the walls of a box do make a measurement with the result that all of the wave function is trapped in one of the boxes B_1 or B_2. If this is indeed what happens, it is interesting to ask at what time after the division of the boxes does this occur. A schematic view of the experiment is shown in Figure 4.4. We first trap only a part of the wave function of an electron in a "box." The "box" is a hollow cylindrical container of radius R, with its bottom sealed by a rigid plate. There is a piston of mass M at the top of the cylinder, which can slide without friction. At equilibrium the piston sits at the height L, which is determined by the balance between two forces exerted on the piston: (1) the downward gravitational force Mg, and (2) the upward force caused by the zero-point motion of the trapped electron. Suppose that the electron is in its ground state Ψ_g, and the integral of $|\Psi_g|^2$ over the volume of the cylinder is F [13]. The equilibrium position is then given as[14]

$$L = \left(\frac{F\hbar^2\pi^2}{m_e M g} \right)^{1/3} \tag{4.1}$$

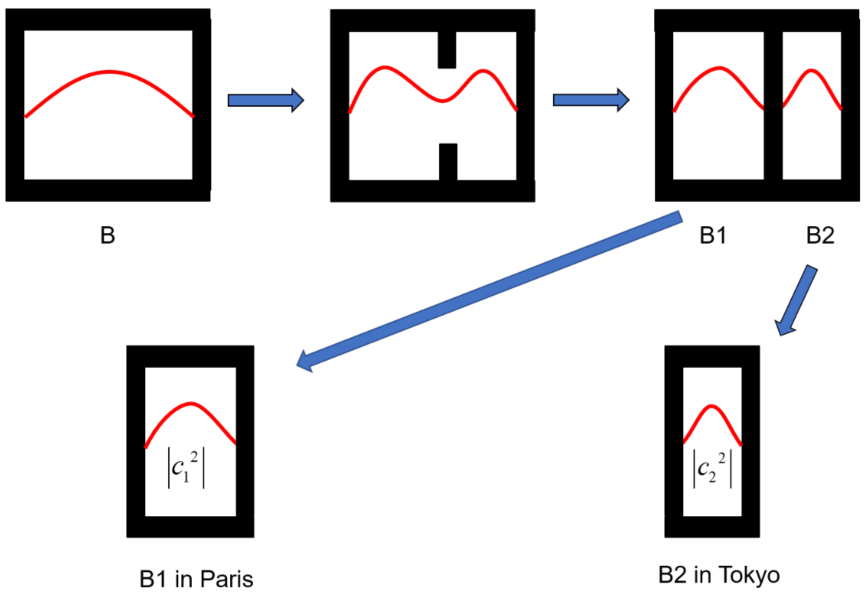

Figure 4.3: Schematic of the experiment described by de Broglie. The red curve denotes the wave function of the particle.

where m_e is the electron mass. In a "box" of this type, there will be a continuous interaction between the trapped part of the electron wave function and the walls of the box. An interesting question to ask is if this interaction results in a measurement that determines whether the electron is in the box or not. If this interaction does not result in a measurement, the

[13] Only a fraction F of the wave function is trapped in the cylinder.
[14] This assumes that the energy of the part of the wave function outside the cylinder is not influenced by the piston position.

equilibrium position of the piston will just be as given by Equation (4.1). But if a measurement results and determines whether there is or not an electron in the box, then the final position of the sliding piston will be either at $L = 0$ ($F = 0$) or $L = \left(\hbar^2 \pi^2 / m_e M g\right)^{1/3}$ ($F = 1$).

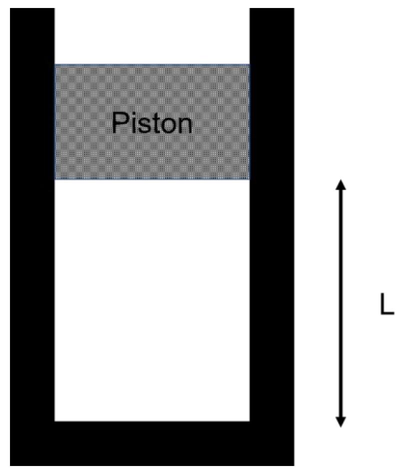

Figure 4.4: Concept of the experiment proposed in the text. The walls of the cylinder and the piston are assumed to be impenetrable.

In order to construct a "box" that traps a part of a wave function, one may consider to move a particle into some region and then manipulate the potential experienced by the particle within a short enough time to make only a part of the particle wave function trapped. This type of process has been discussed in refs. [98], [99] and [100]. Some semiconductor devices with voltage-controlled gates [101][102] might be capable of being used for this. In the present experiment the trapping process happens automatically in liquid helium, and we can simply perform time-of-flight mobility measurements to determine whether some part of the wave function is still trapped at a later time, as we will see below.

In the present experiment a plasma discharge is maintained in helium vapor above a volume of superfluid helium to provide a source of electrons. Note that electrons in the plasma have a continuous distribution of energy. For an electron from the plasma to enter the liquid, the electron must have an energy above the barrier height V_0 (~1 eV) at the liquid-vapor interface. The trapping process is illustrated schematically in Figure 4.5. An electron from the plasma comes close to the liquid-vapor interface. For an electron of energy above V_0, a part of the electron wave function will be transmitted into the liquid, and a part of the wave function will be reflected; this is the so-called "reflection above the barrier." As previously discussed in section 3.6.3, the transmitted part of the wave function will lose kinetic energy via scatterings with helium atoms and travel several hundred Å [69] before it moves slowly enough to get trapped in a bubble. The 1 eV energy barrier provided by the liquid make the parts of the wave function inside and outside the bubble well isolated, i.e., the tunneling rate through the helium barrier is much too slow to be important.

We assume that the integral of $|\psi|^2$ over the space containing the transmitted part of the wave function is F. This transmitted part of the wave function will form a bubble of radius $\tilde{R}$, and then it has the form as below

$$\psi = \sqrt{\frac{F}{2\pi\tilde{R}}}\frac{\sin\left(\pi r/\tilde{R}\right)}{r} \tag{4.2}$$

The total energy of the bubble at zero pressure is then given by

$$\tilde{E}_{bubble} = \int_{r\le\tilde{R}} \psi\left(-\frac{\hbar^2}{2m_e}\nabla^2\psi\right)d^3\vec{r} + 4\pi\tilde{R}^2\sigma = \frac{Fh^2}{8m_e\tilde{R}^2} + 4\pi\tilde{R}^2\sigma \tag{4.3}$$

Then at the energy minimum we obtain $\tilde{R} = F^{1/4} R_{NEB}$, where R_{NEB} is the radius of the NEB.

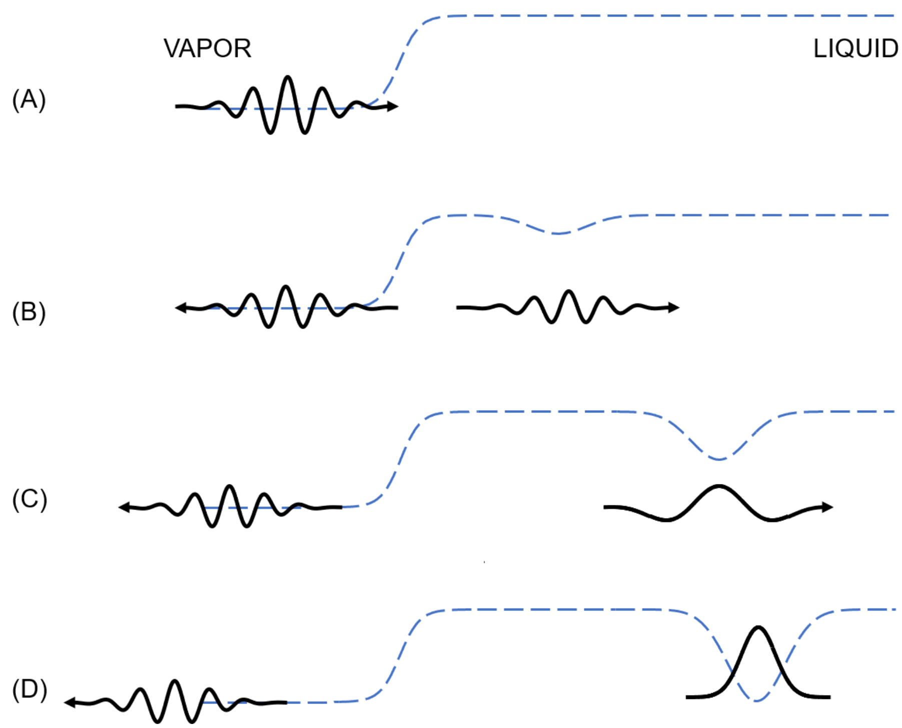

Figure 4.5: Schematic diagram of the trapping process occurring in liquid helium. The solid line denotes the wave function of the electron, and the dashed line is a sketch of the density profile of the liquid helium; the bulk liquid sits on the right-hand side of the figure. The potential acting on the electron is taken to be approximately proportional to the liquid density. In (A) an electron approaches the liquid-vapor interface with an energy above the 1 eV barrier. In (B) the wave function is partially reflected, and partially transmitted into the liquid. Then an incipient bubble is formed in the liquid (C) and grows to its equilibrium size (D).

Note that in the above discussion, we have assumed that during the trapping process the helium did not make a measurement even though the trapped part of the wave function was constantly interacting with the helium atoms surrounding it. If the helium did make a measurement, it would result in either a normal electron bubble ($F = 1$) or no bubble ($F = 0$).

As we will detail later in section 4.2.2.2, the electrons in the plasma have a continuous distribution of energy. Thus, the values of F should also have a continuous distribution, and electron bubbles with a continuous size/radius distribution should be produced in the liquid. To calculate the distribution of the bubble radius, we need to know the energy distribution of the electrons in the plasma and how the value of F is dependent on the electron energy. These will also be discussed later in section 4.2.2.2. Now the problem comes down to how to detect the existence of these bubbles. As previously discussed, in superfluid helium at temperatures around 1 K, to a good approximation the mobility is inversely proportional to the roton number density and the square of the bubble radius, i.e., $\mu \propto \exp(\Delta / k_B T) / R^2$. Therefore, we can perform mobility measurements to look for the existence of bubbles with a continuous size distribution produced by the mechanism we just discussed above. One just need to look for the existence of negative ions that have a continuous distribution of mobility.

For a discussion of the formation of a bubble by an electron entering liquid helium, see the papers of Hernandez [103], Rosenblitt and Jortner [104], and Eloranta and Apkarian [105]. Arguments for and against the possibility of forming bubbles containing only a fraction of the wave function of an electron have been presented by Maris [67], Wei *et al.* [68], Elser [106], Rae and Vinen [107], Jackiw, Rebbi and Schrieffer [108] , Altschul and Rebbi [109], and Mateo, Pi and Barranco [110]. In addition, we mention that there is a detailed review of the quantum measurement process in chapter 8 of the book by Greenstein and Zajonc [111].

4.2.2 Experiments

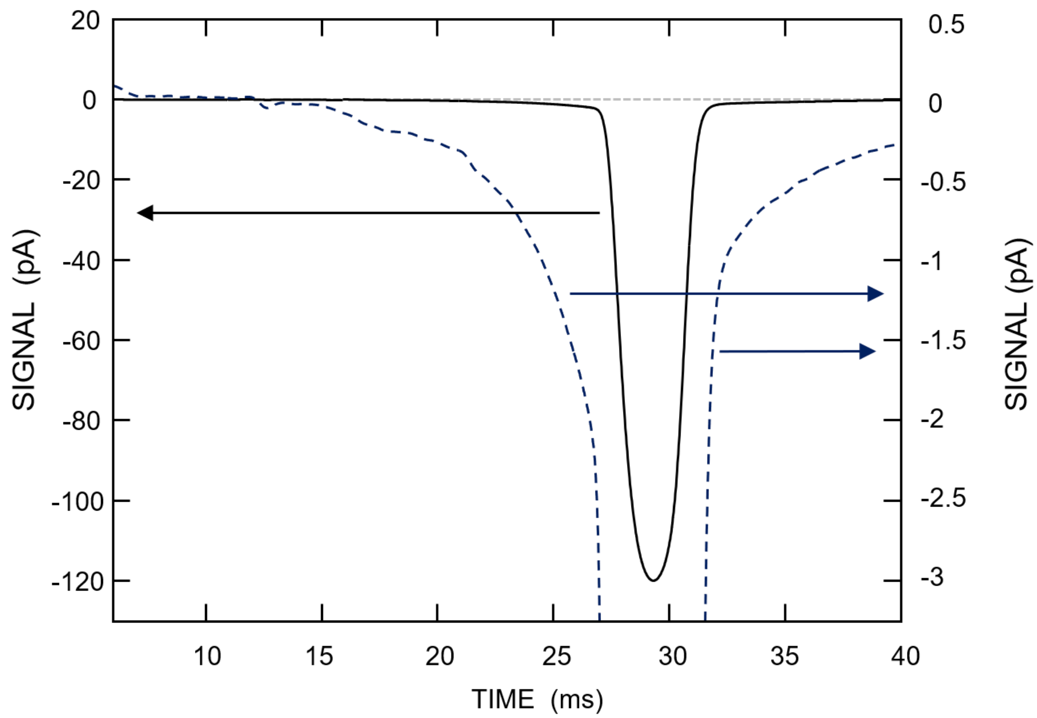

Figure 4.6: Current arriving at the collector as a function of time. The temperature is 1.014 K and the drift field is 65.0 V/cm. The voltage difference ΔV_{01} applied between grids G0 and G1 is 40 volts. The solid curve uses the scale on the left, and the dashed curve is an expanded plot using the scale on the right.

The cell configuration used in the experiments was as described in section 3.2. We have performed a detailed study of background A at many different temperatures, drift fields, and voltages applied to the source S, and the grids G0, G1 and G2. And we also optimized the signal to noise ratio. An example of data taken at 1.014 K is shown in Figure 4.6. The liquid level was positioned at approximately 0.5 mm above grid G1. The data shown in Figure 4.6 were taken with the reverse configuration: S=−283 V, G0=−430 V, G1=−390

V, and G2=-400 V, and the drift field was 65 V cm^{-1}. The amplitude of the gate pulse applied to G0 and G1 was constant at 40 V. The amplitude of the normal electron bubble peak in the signal is approximately 120 pA.

4.2.2.1 Leakage Current

As previously discussed in section 3.2, the Frisch grid plays a key role in the experiment. It significantly reduces the image charge induced on the collector before the ions pass the grid. It would be necessary to have quantitative information about how the Frisch gird reduces the image charge. In previous works [24][25] it was already proposed by Wei *et al.* that background A may come from electrons that are partially transmitted into the liquid. However, the functioning of the Frisch grid was still somehow uncertain at the time of these papers because of a lack of information about the grid geometry. As a slab of ions approaches this grid, there will always be some degree of penetration/leakage of field lines from the ions to the collector plate, as shown schematically in Figure 4.7. This penetration will induce a positive image charge on the collector, which leads to a positive current flowing from the ground to the collector through the 2.5 MΩ resistor. Thus, a small negative current can be detected in the measured collector signal. This current is present before the ions reach the Frisch grid and increases as the slab of ions approaches the gird. It appeared that this might give a signal with a time dependence similar to that found in the experimental results shown in Figure 4.6. The leakage of even just a small fraction of the field lines is important because the background A signal is much smaller than the normal electron bubble signal. For example, in the data shown in Figure 4.6, the peak of the signal for the normal electron bubble is approximately 50 times the maximum signal from background A. To investigate the possibility that the leakage through the Frisch grid can provide an explanation for background A, we need to calculate how many field lines from the ion slab can pass though the grid to the collector. Here we report on a detailed analysis of the Frisch grid.

We first consider the form of the signal to be expected when the Frisch grid completely shields the collector and the measured signal comes entirely from the normal electron bubbles reaching the collector. The width of the peak in the signal is affected by the following effects:

1) The width and amplitude of the negative voltage pulse applied to G1 in order to generate an ion pulse.
2) The inhomogeneity of the drift field; this can give a "tail" after the arrival of the detected current peak resulting from the ion pulse. Note that field decreases as the radial distance from the central cell axis increases. Thus, the inhomogeneity of the field can only cause a tail after the peak, not before the peak.
3) The space charge effect, i.e., the repulsion between the normal electron bubbles making up the pulse.
4) The process during which the ions pass through the Frisch grid and move into the region between the grid and the collector.

As seen in Figure 4.6, the combination of these effects results in a signal which has a full width at half maximum of ~ 2.8 msec. Of these effects, 1), 2), and 3) mainly influence the width of the ion pulse before it passes the Frisch grid, whereas 4) has to do with how the collector responds after the incoming ion pulse has passed through the Frisch grid. Effect

4) has the consequence that the width of the detected signal is significantly larger than the actual time width of the ion pulse as it approaches the Frisch grid.

Then we consider the signal that results when a single zero-thickness slab of ions moves down the cell towards the Frisch grid and the collector; see Figure 4.7. Let the total charge on the ion slab be $-Q$. When there is no leakage through the Frisch grid, there will be no image charge induced on the collector until time t_F at which the slab reaches the grid[15]. After this time the induced charge Q_C on the collector[16] is

$$\begin{aligned} Q_C &= 0 && t_F > t \\ &= Q\frac{z_{FC} - z}{z_{FC}} && t_F + z_{FC}/v_{FC} > t > t_F \\ &= 0 && t > t_F + z_{FC}/v_{FC} \end{aligned} \tag{4.4}$$

where z is the distance of the ion slab from the collector, z_{FC} is the distance from the Frisch grid to the collector, and v_{FC} is the velocity of the ions while moving between the grid and the collector. When the ions reach the collector, the charge Q_C drops to zero[17]. The collector current is then given by

$$\begin{aligned} I(t) &= 0 && t_F > t \\ &= -Q v_{FC}/z_{FC} && t_F + z_{FC}/v_{FC} > t > t_F \\ &= 0 && t > t_F + z_{FC}/v_{FC} \end{aligned} \tag{4.5}$$

---

[15] If the geometry is chosen appropriately, the grid can be made in such a way that only a small leakage of field lines comes from approaching ions. However, for this same geometry most of the field lines from G2 that make up the static drift field can pass through the grid. This has the consequence that most of the ions can pass through the grid rather than ending up on the grid wires. For a discussion about this interesting property of the Frisch grid, see O. Buneman, T.E. Cranshaw, and J.A. Harvey, Can. J. Res. A27, 191 (1949). We calculated for our grid that ~88 % of the static field lines pass through the grid. This calculation was performed in a single cell of the grid by using the finite element method with the periodic boundary condition. Thus, assuming that the ions follow the field lines, only ~ 12 % of the ions are lost at the Frisch grid.

[16] This equation neglects the calculated 12% charge loss on the Frisch grid.

[17] There is a short delay due to the effective capacitance between the collector and the ground.

For the signal shown in Figure 4.6, z_{FC} / v_{FC} is 0.51 msec with the consequence that the actual width of the ion pulse when it approaches the Frisch grid must be significantly less than 2.8 msec. Given that this width is considerably smaller than the time range over which background A is present (see Figure 4.6), to a first approximation we can treat the ion pulse as a charge slab of zero thickness in calculating the leakage through the Frisch grid.

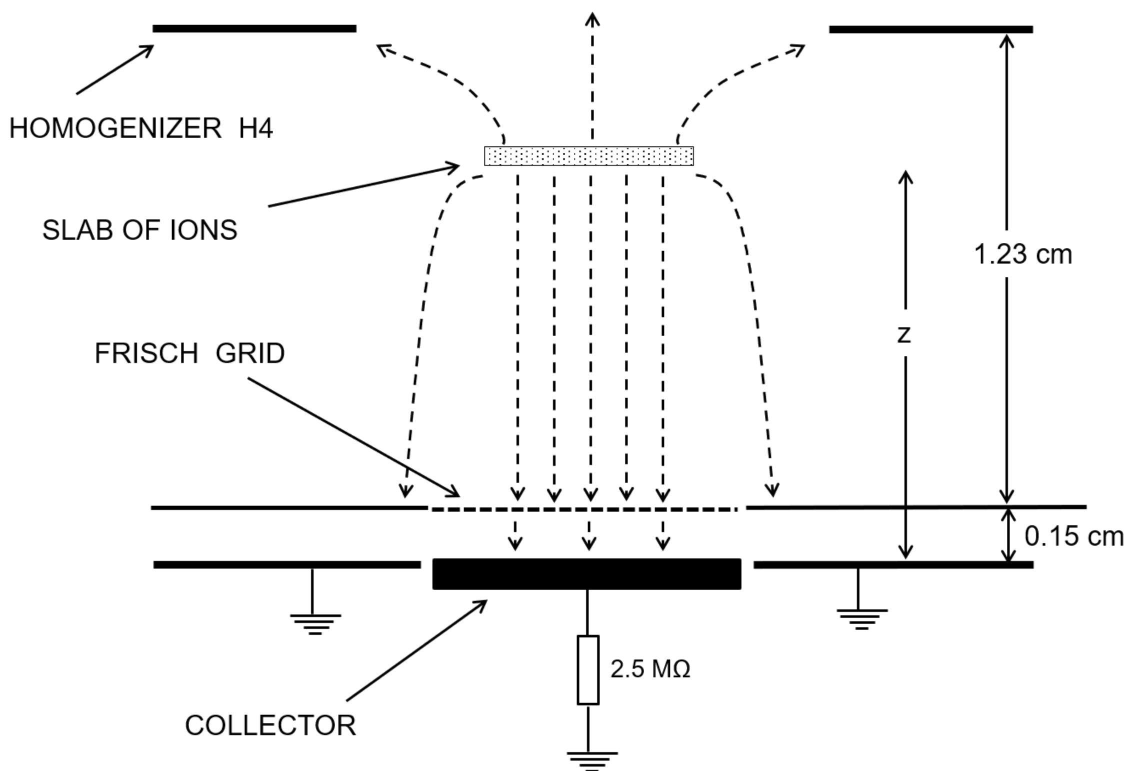

Figure 4.7: Schematic diagram showing a slab of ions approaching the Frisch grid and the collector. The dashed lines with arrows show field lines from the slab of ions to the lowest homogenizer disk H4, to the Frisch grid, and to the collector.

We discuss now the leakage/penetration of the field lines through the Frisch grid. Suppose that at distance z from the collector there is a zero-thickness ion slab centered along the central axis, and the charge on this slab is uniformly distributed within a radial distance of

0.4 cm. This supposes that the slab has the same diameter as grids G1 and G2 (see section 3.2.1). Our problem is then to find how many field lines starting from these ions can eventually pass through the Frisch grid and terminate on the collector. This is dependent on the distance from the collector and thus on the time. The detected current on the collector due to the leakage through the Frisch grid is given by

$$I(t) = -\frac{1}{4\pi}\frac{d}{dt}\int E\, dS = -\frac{dQ_{image}}{dt} \tag{4.6}$$

where the integral of the field E is over the surface area of the collector, and Q_{image} is the image charge induced on the collector.

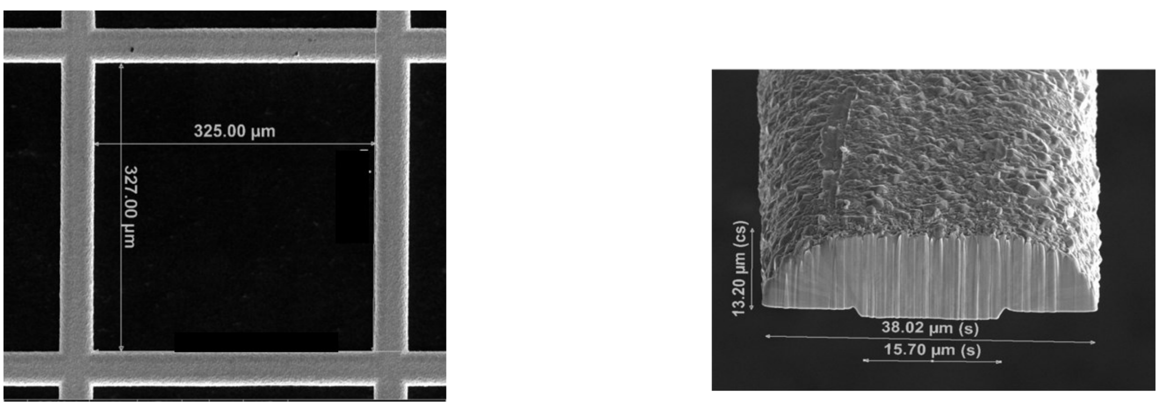

(a) (b)

Figure 4.8: Scanning electron microscope images of the Frisch grid. Part (a) shows one cell of the grid, and (b) was taken with higher magnification in order to show a cross-section of one of the wires.

To calculate the leakage of the field lines, detailed information about the geometry of the Frisch grid is needed. To this purpose, images of a section of the grid were made[18] using a scanning electron microscope. We show two examples of these images in Figure 4.8. In the calculation, we have slightly simplified the geometry of the grid. The spacing between wires was taken to be 326 μm in both the x and the y directions. The width and thickness of the wires were taken to be 38 μm and 13 μm, respectively. The rounded shape of the top corners of the wire was replaced by a quarter circle of radius 13 μm. We also neglected the small ridge at the bottom of the wire (as seen in Figure 4.8b) and treated the bottom as a completely flat surface. The dimensions of the collector and the other electrodes in the cell, such as the homogenizer disks H1-H4, were easy to measure.

We then detail the calculation for the number of field lines from an ion slab that can pass through the grid and reach the collector (see Figure 4.7). At first sight one would think of using the finite element method. However, this approach is very challenging because of the huge discrepancy between the dimensions of the electrodes such as H1-H4 and the wires making up the Frisch grid. A mesh needed in this case must be constructed in a very complicated way.

Instead, we used a Monte Carlo method [112][113] to perform the calculation. Monte Carlo methods have been widely used in electrostatic boundary problems. A straightforward approach is described as follows. Suppose that there is a charge Q located at a particular position in the drift region. A random walker is placed at the position of this charge and then start to undergo a random walk. The random walker stops once it arrives at a

[18] We thank Dr. Shaghayegh Rezazadeh for making these images.

conducting electrode. We then repeat this process for a large number $N_{walkers}$ of walkers and find the number $N_{collector}$ of the walkers that reach the collector. The image charge Q_{image} induced on the collector is given as

$$Q_{image} = -\frac{N_{collector}}{N_{walkers}} Q \tag{4.7}$$

The derivation of this equation is based on the fact that the Green's function of a point charge is related to the first passage probability[19] of a random walker starting at the position of the charge [113]. This relation is given as

$$p(\vec{r}_B;\vec{r}_0) = -\frac{\partial G(\vec{r}_B;\vec{r}_0)}{\partial \vec{n}} \tag{4.8}$$

where $p(\vec{r}_B;\vec{r}_0)$ is the first passage probability distribution of a random walker starting at $\vec{r}_0$, and $\frac{\partial G(\vec{r}_B;\vec{r}_0)}{\partial \vec{n}}$ is the normal derivative of the Green's function G at the boundary. Note that the right-hand side of Equation (4.8) is just the surface charge density. One can easily integrate this equation to obtain Equation (4.7).

The procedure we have described so far would not directly construct a very efficient algorithm because at first glance one would think that the step size of the random walk would have to be much smaller than the smallest length scale of the geometry, i.e., the thickness of the wires making up the Frisch gird. If we chose the step to be of 2 μm, then a walker would take $\sim 2.5\times 10^7$ steps to move 1 cm[20], which means that an accurate simulation

[19] The first passage probability is defined as the probability that a random walker first hits a given site on the boundary.

[20] Note that the mean square displacement is $N\lambda^2$, where λ is the step size.

would be considerably time-consuming. However, it has been shown [112][113] that Equations (4.7) and (4.8) are still valid even with a variable step size for the random walk. Obviously, there is an upper limit for the step size, i.e., the step size must be not larger than the distance ζ from the current position of the walker to the nearest electrode in each step of the walk[21]. Therefore, to minimize the required number of steps and the running time of the simulation, in each step the walker moves to a point uniformly sampled out of the surface of a sphere centered at the previous position that has a radius of ζ, i.e., the walker exits a series of successive spheres. This method was first proposed by Muller in 1956 [112] and now is referred to as the "Walk on Spheres" method. We terminate the walker when it reaches a position that is within a small distance δ of an electrode. This termination strategy was justified by Muller in section 7.2 of his paper [112]. δ was taken to be 0.1 μm in our simulation. A schematic of this process is shown in Figure 4.9.

Figure 4.10 shows how the ratio of the image charge on the collector to the total charge on the ion slab varies with distance z from the collector. To obtain high accuracy, two million walkers were used in the simulation. The starting positions of these walkers were uniformly distributed over the area of the ion slab (see Figure 4.7). Then we repeated the simulation for different values of z to obtain the charge ratio as a function of z, as shown in Figure 4.10. One can see from the figure that the leakage through the Frisch grid increases fast as the ion slab approaches the Frisch grid. The results were fit very well to the following equation

[21] Of course, the step size also needs to be large enough so that the walker can reach an electrode.

$$Q_{image} = -Q\,a \cdot \exp(-z / b) \tag{4.9}$$

where Q_{image} is the image charge induced on the collector, Q is the total charge on the ion slab, $a = 0.0375$, and $b = 0.355\ \text{cm}$.

To perform a more accurate calculation of the leakage current, we have replaced the single slab of ions just considered by a more delicate model. We included the effect that the actual ion slab in the experiments was of a finite thickness. And we also included a correction to allow for the ~12% charge loss at the Frisch grid. To take account of these effects, we now consider an ion slab of thickness w[22]. Suppose that at time t_F the front of the ion slab arrives at the Frisch gird, and at time t_C the rear of the ion slab arrives at the collector. Then we have

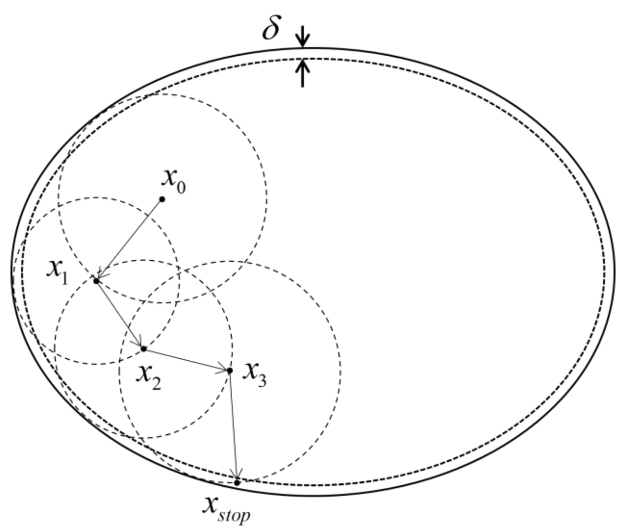

Figure 4.9: Schematic showing the "Walk on Spheres" method. A walker starts at position x_0 and stops at position x_{stop}. Note that this figure does not include the actual geometry of the cell. It only intends to show the concept of the "Walk on Spheres" process.

[22] The diameter is still assumed to be 0.8 cm, as previously discussed.

$$w = v_{drift}(t_C - \frac{z_{FC}}{v_{FC}}) \tag{4.10}$$

where v_{drift} is the velocity of the NEB in the drift region above the Frisch grid, and v_{FC} is the velocity of the NEB in the region between the Frisch grid and collector. At time t_F the profile of the charge density on the slab is taken as

$$\rho = \begin{cases} \rho_0(z), & z_{FC} \le z \le z_{FC} + w \\ 0, & z > z_{FC} + w \end{cases} \tag{4.11}$$

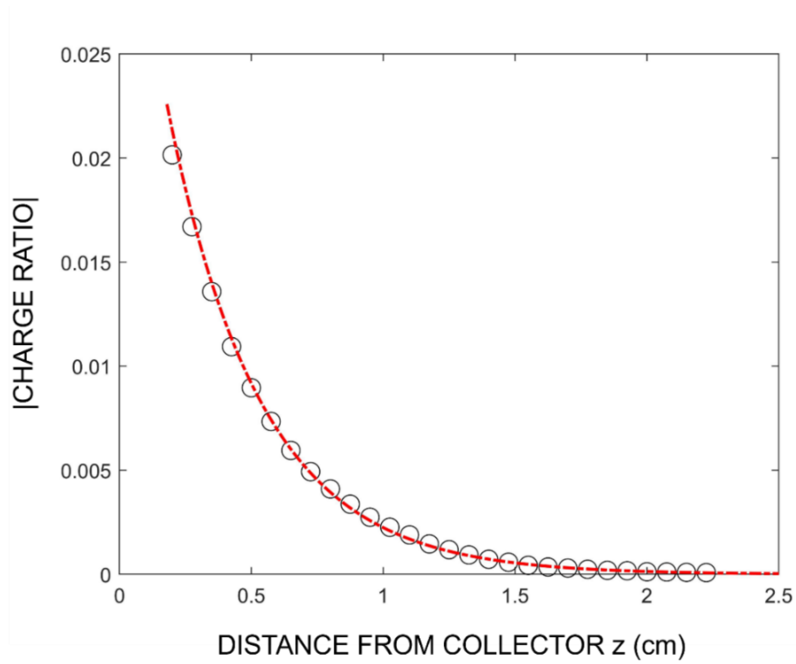

Figure 4.10: Plot of the ratio of the image charge on the collector to the total charge on an ion slab approaching the Frisch grid as a function of distance z from the collector. The cycles are the results from the Monte Carlo simulation, and the dashed line is an exponential fit to these results.

At a later time $t \ge t_F$, the charge density $\rho'(z,t)$ is given by

$$\rho'(z,t) = \rho\left[z + v_{drift}(t - t_F)\right] \tag{4.12}$$

It is not difficult to derive the equation for the leakage current at the collector.

$$\begin{aligned} I_{leakage} &= -\frac{dQ_{image}}{dt} \\ &= \frac{d}{dt}\int_{z_{FC}}^{\infty} \rho_0\left[z + v_{drift}(t - t_F)\right] A_{slab} \cdot a\exp\left(-z/b\right) dz \end{aligned} \tag{4.13}$$

where $A_{slab} = \pi r_{slab}{}^2$ with $r_{slab} = 0.4$ cm. Note that the charge density profile should be chosen so that it reproduces the profile of the measured NEB signal. This requirement gives

$$\begin{aligned} &\rho_0\left[v_{drift}(t - t_F) + z_{FC}\right] \\ &= \frac{dI\left(t\right)}{dt} \cdot \frac{z_{FC}}{v_{drift} \cdot v_{FC}} \cdot \frac{1}{A_{slab} \cdot Tr},\ t_F \le t \le t_F + z_{FC}/v_{FC} \\ &= \frac{dI\left(t\right)}{dt} \cdot \frac{z_{FC}}{v_{drift} \cdot v_{FC}} \cdot \frac{1}{A_{slab} \cdot Tr} + \rho_0\left[v_{drift}(t - t_F - z_{FC}/v_{FC}) + z_{FC}\right], t_C \ge t > t_F + z_{FC}/v_{FC} \end{aligned} \tag{4.14}$$

where $I(t)$ is the measured current signal at the collector[23], and Tr is taken to be 88% to give the approximate charge loss at the Frisch grid. t_F and t_C are chosen to be two time points before and after the arrival time of the NEB, respectively, at which the current is 1% of its peak value.

In Figure 4.11 the calculated leakage current is shown as the dashed curve, and the measured signal is shown as the solid curve. It is obvious that over the time range in which background A seems evident, the calculations for $I_{leakage}$ are much too small to provide an

[23] This equation assumes that the measured signal only comes from the normal electron bubbles arriving at the collector. Note that in fact the measured signal contains background A and the leakage current. However, these two are too small to have any effects on the leakage calculation.

explanation for the measured signals. At a time of 22 msec, for example, the measured current for $\Delta V_{01} = 70$ V is -0.49 pA, while the calculated leakage current is only about -0.12 pA.

Of course, it is necessary to test and confirm the accuracy of the leakage calculation just described. We will discuss this point in section 4.2.2.3.

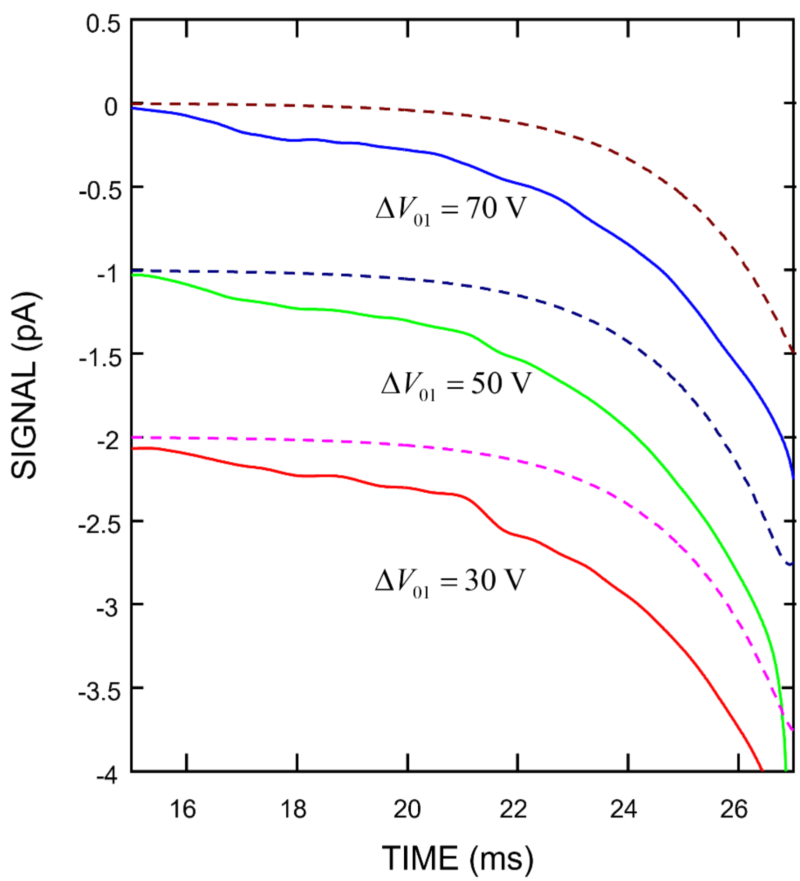

Figure 4.11: Plots of the measured background A and the calculated leakage current through the Frisch grid. The curves are labelled by the voltage difference between grids G0 and G1. The data for ΔV_{01} equal to 30 V and 50 V are offset by 2 and 1 pA, respectively. The temperature was 1.014 K. The drift field was 65 V/cm. The amplitude of the pulse applied to G0 and G1 was held constant at 40 V.

4.2.2.2 Experiments with Electrons from the Plasma

Now we have excluded the possibility that background A only arises from the leakage through the Frisch grid. In this section we will make a comparison between the measured background A signals shown in Figure 4.11 and the signals to be expected from the trapping process described in section 4.2.1 in which the electron wave function only gets partially transmitted into the liquid and thus gets trapped in a bubble smaller than the NEB.

The electron energy distribution $n(\varepsilon)$ in the plasma is given by [114][115]

$$n(\varepsilon)\,d\varepsilon = \frac{2n_{el}}{\Gamma(3/4)}\frac{\varepsilon^{1/2}}{\varepsilon_0^{3/2}}\exp\left(-\varepsilon^2/\varepsilon_0^2\right)\,d\varepsilon \tag{4.15}$$

In the above equation n_{el} is the total number density of electrons and

$$\varepsilon_0 = \Lambda eE\sqrt{\frac{M_{He}}{3m_e}} \tag{4.16}$$

where Λ is the electron mean free path, E is the applied electric field, and M_{He} is the mass of a helium atom. The mean free path Λ of electrons in the vapor is given as

$$\Lambda = \frac{1}{n_{He}\sigma_{el-He}} \tag{4.17}$$

where n_{He} is the number density of helium atoms in the vapor, and σ_{el-He} is the cross section for electron-helium scattering. This cross section at few eV electron energies is about 5.5×10^{-16} cm^2 [116]. Equation (4.15) only holds under the following conditions: 1) the electron energies must be much larger than the thermal energy scale k_BT; this is the case in our experiment, and 2) the electrons lose kinetic energy mainly by means of quasi-elastic scatterings by helium atoms instead of excitations or ionizations of helium atoms.

The electron distribution in the wave vector $\vec{k}$ space is then given as[24]

$$\frac{\hbar^3 n_{el}}{\sqrt{32}\,\pi\Gamma(3/4)m_e^{3/2}\varepsilon_0^{3/2}}\exp\left(-\hbar^4 k^4/4m_e^{\,2}\varepsilon_0^2\right)dk_x dk_y dk_z \tag{4.18}$$

We can calculate the rate at which electrons are incident on the liquid-vapor interface as

$$\int_{-\infty}^{\infty}dk_x\int_{-\infty}^{\infty}dk_y\int_0^{\infty}dk_z\,\frac{\hbar^3 n_{el}}{\sqrt{32}\,\pi\Gamma(3/4)m_e^{3/2}\varepsilon_0^{3/2}}\exp\left(-\hbar^4 k^4/4m_e^{\,2}\varepsilon_0^2\right)k_z A \tag{4.19}$$

where A is the area of the surface where the electrons are incident.

The problem comes down to what happens to an electron of momentum $\vec{k}$ when it is incident on the liquid surface. As far as we are aware, there is no detailed theory of this. One approach is to assume that the liquid provides a smoothly varying potential $V(z)$ that acts on an incident electron; z is the distance measured normal to the interface. For large z, $V(z)$ equals the barrier height V_0 and has a magnitude of 1 eV. If the energy of the electron is less than V_0, there will be no transmission; for electron energy above V_0 there will be partial transmission due to the so-called "reflection above the barrier." A second approach is to allow for scattering of the electron from individual helium atoms in the liquid.

[24] For the momentum distribution, Lifshitz and Pitaevskii [115] also gave a small first order term $f_1(p)\cos\theta$, where θ is the angle with respect to the direction of the applied field. We have tested that this first order term has only a small effect on the calculation.

The helium density profile at the liquid-vapor interface has been measured using X-ray techniques [117][118] and is in reasonable agreement with computer simulations [119]. The measurements [117] found a density profile that went from 10 % of the bulk density to 90% over a distance of 9.2 Å. We can obtain this width if we take the density profile to be given by the expression

$$\rho(z) = \frac{\rho_0}{1+\exp(-z/a)} \tag{4.20}$$

where ρ_0 is the mass density in the bulk liquid and $a = 2.09$ Å. We then take the potential $V(z)$ acting on an electron incident on the interface to be proportional to the density and thus

$$V(z) = \frac{V_0}{1+\exp(-z/a)} \tag{4.21}$$

If an electron reaching the interface has a normal wave vector k_z less than $\sqrt{2m_e V_0/\hbar^2}$, it will be completely reflected. The electron wave function ψ will be partially reflected and partially transmitted if $k_z > \sqrt{2m_e V_0/\hbar^2}$. Then the fraction F [25] of $|\psi|^2$ transmitted into the liquid can be calculated as [120]

$$F = 1 - \frac{\sinh^2\left[\pi(k_z - k_z')a\right]}{\sinh^2\left[\pi(k_z + k_z')a\right]} = \frac{\sinh(2\pi k_z a)\sinh(2\pi k_z' a)}{\sinh^2\left[\pi(k_z + k_z')a\right]} \tag{4.22}$$

where $k_z' = \sqrt{k_z^2 - 2m_e V_0/\hbar^2}$.

[25] This fraction is just taken to be the transmission coefficient of the electron.

With the above equations we can calculate the distribution function of the F values for electrons entering the liquid from the plasma. Given that the radius of the bubble formed in the liquid equals the radius of the NEB multiplied by a factor of $F^{1/4}$, this distribution can then be used to calculate the distribution of transit times through the drift cell, i.e., the current as a function of time. This current is supposed to be proportional to the total number density n_{el} of electrons in the plasma, which is an unknown factor. The value of n_{el} can be chosen by making the integral of the calculated current over the whole range of transit times equal to the value obtained from the measured data. Then ε_0 becomes the only adjustable parameter. Using Equation (4.16) to calculate the parameter ε_0 requires information on the field E_{vap} in the vapor just above the liquid-vapor interface. At first sight one would think that this field is just the voltage difference ΔV_{01} between grids G0 and G1 divided by the distance between these grids. However, even though we have measured the voltage difference ΔV_{01}, it is still not likely for us to perform an accurate calculation for E_{vap} due to the following effects:

1. Since electrons experience a 1 eV energy barrier at the liquid-vapor interface, a layer of electrons will be deposited at the interface. The amount of the deposited charge may vary with the value of ΔV_{01}, i.e., the field just above the interface. It is likely that the electrons start to leave the interface and escape into the liquid when the charge builds up to a critical value.
2. By ionizing helium atoms in the vapor, alpha particles in the region between grids G0 and G1 provide an electron source that does not seem to vary significantly with positions. However, alpha particles do not reach some parts of the G0-G1 region

(see Figure 3.2) since they cannot penetrate the 0.05 cm thick metal disks onto which the grids are attached. Therefore, the ionization rate by alpha particles varies laterally.

3. The fields above and below the interface, i.e., the field in the vapor and the liquid, will be different. Note that the mobility and the number density of the electrons in these two regions are different and may be dependent on the position.

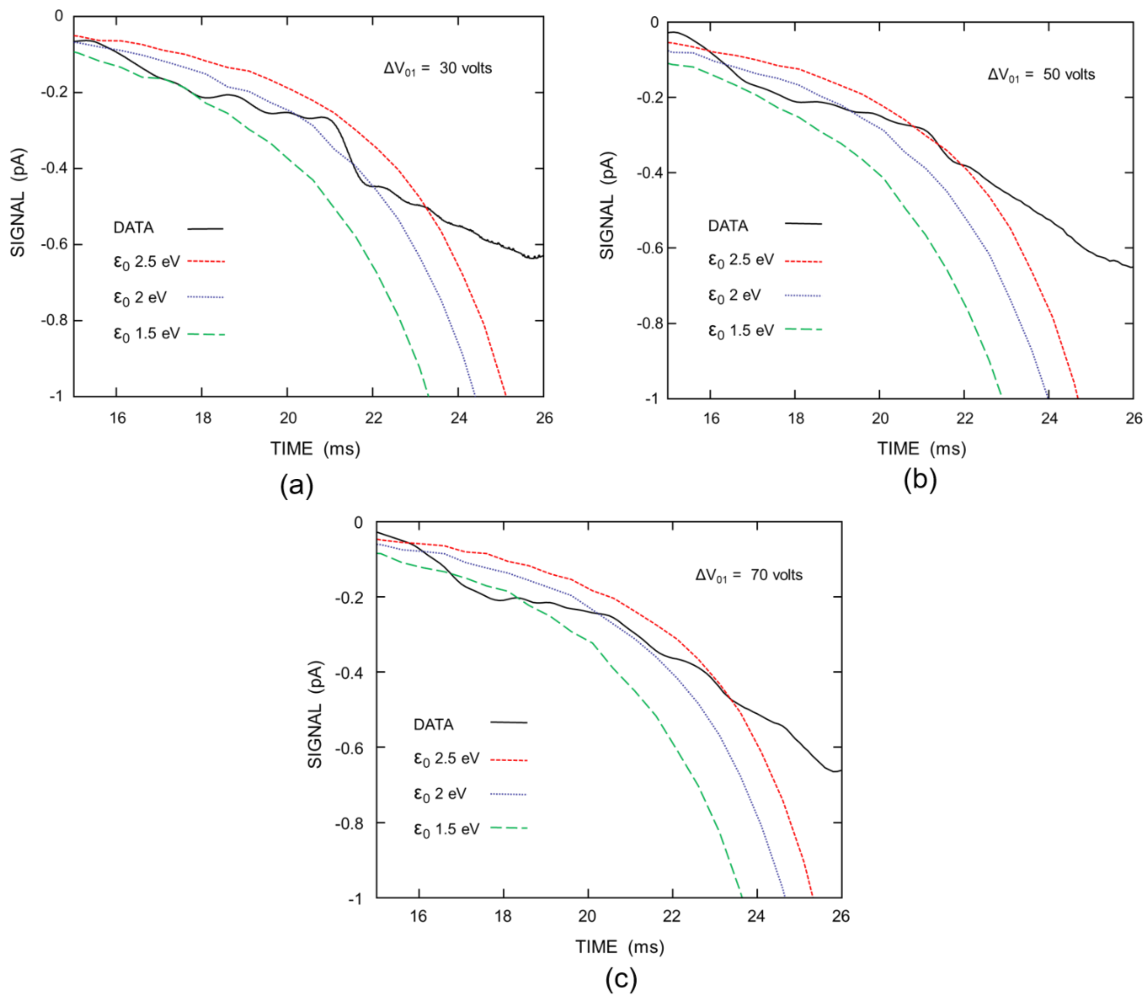

Figure 4.12: The solid curve shows the measured background A data after subtraction of the leakage current. The voltage differences between grids G0 and G1 are (a) 30 V, (b) 50 V, and, (c) 70 V. In each part of the figure, the results for the calculated signal are shown at different values of the parameter ε_0.

We plot the measured data at three different values of ΔV_{01} in Figure 4.12. The calculated leakage current through the Frisch grid has been subtracted from each data trace. In each plot we also show the calculated signals obtained using the method described above, i.e., using Equations (4.19) and (4.22). We include the calculated signals for three different values of ε_0. The values of ε_0 that give a reasonable fit to the measured data do not seem to vary significantly between different values of ΔV_{01}. It appears that the largest discrepancy between the calculations and the measured data occurs within the time range from 90 to 100 % of the arrival time of the normal electron bubble. The calculation is significantly larger than the measured data in this time range. Of course, some approximations/assumptions were made in the calculations. We summarize these as follows:

a) The energy distribution of electrons in the plasma is taken to be Equation (4.15).

b) We take the bubble radius R to be proportional to $F^{1/4}$ and assume that the mobility is proportional to R^{-2}. The charge is assumed to be $-e$ [26].

c) The potential barrier at the interface is assumed to be linearly proportional to the liquid density given by Equation (4.20) with the interface width value measured by Lurio *et al.* [117]. Note that in their paper, Lurio *et al.* had considered the broadening of the interface due to the thermally excited ripplons. Using the simple dispersion relation $\omega^2 = gk + \alpha k^3 / \rho$ with $\hbar\omega / k_B \sim 1\,\mathrm{K}$, the ripplon wavelength is ~33.6 Å. With $\omega / 2\pi = 280\,\mathrm{Hz}$, which corresponds to the frequency of the mechanical vibration of the apparatus, the ripplon wavelength is ~ 0.06 cm. The rms

[26] See the discussion in section III.E of ref. [67].

surface displacement obtained by employing all the ripplon modes is ~3 Å at 1 K [121].

d) The scattering of electrons from individual helium atoms is not considered; the potential is assumed to vary smoothly with position.

e) The image potential across the vapor/liquid interface is not included. Cheng *et al.* [122] proposed a model that considers the non-uniform liquid density profile at the interface. Cheng *et al.* only used their model to calculate the bound states of the electron at the interface.

Of these, assumption d) seems to be the most questionable. The number density in liquid helium at ~ 1 K is 2.17×10^{22} cm^{-3} and so the electron mean free path in the liquid is $\Lambda_{liq} = 8.39$ Å, i.e., comparable to the width of the surface.

4.2.2.3 Experiments with Positive Helium Ions

In this section we report on experiments with positive helium ions performed to test our theory of background A and the Frisch grid leakage. A positive helium ion in the liquid polarizes the surrounding neutral helium atoms and forms a "snowball" because of the increase in liquid pressure. As previously discussed, there have been many measurements of the mobility of these "snowballs;" their mobility was found to be about twice that of the normal electron bubble. It is interesting to consider the "reflection above the barrier" for the positive ions. When a He^+ ion collides with a helium atom in the vapor, it will lose much of its kinetic energy because the masses are nearly the same. As a result, a He^+ ion incident on the liquid-vapor interface will typically have an energy on the order of $eE\Lambda_{vap}$, where Λ_{vap} is the mean free path of the positive ion in the vapor, and E is the applied field. Therefore, for most of the positive ions that are incident on the interface, $\pi k_z a$ in Equation (4.22) will be much greater than unity[27]. Given that for a positive ion the potential in the bulk liquid is negative relative to the vapor, $\pi k_z' a$ will be even greater than $\pi k_z a$. Thus, it can be deduced from Equation (4.22) that the "reflection above the barrier" will be neglectable for the positive ions, and one should expect that the "tail" prior to the arrival of the positive ions only consists of the signal resulting from the leakage through the Frisch grid. This indicates that experiments with positive ions can be used to check our calculation for the leakage.

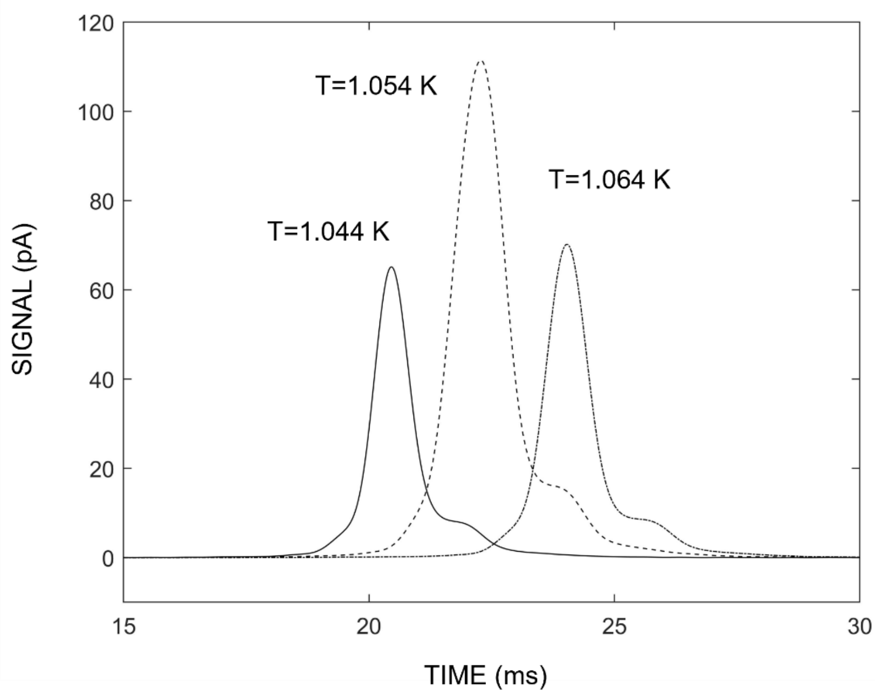

Figure 4.13: Current of positive ions detected at the collector as a function of time at three different temperatures: 1.044, 1.054 and 1.064 K. The drift field was 65 V/cm.

---

[27] Note that the mass ratio of He^+ to electron is about 10^4.

To conduct measurements of positive ions, the polarities of all the voltages applied in the cell were reversed. Representative data from the experiments are shown in Figure 4.13. It appears that there are additional peaks shown in the data. The observation of multiple positive helium ions has been discussed in section 3.4.

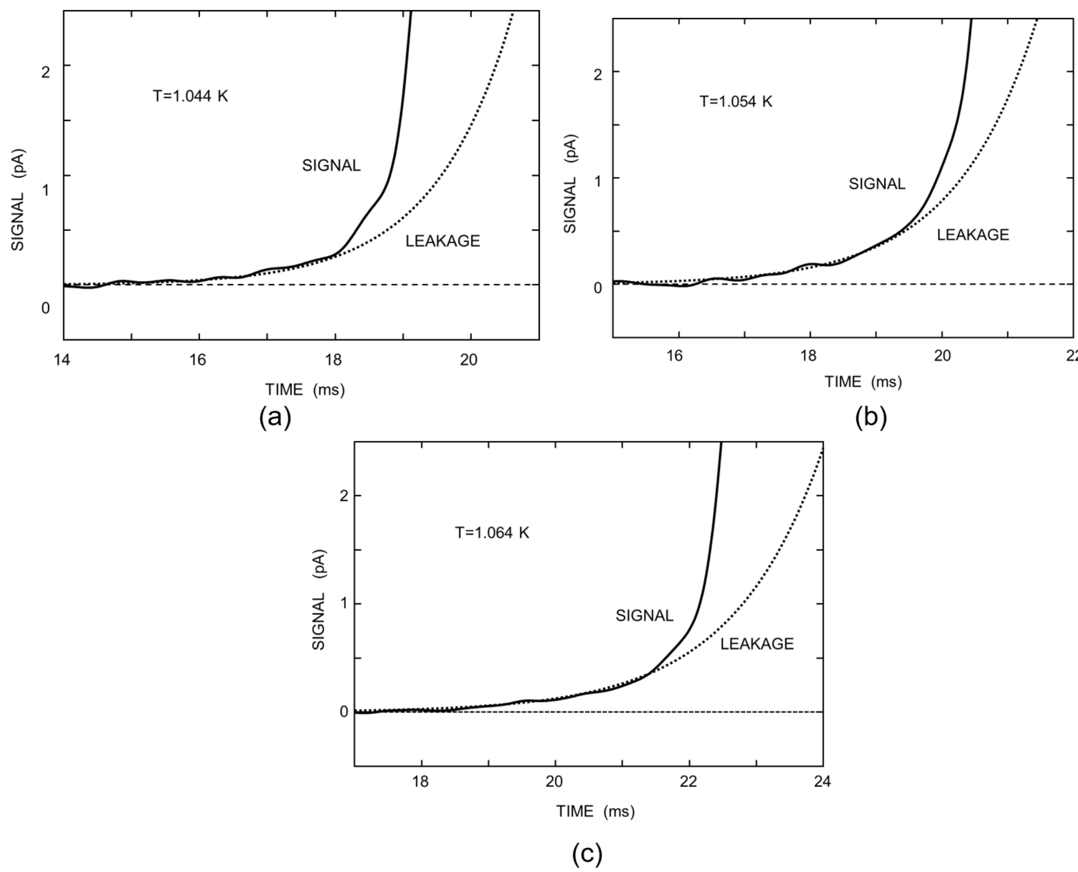

Figure 4.14: Current of positive ions arriving at the collector as a function of time at three different temperatures: (a) 1.044 K, (b) 1.054 K, and (c) 1.064 K. The solid curve shows the measured data of the positive "tail" discussed in the text. The dotted curve shows the calculated leakage current.

In Figure 4.14, we replot the positive ion data in the time range before the arrival of the main peak. The vertical scale of each plot has been greatly expanded, and one can clearly see a small "tail" signal before the arrival of the main peak. However, it appears that the magnitude of this tail is significantly smaller than that of the background A signal for negative ions shown in Figure 4.11. For example, this tail becomes buried in noise at a time of about 70-75% of the arrival time of the main peak, whereas background A is still well above the noise level at the same time point. Now we make a comparison between this tail and the leakage through the Frisch grid. The leakage was calculated as follows. The integral of the current over the time range close to the main peak was found first. This gave the total charge Q arriving at the collector. The results were 0.069, 0.166 and 0.088 pC at the temperatures 1.044, 1.054 and 1.064 K, respectively. We then took the total charge as an infinitesimal ion slab traveling at the measured drift velocity of the positive ion He^+ and calculated the image charge on the collector using Equation (4.9). Lastly, we calculated the leakage current as the first derivative of the image charge with respect to time. The results are shown as the dotted curves in Figure 4.14.

Figure 4.14 shows that the calculated signal from the leakage through the Frisch grid agrees well with the measured "tail". This indicates that in contrast to what we have seen for the negative ions, the only signal in the "tail" before the main peak of the positive ions arises from the leakage through the Frisch grid, as we expected.

4.2.2.4 Experiments with Alpha Source Immersed in the Liquid

It is interesting to study electrons that have been generated in the liquid and have not been reflected or transmitted at the liquid-vapor interface. Do these electrons give a measured signal with a continuous background similar to that produced with electrons from the plasma? Or are only normal electron bubbles produced?

In the experiments described so far, the alpha source has been positioned in the vapor above the liquid. The alpha particles ionize helium atoms in both the helium vapor and in the part of the liquid that is very close to the surface[28]. When the field between G0 and G1 is on the order of 100 V cm^{-1} or less [69], alpha particles that enter the liquid cause ionization but nearly all the resulting electrons are pulled back to a positive ion and recombine.

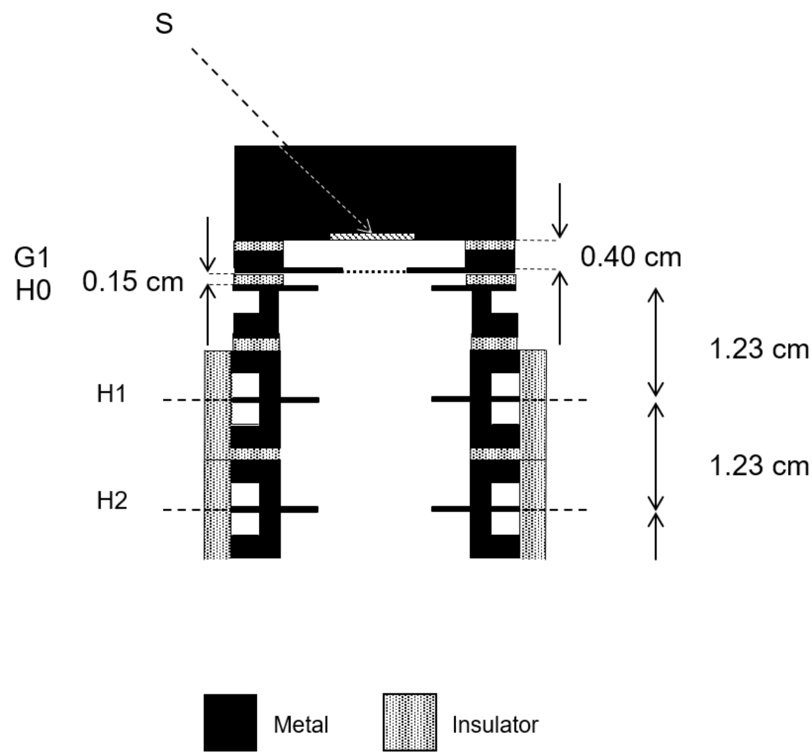

Figure 4.15: Modification of the cell. Grid G2 was replaced by a ring disk without wire grid. The spacing between the source and grid G1 was adjusted. The voltage on the source was held at -1300 V. The voltages on G1 and H0 were held at -310 V and -400 V, respectively. To produce a pulse of electrons, a gate pulse of -450 V was applied to G1. Other cell parts are omitted in this figure.

[28] Note that the range of alpha particles in the liquid is only about 250 μm.

Consequently, most of the electrons that produce the signal measured in section 4.2.2.2 come from the plasma and are incident on the surface of the liquid.

To produce electrons in the liquid, sufficient liquid was added to the cell so that the alpha source was immersed in the liquid and the applied dc field in the region of the liquid that is close to the source was increased. Details of the modification of the electrodes at the top

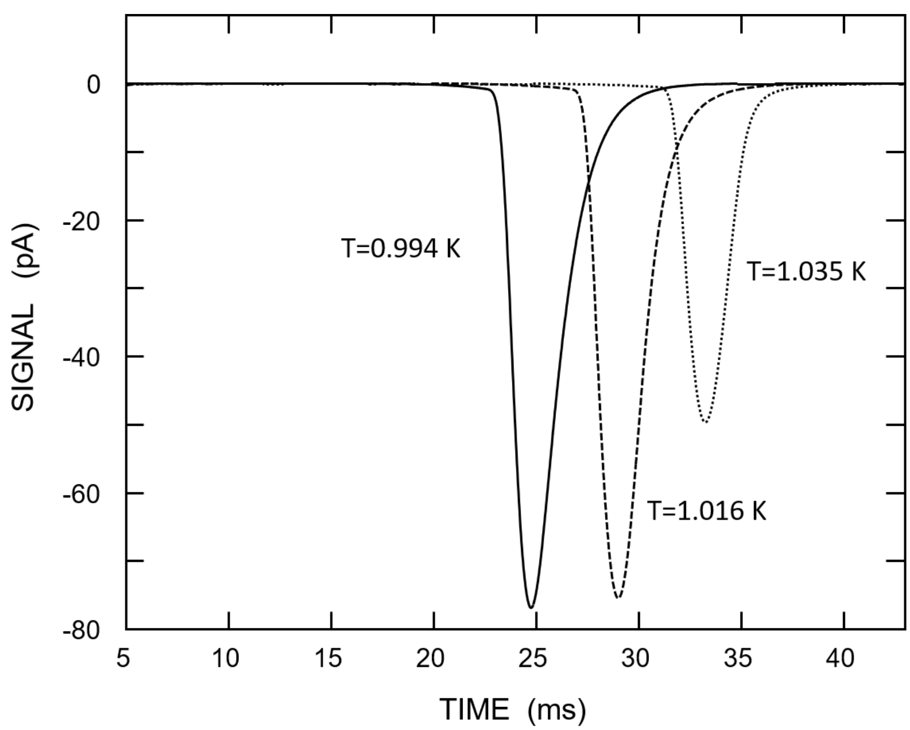

Figure 4.16: Current detected at the collector as a function of time. The alpha source is immersed in the liquid. The drift field was 65 V/cm.

of the cell are shown in Figure 4.15. The measured signals at three different temperatures are shown in Figure 4.16. The magnitudes of the signals are on the order of 50 pA. Figure 4.17 shows the comparison between the measured signal and the calculated leakage signal in the time range between 50% and 90% of the NEB arrival time. The measured signal and the calculated leakage are almost identical thus indicating that the measured signal only comes from normal electron bubbles, and there is almost no contribution from background A. This is an indeed interesting result. The average energy lost by an alpha particle in producing one electron (the so-called W value) has been measured by Ishida *et al.* [123] to be 43.3 eV. However, a fraction of the energy lost by the alpha goes into exciting other helium atoms. The estimated average kinetic energy of the recoil electrons once they have dropped below the excitation threshold is estimated to be 8 eV[29]; still much larger than the barrier energy $V_0 = 1\,\mathrm{eV}$.

4.2.3 Discussion

In this experiment electrons from a plasma in helium vapor are incident on the surface of superfluid helium. Negative ions are produced in the liquid and the mobility of these ions has been measured. We have focused attention on one particular component of the signal, which we call background A. Background A has the remarkable property that the measured signal varies smoothly with arrival time. All these ions are found to have a mobility that is larger than that of the so-called normal electron bubble.

We have proposed that electrons produced in the plasma are partially transmitted into the liquid and become trapped as "electron bubbles" below the liquid surface. Each bubble contains a different fraction F of the integral of $|\psi|^2$ and consequently has a different size

[29] See section II.B of ref. [124].

and mobility. The experimental results support the proposal that stable electron bubbles can be produced which contain only a fraction of the electron wave function.

We have made a number of tests of the experimental procedure; particular attention was paid to the operation of the Frisch grid. The leakage through this grid was calculated using the Monte Carlo method as described in the section 4.2.2.1. The results of the simulation were confirmed by experiments with positive helium ions (see section 4.2.2.3), and excellent agreement was found.

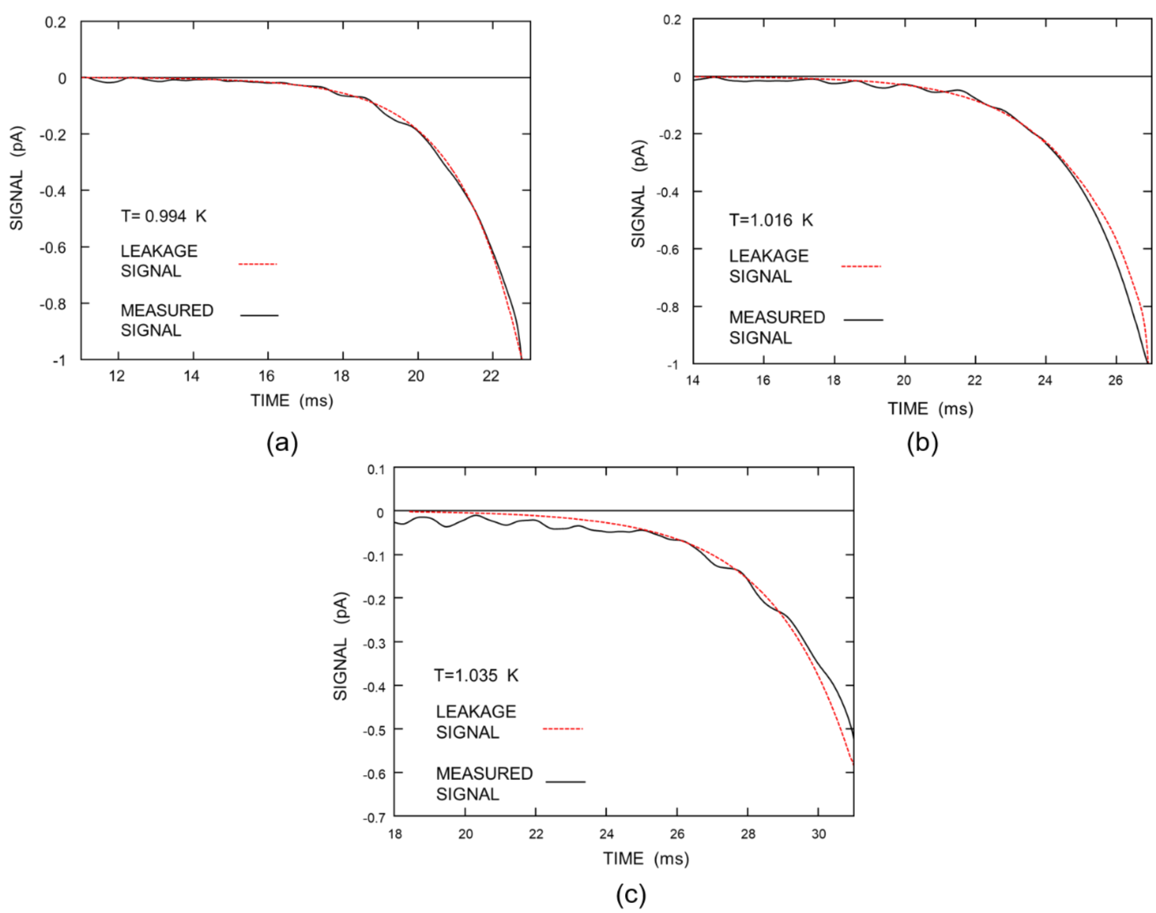

Figure 4.17: Current detected at the collector as a function of time at three different temperatures: (a) 0.994 K, (b) 1.016 K, and (c) 1.035 K. The solid curve shows the measured signal. The dashed curve shows the leakage current calculated by using the method described in section 4.2.2.1.

It is interesting to consider other possible explanations of the experimental data and we now mention what would be needed. The key challenge is to explain how there can be a smooth background signal. A first possibility is to propose that in the liquid there are a number of different ion species each with a different mobility and which decay into other ions. For this proposal to work, the decay time would need to be of the same general order as the transit time for the signal through the cell. But then the shape of the signal would be dependent on the magnitude of the drift field. This is not consistent with the experimental results.

A second possibility is to propose that there is only one ion species but the mobility of these ions changes with the value of some parameter of the ion. For example, it could be proposed that these ions are not spherically symmetric, and to some degree retain the direction of an axis while they travel through the drift region. Another possible approach would be to propose that each ion entering the liquid at the top of the drift region has some type of vibration that changes the mobility. A distribution of initial vibration amplitudes could possibly result in the continuous background signal. This approach requires that the proposed vibrations are not attenuated too rapidly and continue for sufficient time to give the continuous background signal.

There are several experiments that would extend the results obtained so far:

1) It would be interesting to determine if the bubbles we have been studying have a finite lifetime. A possible approach is described as follows. As in the mobility experiments previously described, the gate grids are used to bring a pulse of negatively charged ions into the cell. Then the drift field is turned off before these ions

can reach the collector electrode. After the field has been off for a time t_{off}, the drift field is then turned back on and the strength of the signal reaching the collector is measured. The problem with this approach is that during the time interval in which the applied drift field is turned off, the ions still move a significant distance due to the space charge effect and diffusion. This movement will make the ions end up at an increasing distance from the cell axis and an unknown number of them being collected by the homogenizer disks, and therefore not reaching the collector. To overcome this problem, it would be necessary to have a cell of larger diameter and some way of making corrections for space charge and diffusion would need to be found.

2) Measurement of the cavitation threshold for the electron bubbles with $F < 1$. A number of experiments have been performed to measure the negative pressure at which normal electron bubbles ($F = 1$) become unstable and grow without limit. These measurements have been performed using ultrasound to produce a transient negative pressure [125][126]. The magnitude of the critical negative pressure for bubbles with $F < 1$ has been calculated and increases as F decreases [127]. A measurement of the critical pressure could be used to test this calculation.

3) Finally, it would be very interesting to make measurements on other materials. This requires a liquid in which a stable bubble is formed when an electron enters, i.e., helium-3, hydrogen, deuterium, and neon[30]. Such measurements would provide an opportunity to study bubbles in a classical fluid.

[30] See the discussion in ref. [74].

4.3 Study of Background B

4.3.1 Experiments

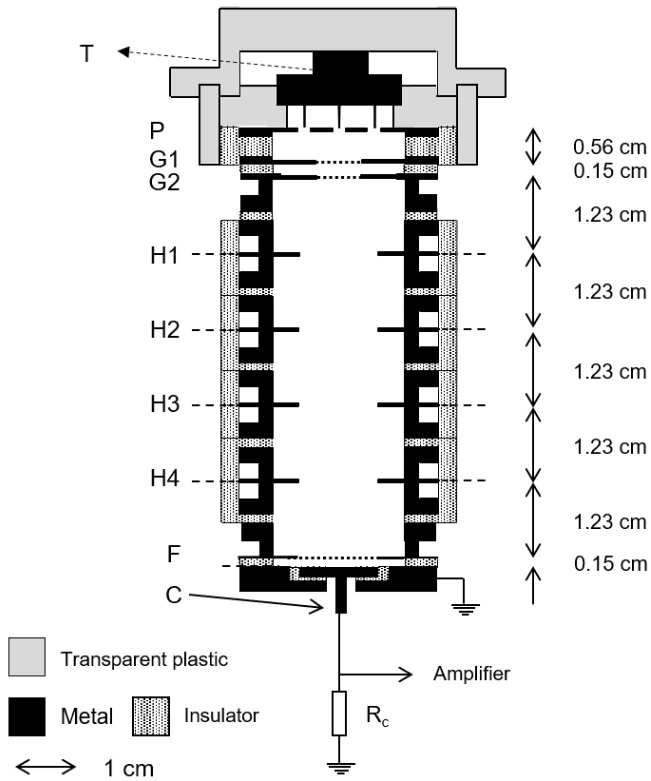

Figure 4.18: Cross section of the experimental cell. Four tungsten tips (T) are mounted at the top. A perforated plate (P) is positioned below the tips. More details are described in the text. This figure is adapted from ref. [25].

In the experiments just described in section 4.2, the sudden change in the background signal as shown in Figure 4.2 was not observed. It was reported in ref. [25] that the background B data shown in Figure 4.2 were taken when the plasma was unstable[31]. To further

[31] See page 91 of ref. [25] and page 36 of ref. [27].

investigate the conditions under which background B occurs, new measurements have been performed.

The cell geometry was nearly the same as that in the previous experiments of Wei *et al*. [25]. A schematic is shown in Figure 4.18. Four tungsten tips were installed on a brass holder at the top of the cell, one at the center of the holder and three at the vertices of an equilateral triangle around the center. The end of each tip and the top of the perforate plate P were roughly at the same height. The liquid level was approximately 2 mm above the gird G1. Sufficiently large negative voltages were applied between the tips and the perforated plate in order to maintain a stable plasma in the vapor. The functioning of other parts was the same as described in Chapter 3.

In Figure 4.19, we show data taken at three different temperatures: 1.030, 1.055, and 1.070K. The voltage on the tips is given in the figure. The voltages on P, G1 and G2 were held constant at -440 V, -390 V, -400 V, respectively. The amplitude of the gate pulse was held constant at 22 V. The drift field was 65 V/cm. At each temperature, the upper dashed curve in Figure 5.19a shows the signal from background A, and the lower solid curve shows the signal from the sum of backgrounds A and B (background A+B). As shown by the data, there is a sudden change in the background signal, i.e., background B occurs, after the tip voltage is only varied by 7-10 volts. However, the profile of normal electron bubble peak remains almost the same, as shown in Figure 4.19b. It appears that the tip voltage that is needed for background B to occur decreases as the temperature increases.

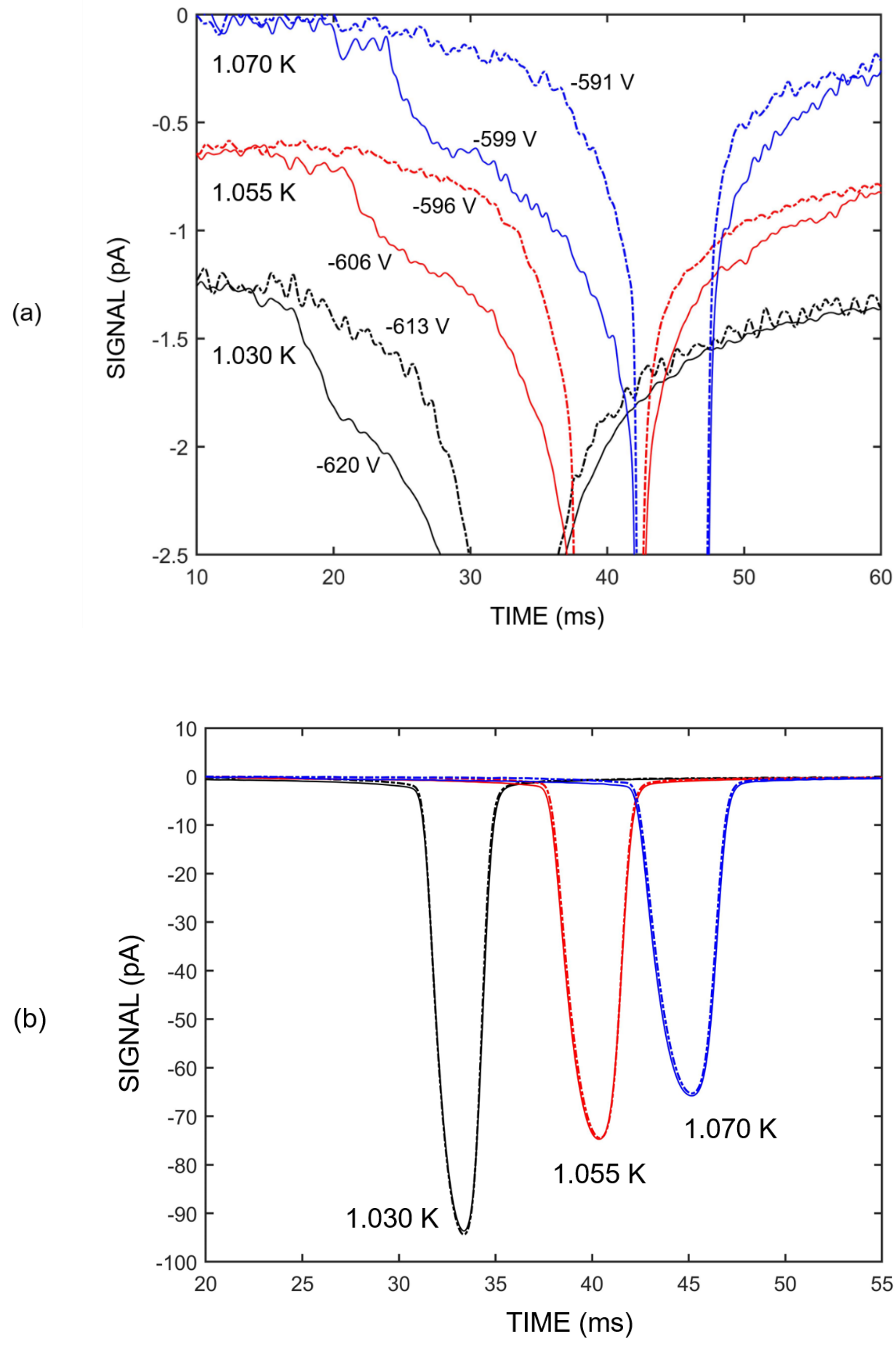

Figure 4.19: Current detected at the collector as a function of time at three different temperatures. In (a), the curves are labelled by the voltage on the tips. The same data are replotted in (b) with a larger y-axis limit to show the complete peak of the NEB. The plots in (a) are offset for clarity.

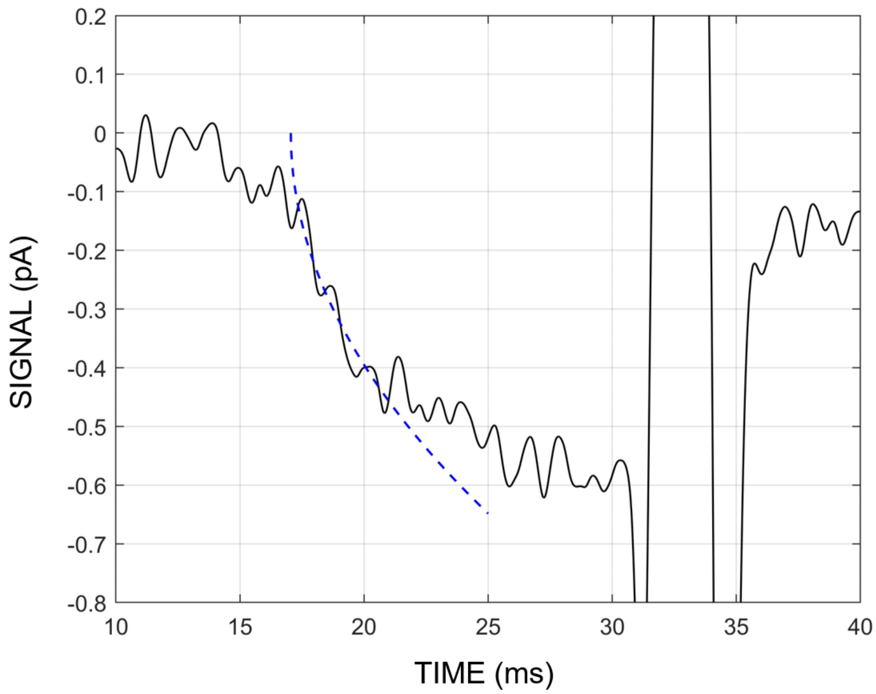

Figure 4.20: Background B obtained by subtracting background A from background A+B. The temperature was 1.030 K. The black curve shows the results for background B. The large fluctuation in the time range between 30 and 35 ms is due to the difference in the normal electron bubble peak. The blue curve shows a plot of $A\sqrt{t-\tau_B}$, where τ_B is the starting time of background B, which is roughly half the arrival time of the normal electron bubble, and A is a constant.

In order to obtain the profile of background B, the background A signal was subtracted from the background A+B signal. The result obtained at 1.030 K is shown in Figure 4.20. Background B begins at time τ_B, which is about half the arrival time of exotic ions, and is proportional to $\sqrt{t-\tau_B}$ when time t is close to τ_B. The temperature dependence of τ_B is shown in Figure 4.21. The results can be fitted reasonably well to the equation $\tau_B \propto \exp(-\Delta_B / T)$ with $\Delta_B = 8.95\,\mathrm{K}$, which indicates τ_B varies with temperature in the same way as the arrival time of the exotic ions does. These findings are consistent with the previous experiments of Wei *et al.* [25] as summarized in section 4.1.

Note that the background B profile obtained in the present experiment is not exactly the same as that obtained in the previous experiments of Wei *et al*. An example of the background B profiles obtained from their data is shown in Figure 4.22. The profile shown in Figure 4.22 has an obvious upward trend in the time range close to the arrival time of the normal electron bubble. This is not evident in the present experiment, as shown in Figure 4.20. The reason is not fully understood yet. It is likely that the profile of background B, not only the magnitude, depends on the voltage on the tips.

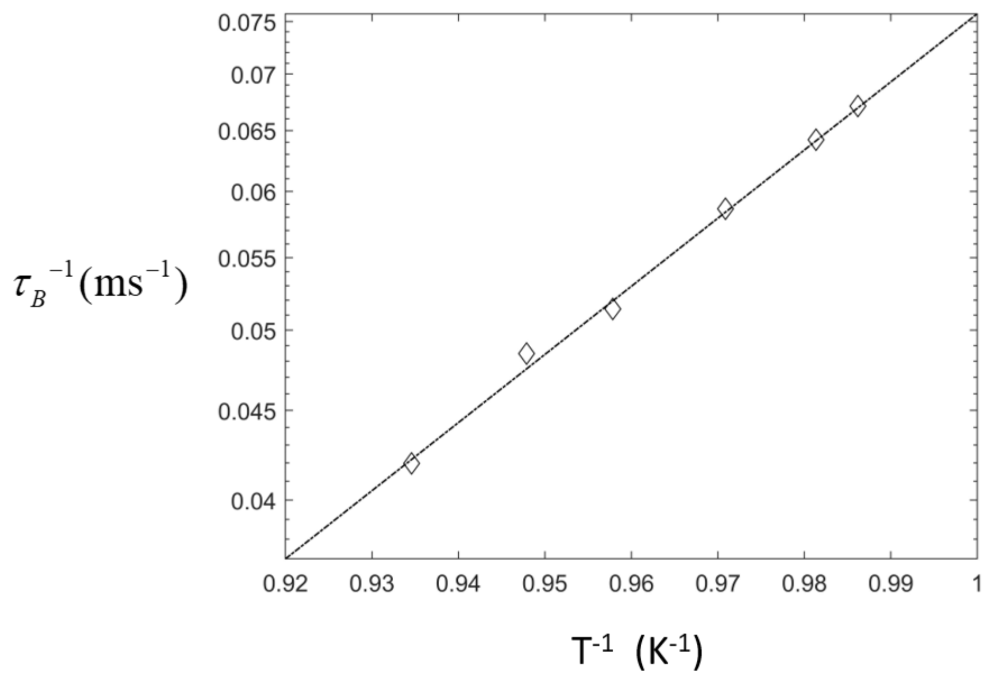

Figure 4.21: Starting time of background b as a function of temperature. The line is a fit to the data assuming $\tau_B \propto \exp(-\Delta_B / T)$.

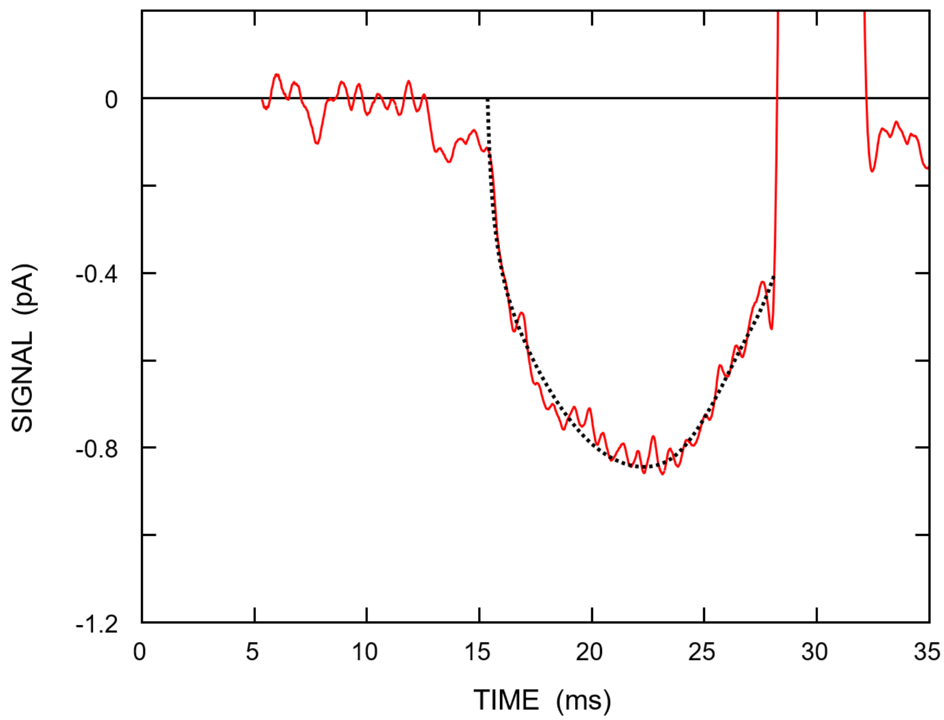

Figure 4.22: Background B obtained from the data of Wei *et al*. The black curve shows a guide to the eye. This figure is adapted from the previous review article [74].

4.3.2 Discussion

There is so far no theory proposed for background B. A theory for background B is required to explain the following experimental findings:

a) Background B appears to come from real ions with a continuous distribution of mobility.

b) Background B has a cutoff time τ_B, which is about half of the arrival time of the NEB. And the magnitude of background B is proportional to $\sqrt{t-\tau_B}$ near the cut-off. Thus, the mobility distribution must also have a cutoff μ_B (as an upper limit), which is about twice of the NEB mobility. And near the cutoff the mobility distribution is proportional to $\frac{1}{\mu^2}\sqrt{\frac{1}{\mu}-\frac{1}{\mu_B}}$.

c) Background B abruptly occurs when a small change in the tip voltage is made.

Of these, c) was observed in the experiments using sharp tips to maintain a plasma in the vapor. More generally, the sudden occurrence of background B may be dependent on the characteristic of the plasma. It is difficult to accurately describe the plasma characteristic, because it can be affected by a large set of parameters, including the type of source, the cell geometry, the voltages on the electrodes, the temperature, the liquid level, etc.

It is possible that background B also comes from bubbles that only contain a fraction F of the electron wave function. The values of F could have a continuous distribution that gives the correct profile of background B. However, we do not know what mechanism can produce such bubbles.

Chapter 5

Experimental Investigation of Photo-Excitation of Electron Bubbles

The 1S→1P optical transition energy of an electron bubble in superfluid helium was measured to be about 0.1 eV at zero pressure. In previous experiments it was found that the 1S→1P transition could produce a photocurrent. This current was believed to arise from electron bubbles escaping from quantized vortices. In this chapter we report on experiments in which we used a caron dioxide (CO_2) laser of wavelength 10.6 μm to excite electron bubbles trapped on quantized vortices. The mobility of the negative ions escaping from the vortices was then measured in a time-of-flight cell.

5.1 Previous Works

In 1967 Northby and Sanders [128][129] investigated the effect of infrared light on the mobility of negative ions in superfluid helium. The apparatus they used consisted of a Cunsolo device [17] immersed in the liquid. At the top of the device, a ^{210}Po alpha source was used to provide a source of electrons by ionizing helium atoms in the liquid. Electrons were then directed to a drift region between two grids G1 and G2. Light from a xenon arc lamp was directed into the drift region after passing through a gating monochromator. A square-wave field was applied between G1 and G2. The frequency of the square wave was adjusted so that the transit time it took for normal electron bubbles to travel from G1 to G2 was slightly larger than one half of the period. This had the consequence that no normal electron bubbles would be able to reach the collector below G2. Only negative ions with higher mobility, such as electrons ejected from bubbles by the infrared light, could result in a current at the collector. They measured the photocurrent as a function of photon energy and found a peak at about 1.21 eV. This energy was supposed to relate to photo-ejection.

Later Zipfel and Sanders [130][131] made similar measurements at pressures up to 230 psi. They observed that the peak previously detected by Northby and Sanders shifted towards higher photon energies as the pressure was increased. They also detected another peak at a lower energy. This peak appeared at ~0.5 eV at 10 psi and disappeared below 10 psi.

To interpret these photocurrent experiments, Miyakawa and Dexter [132] calculated the optical absorption of electron bubbles at different pressures. They concluded that the low energy peak detected by Zipfel and Sanders was due to the 1S→2P transition. They also calculated the 1S→1P transition energy and determined that this energy should correspond to a wavelength of about 12 μm at zero pressure. This calculation was confirmed by Grimes and Adams by making photocurrent measurements [133] and direct optical absorption measurements [134]. The 1S→1P transition energy measured by Grimes and Adams is shown in Figure 5.1. At zero pressure the transition energy was measured to be 0.102 eV.

The mechanism of the photocurrent induced by the photo-excitations of electron bubbles from the ground state to an excited state, such as 1S→1P and 1S→2P, is still not fully understood. One possibility is that the photocurrent comes from electron bubbles trapped on quantized vortices. Miyakawa and Dexter [132] suggested that the thermal energy released by a bubble during the relaxation process following photo-excitation would raise the local temperature in the liquid and then release the bubble from vortices. We take the experiment of Zipfel and Sanders as an example. Electron bubbles could be trapped on vortices distributed between G1 and G2. Then if the bubbles escape from the vortices after an optical transition, they will be able to reach the collector and contribute to the detected photocurrent.

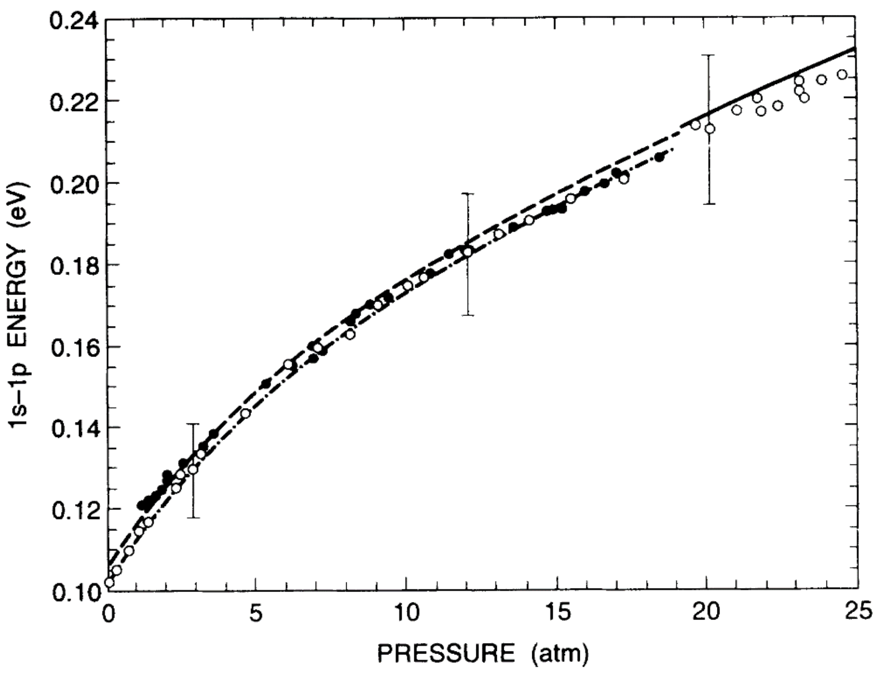

Figure 5.1: The 1S→1P transition energy at 1.3 K as a function of pressure, taken from Grimes and Adams [134]. The open circles are results from their photocurrent measurements, and the filled circles are results from their optical absorption measurements. The curves show their calculations using different models.

Another possibility is the "fission theory" [25][67]. After the electron in a bubble experience an optical transition, for example, from 1S to 1P, the shape of the bubble will start to evolve with time until it reaches an equilibrium, which is a peanut shape for the 1P state. However, computer simulations by density functional theory for the 1S→1P transition [110][135] shows that if the pressure in the liquid is above 1 bar, the bubble shape will go past the equilibrium, and eventually, the bubble will break into two. Maris [67] also pointed out that there is a feedback mechanism that drives a breaking 1P bubble to divide into two equal parts. Smaller bubbles have a higher mobility and thus could contribute to the photocurrent detected in the previous experiments.

In the experiments described above, the mobility of the negative ions was not measured. In order to investigate the mobility change due to photo-excitation, Wei *et al*. [25][27][136] performed mobility measurements in a time-of-flight cell similar to what has been described in section 3.2. They used field emission tips or beta radioactive source to produce electrons. They excited the electrons from the ground state (1S) to the 1P state by using a CO_2 laser of wavelength 10.6 μm. The electron bubbles in their experiment were expected to get trapped on vortices and get knocked off after the application of light. The mobility of these bubbles was then measured. Surprisingly, they observed negative ions which have mobility higher than that of the NEB. An example of their results obtained with field emission tips is shown in Figure 5.2.

Wei *et al*. measured the temperature dependence of the mobility of these objects and found that the temperature dependence was very close to that of the NEB. And more surprisingly, they observed completely different objects in the experiments with a beta source (^{63}Ni).

The nature of the objects seen by Wei *et al.* is not known yet. Two possibilities have been considered. One possibility is that these objects are just normal electron bubbles trapped on vortices located at different positions in the drift region. The CO_2 light was usually directed to the top of the drift region. However, the light could be scattered down to some lower places where there were electrons trapped on vortices. After being knocked off these electrons would travel a shorter distance and reach the collector earlier. The other possibility is the fission theory as discussed previously.

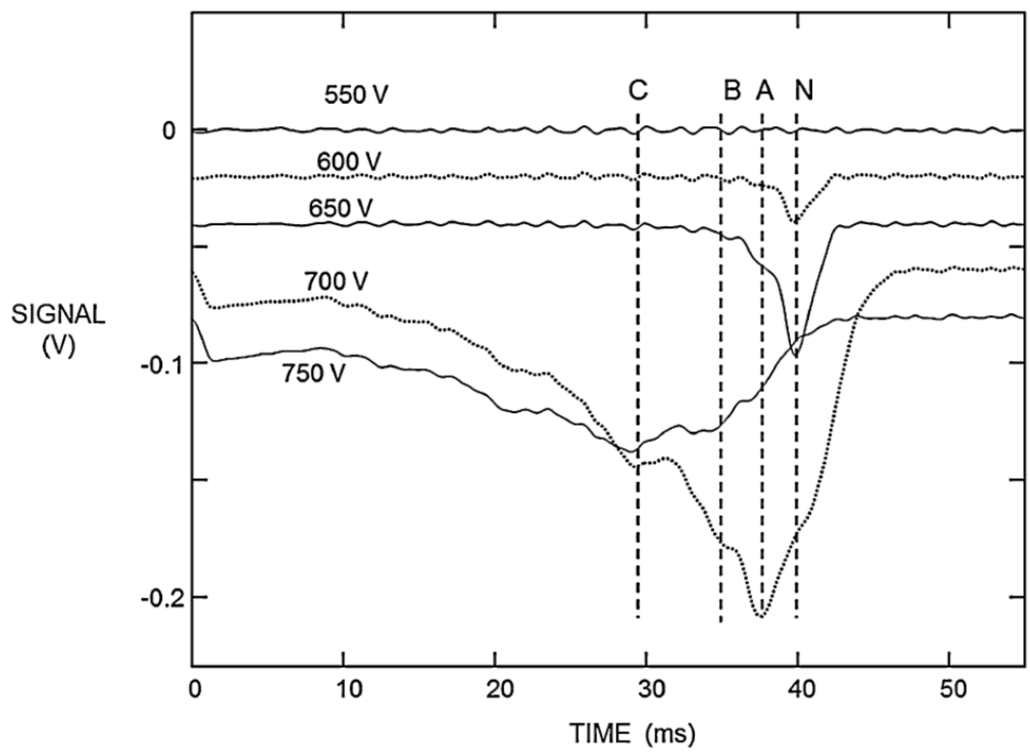

Figure 5.2: Voltage signal detected at the collector as a function of time, taken from Wei *et al.* [136]. This dataset was taken with a field emission tip. The curves are labelled by the voltage on the tip. The signal from the NEB is labelled as "N." Three other objects A, B and C reach the collector at earlier times.

In the present experiment we continued the work to investigate the mobility change due to photo-excitation. And we report on experimental results and discuss possible explanations in this chapter.

5.2 Apparatus

5.2.1 Cell Configuration

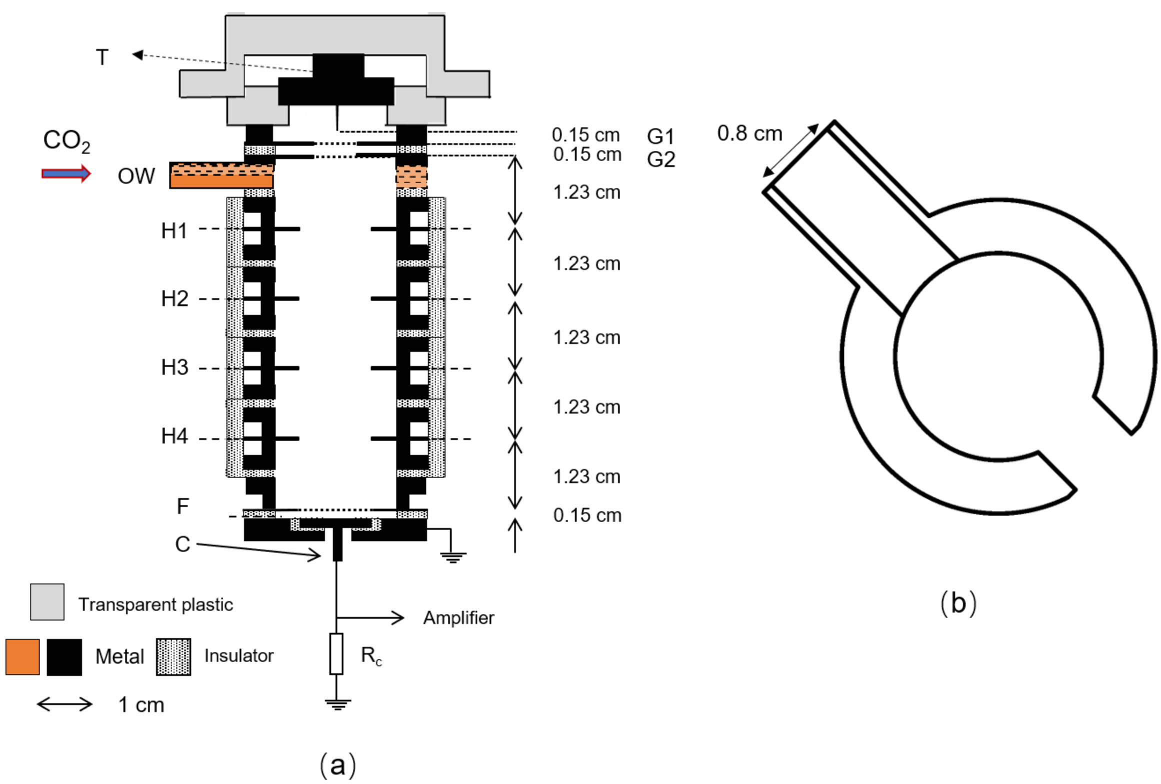

Figure 5.3: (a) Cross section of the experimental cell. The field emission tip T was placed at approximately 0.15 cm above the grid G1. The optical waveguide OW was placed below the gird G2. (b) Cross section of the optical waveguide. The view orientation of (b) is normal to that of (a).

The experimental cell was similar to that used in the previous experiments by Wei *et al*. [136]. A schematic of the cell cross section is shown in Figure 5.3. To produce electrons, we used a field emission tip immersed in the liquid. The method to prepare this tip was described by Kawasaki *et al*. [137]. We coated a section of 0.010" dia. tungsten wire with a layer of carbon nanotubes (CNTs). A field emission tip of this type has a low threshold voltage for field emission. The tip was positioned at 0.15 cm above the G1 grid. The spacing between grids G1 and G2 was 0.15 cm. The inner diameter of G1 and G2 was 0.8 cm.

The CO_2 laser beam was directed into the cell through a brass optical waveguide OW below G2. The waveguide has a rectangular opening that is 0.8 cm wide and 0.2 cm high. To reduce the reflection, the waveguide was chopped on the outgoing side, as shown in Figure 5.3b. The top of the opening was placed at 0.05 cm below G2. Other parts of the cell, such as homogenizers H1-H4, the Frisch grid F and the collector C, were as described in section 3.2.

5.2.2 CO_2 Laser and Optical Windows

The CO_2 laser[32] used in the present experiments has a wavelength of 10.6 μm (photon energy: 0.117 eV) [138]. According to the measurements by Grimes and Adams (see Figure 5.1), the pressure at which the transition energy is close to 0.117 eV is around 1 bar[33].

In the continuous wave (CW) mode, the laser has a maximum output power on the order of 5 Watts. The laser beam has a diameter of several millimeters and a full angle divergence

[32] Model J48-1, SYNRAD Inc., 4600 Campus Pl, Mukilteo, WA 98275, USA.
[33] The full line-width at half maximum is approximately 1/6 of the transition energy [134].

of 4 milliradians. The beam shape is square at the output aperture and changes to circular after traveling 1 meter or more.

The laser uses pulse width modulation (PWM) to control its output power. PWM controls the power-on time of the internal RF amplifier of the laser, and thus the laser output power is controlled by adjusting the pulse width (PWM duty cycle). The output power as a function of PWM duty cycle is shown in Figure 5.4.

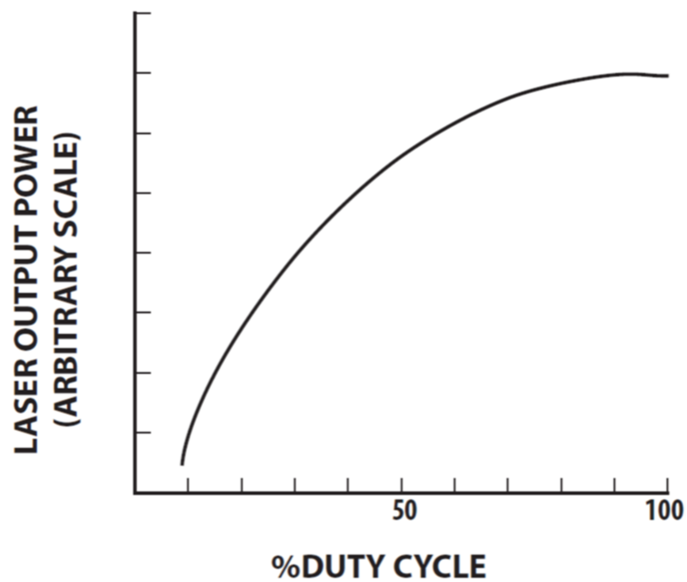

Figure 5.4: Average laser output power as a function of PWM duty cycle, taken from the operation manual [138].

The PWM drive signal is provided by a SYNRAD UC-2000 laser controller and has a standard frequency of 5 kHz. The PWM drive signal can be gated with an external gate signal applied to the UC-2000 controller. Figure 5.5 shows how the laser output is controlled by the PWM drive signal. Note that this figure is only a schematic. Actual laser output follows the PWM drive signal with a rise/fall time constant of about 100 μs.

The laser beam passes through four zinc selenide (ZnSe) windows before it enters the cell. These ZnSe windows have anti-reflective (AR) coatings on both sides and have a nearly 100% transmission at a wavelength of 10.6 μm. The beam then leaves the cell and the 4 K shield though another two ZnSe windows and gets absorbed on a calcium fluoride (CaF_2) window installed on the 77 K shield (see Figure 3.1).

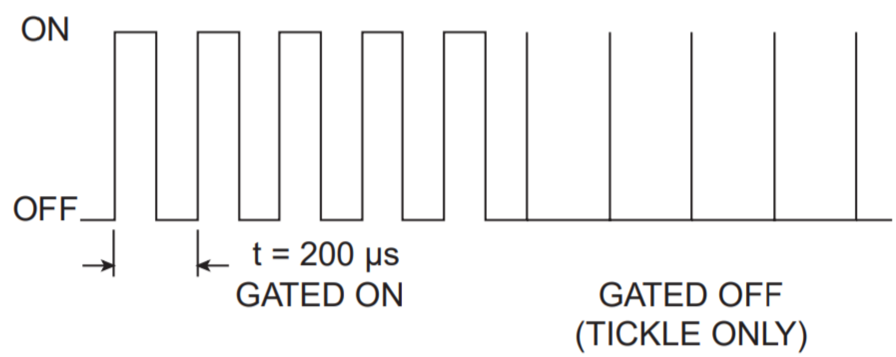

Figure 5.5: Laser output controlled by the drive signal from the controller, taken from the operation manual [138]. The PWM duty cycle is 50%. The tickle pulses are applied to the laser in order to reduce the optical rise time.

The output power of the laser was directly measured with an Ophir 20A laser power meter. The laser power was measured to have a fluctuation of 10%-15%. The laser approximately output 2 mJ per gate operation when the PWM duty cycle was 30% and a 1 msec wide gate signal was applied at a repetition rate of 100 msec.

In the experiments gate signals applied to the laser controller were also used to trigger the data acquisition device.

5.2.3 Thermometer

As detailed in section 4.3.6 of ref. [27], Wei *et al.* suspected that in the experiments there could be a deviation of the temperatures measured by the germanium thermometer (see section 3.1) due to the heating resulting from the CO_2 light or the black body radiation transmitted though the ZnSe windows. In order to better compare the measured mobilities, we performed a temperature calibration using the NEB mobility data measured by Wei *et al*. [27][136].

5.3 Experiments

In the experiments a sufficiently large negative dc voltage was applied to the field emission tip to produce a field emission current. Due to the high field near the tip, electrons extracted out of the tip would be trapped on vortices. Typically, the dc voltage on G2 was more negative with respect to that on G1, and no negative voltage pulse was applied to G1. Therefore, no free electrons could pass though G2. However, some electrons attached to vortices could still leak though G1 and G2. A light pulse was applied below G2 to knock off electrons. Knocked-off electrons then started to travel though the drift region and reached the collector. Current signals were detected at the collector.

5.3.1 Observation of Multiple Negative Ion Signals

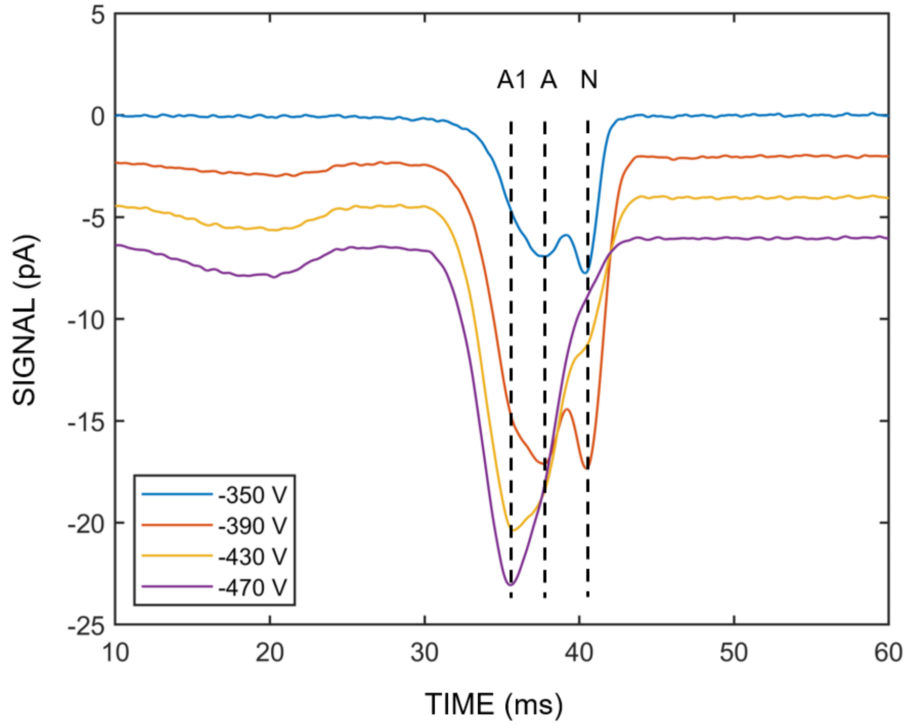

Figure 5.6: Current detected at the collector as a function of time. A light pulse of width 1 msec[34] from the CO_2 laser was applied at time zero. The curves are labelled by the voltage difference between the tip and G1. The temperature was 1.041 K. Data are offset for clarity.

In Figure 5.6 we show a dataset taken at 1.041 K. The cell pressure was 24 psi. The voltages on G1 and G2 were held constant at -295 V and -300 V, respectively. The voltage difference ΔV_{T-G1} between the tip and G1 was varied from -350 to -470 V. The drift field was 46.7 V/cm. The laser was pulsed for 1 msec at time zero with a PWM duty cycle of 30%. The signal from the normal electron bubbles is labelled as "N." Two other objects are seen before the arrival of the NEB. One has a mobility which matches that of the A ion seen by Wei *et al*. We still call it "A." The other one which we call "A1" was not seen in the

[34] A gate signal of width 1 msec was applied to the laser controller. See section 5.2.2 for details.

previous experiments[35]. The mobilities of A and A1 are approximately 8% and 14% higher than that of N, respectively. As shown in the figure, the N peak eventually disappears when the tip voltage becomes high.

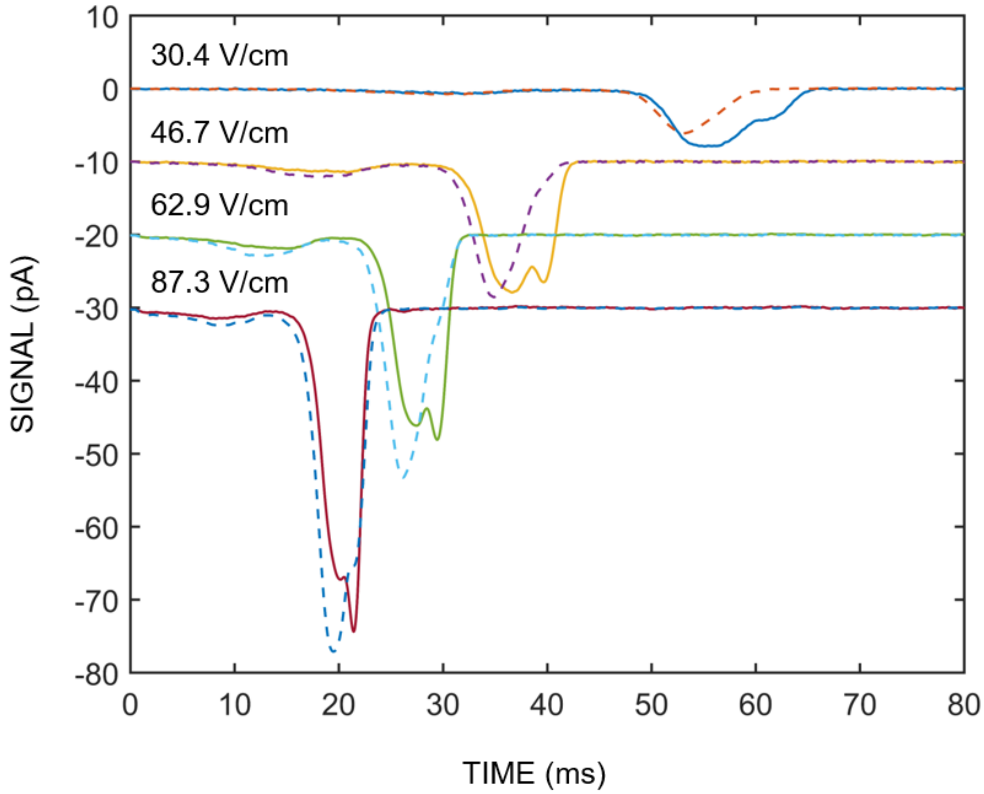

Figure 5.7: Current detected at the collector as a function of time. The curves are labelled by the drift field. Under each field two data traces were taken: the dashed line was taken at $\Delta V_{T-G1} = -470$ V, and the solid line was taken at $\Delta V_{T-G1} = -390$ V. The temperature was 1.037 K, and the cell pressure was 24 psi.

We then investigated the effect of varying the drift field. The data obtained under different drift fields are shown in Figure 5.7. The drift field was varied from 30.4 V/cm to 87.3 V/cm.

---

[35] A1 has a mobility that lies between that of the A and B ions measured by Wei *et al*.

The voltage on G1 was 5 V more positive with respect to that on G2. The laser was pulsed for 1 msec at time zero with a PWM duty cycle of 30%. All the peaks shift forwards and becomes stronger as the drift field increases. Assuming that A and A1 also started where the laser beam was directed, as N did, we plot the mobilities as a function of drift field in Figure 5.8. The mobilities of the A1, A and N ions do not vary significantly over the field range from 30.4 V/cm to 87.3 V/cm.

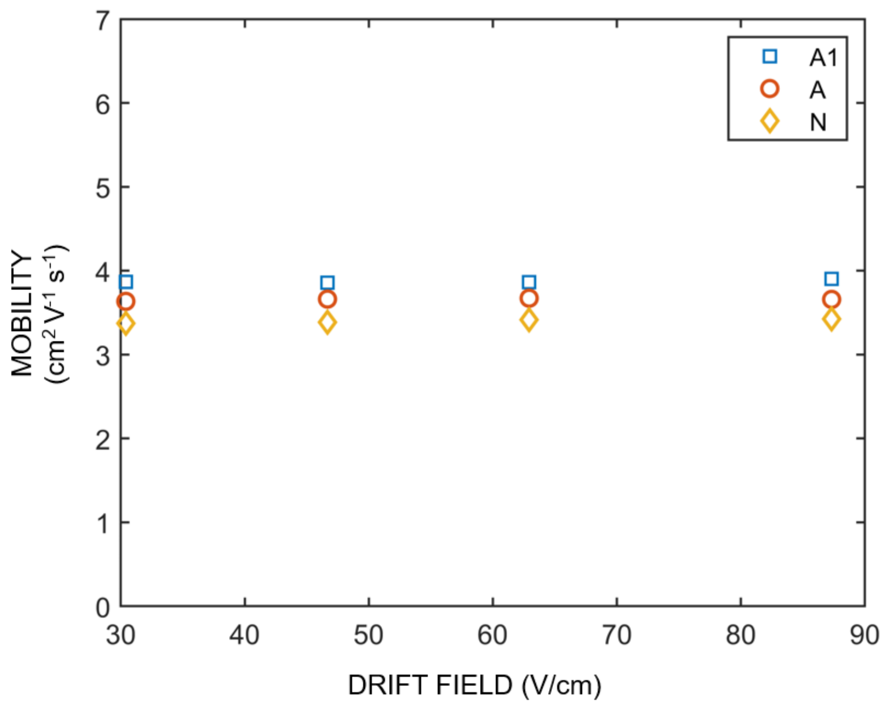

Figure 5.8: Mobilities of the A1, A and N ions as a function of drift field.

The mobilities were also measured at 24 psi over the temperature range from 1.026 to 1.29 K. The results are shown in Figure 5.9. Other experimental conditions, such as the tip voltage, the drift field, and the laser power, were adjusted in order to make the peaks well resolved[36]. The temperature dependence of the mobilities of A1, A and N is as expected, i.e., it could be well fitted to the equation $\mu \propto \exp(\Delta_{ion} / k_B T)$ with Δ_{ion} as the fitting parameter. The values of Δ_{ion} obtained for the A1, A and N ions were 8.52, 8.54 and 8.53 K, respectively. That the Δ_{ion} values obtained for different ions are fairly close to each other is consistent with the experiments of Wei *et al.* [27].

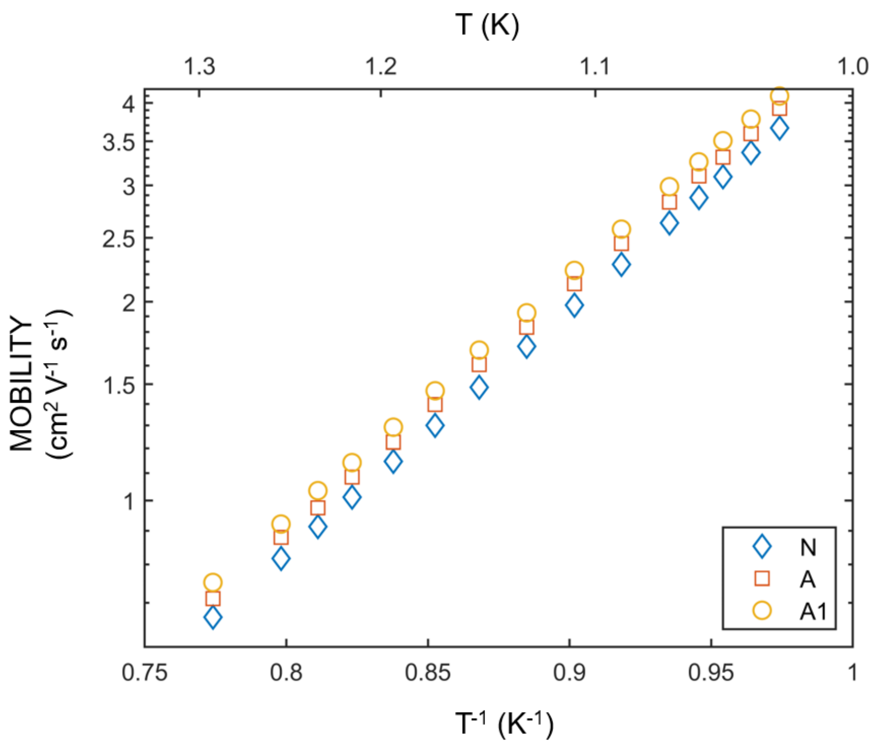

Figure 5.9: Mobilities of the A1, A and N ions as a function of temperature.

The variation of the laser power was studied as well, as shown in Figure 5.10. The laser was pulsed for 1 msec at time zero. The voltages on the tip, G1 and G2 were -950 V, -595

[36] The voltage on G1 was always 5 volts more positive with respect to that on G2.

V and -600 V, respectively. With this voltage setup only A and N were seen. Both signals become bigger as the laser power increases.

Note that in this run the 1 MΩ resistor between G2 and H1 was removed[37]; see Figure 3.3. This change was made in order to independently control the voltages on G2 and H1. In all the measurements described above, G2 and H1 were operated as if the 1 MΩ resistor was still installed, i.e., the voltage difference between G2 and H1 was equal to that between H1 and H2.

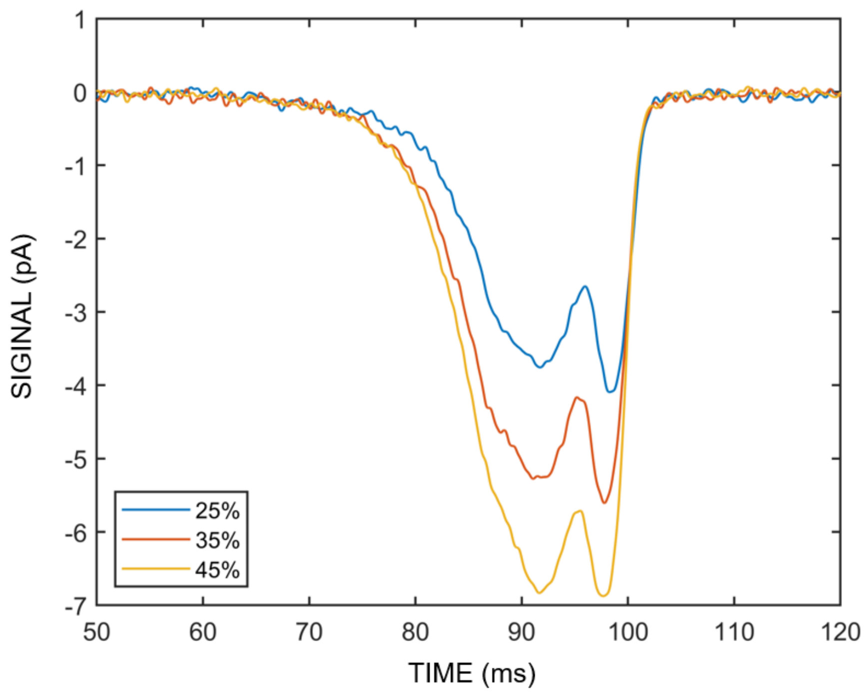

Figure 5.10: Current detected at the collector as a function of time. The temperature was 1.29 K, and the cell pressure was 24 psi. The drift field was 95.4 V/cm. The curves are labelled by the percent PWM duty cycle of the laser.

[37] The other four resistors were unchanged.

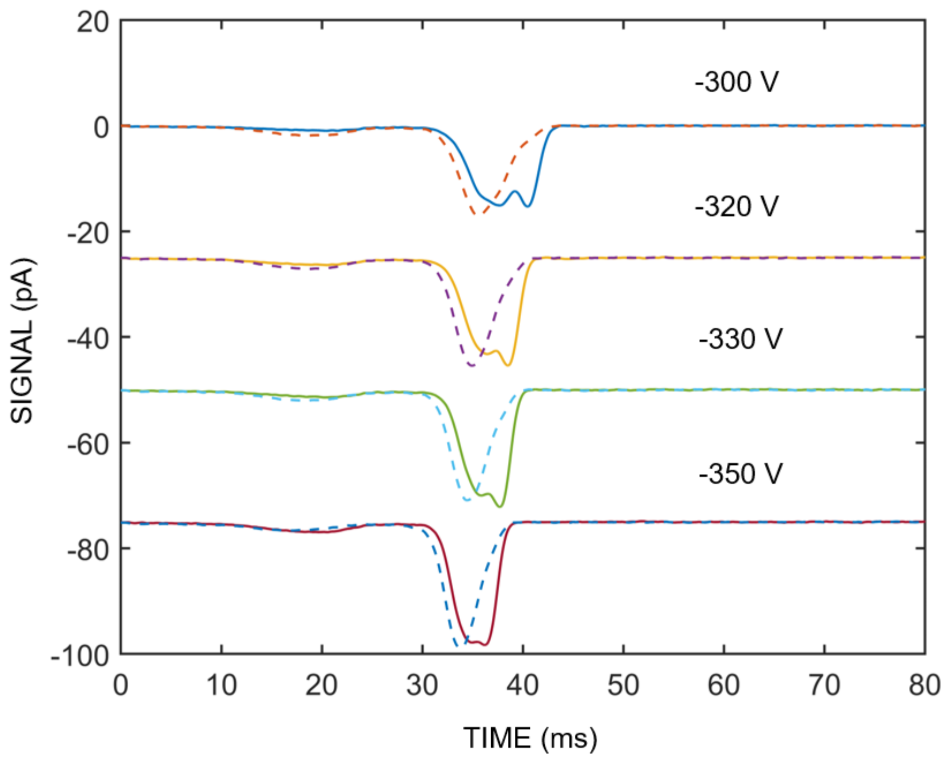

Figure 5.11: Current detected at the collector as a function of time. The curves are labelled by the voltage on G2. At each voltage, two traces were taken. The dashed trace was taken at a higher tip voltage in order to make the A1 peak strong. The solid trace was taken at a lower tip voltage in order to make the A and N peaks strong. The temperature was 1.041 K, and the cell pressure was 24 psi. The curves are offset for clarity.

As previously mentioned in section 5.1, it has been proposed that the multiple peaks in the measured signal could arise from normal electron bubbles starting at different locations in the drift region. Assuming this is the case, the A and A1 ions are supposed to start at approximately 0.75 and 0.48 cm above the homogenizer H1[38], respectively. Then a very good test on this proposal can be made by varying the voltage on G2 while holding the voltage on H1 constant. This variation can make the fields above and below H1 different. Studying

[38] N is supposed to start at approximately 1.18 cm above H1.

how the transit time varies with the voltage on G2 can provide useful information on where these ions start.

Ion N			
V_{G2} (Volts)	$t_m / t_m(V_{G2} = -300\text{ V})$	$t_{cal}^{I} / t_{cal}^{I}(V_{G2} = -300\text{ V})$	$t_{cal}^{II} / t_{cal}^{II}(V_{G2} = -300\text{ V})$
-300	1	1	1
-320	0.951	0.954	0.946
-330	0.93	0.938	0.925
-350	0.892	0.916	0.889
Ion A			
V_{G2} (Volts)	$t_m / t_m(V_{G2} = -300\text{ V})$	$t_{cal}^{I} / t_{cal}^{I}(V_{G2} = -300\text{ V})$	$t_{cal}^{II} / t_{cal}^{II}(V_{G2} = -300\text{ V})$
-300	1	1	1
-320	0.965	0.968	0.953
-330	0.947	0.958	0.934
-350	0.909	0.943	0.902
Ion A1			
V_{G2} (Volts)	$t_m / t_m(V_{G2} = -300\text{ V})$	$t_{cal}^{I} / t_{cal}^{I}(V_{G2} = -300\text{ V})$	$t_{cal}^{II} / t_{cal}^{II}(V_{G2} = -300\text{ V})$
-300	1	1	1
-320	0.982	0.979	0.957
-330	0.968	0.972	0.940
-350	0.949	0.962	0.912

Table 5.1: Measured and calculated relative transit times as a function of voltage V_{G2} on G2. The values at $V_{G2} = -300\text{ V}$ are normalized to unity for the convenience of comparison. The t_m values are from measurements. The t_{cal}^{I} values are from calculations using Equation (5.1), and the t_{cal}^{II} values are from calculations using Equation (5.2).

In Figure 5.11 we show the results of the test. The laser was pulsed for 1 msec at time zero, and the PWM duty cycle was 30%. The voltage on H1 was held constant at -240 V. The voltage on G2 was varied from -300 V[39] to -350 V. The voltage on G1 was held at 5 volts more positive with respect to that on G2. The tip voltage was adjusted in order to see strong

[39] Note that the fields below and above H1 were equal when the voltage on G2 was -300 V.

signals from different peaks. We can see in the figure that all the peaks shift forward as the amplitude of the voltage on G2 increases. This is as expected because increasing the voltage on G2 would increase both the fields above and below H1.

In Table 5.1 we show the measured transit times as a function of voltage V_{G2} on G2. The variation of transit time with V_{G2} is different for A1, A and N. This appears to support the idea that these ions started at different locations in the drift region. Then we calculate the transit time. As previously mentioned, varying V_{G2} affect not only the field between G2 and H1 but also the field below H1. Here we take two simple approaches to calculate the transit time by using the voltages on G2, H1, H2 and F. The first approach (I) is given as

$$t_{cal}^{I} = \frac{d_{\text{ion-H1}} \cdot d_{\text{G2-H1}}}{\left|V_{\mathrm{G2}} - V_{\mathrm{H1}}\right|} + \frac{d_{\text{H1-F}}^{\ 2}}{\left|V_{\mathrm{H1}} - V_{\mathrm{F}}\right|} \tag{5.1}$$

where $d_{\text{ion-H1}}$ is the distance between H1 and the starting position of the ion of interest, $d_{\text{G2-H1}}$ is the distance between G2 and H1, and $d_{\text{H1-F}}$ is the distance between H1 and F. This equation simply assumes that V_{G2} has no effect on the field below H1. Another approach (II) is given by the following equation

$$t_{cal}^{II} = \frac{d_{\text{ion-H2}} \cdot d_{\text{G2-H2}}}{\left|V_{\mathrm{G2}} - V_{\mathrm{H2}}\right|} + \frac{d_{\text{H2-F}}^{\ 2}}{\left|V_{\mathrm{H2}} - V_{\mathrm{F}}\right|} \tag{5.2}$$

where $d_{\text{ion-H2}}$ is the distance between H2 and the starting position of the ion of interest, $d_{\text{G2-H2}}$ is the distance between G2 and H2, and $d_{\text{H2-F}}$ is the distance between H2 and F. Equation (5.2) takes the field in the region between G2 and H2 as an average field determined by voltages V_{G2} and V_{H2}. It also assumes that the field below H2 is independent of

V_{G2}. The calculated values using these two approaches are also given in Table 5.1. Of course, both approaches only give approximations of the transit time. However, they still give results that are in reasonable agreement with the measured values.

To conclude, the test of varying the voltage on G2 appears to make preferable the idea that A1 and A were just normal electron bubbles starting at different locations. Wei *et al*. made similar tests in previous experiments [25]. However, they observed a completely different set of peaks when they made these tests, which makes it difficult for us to make a comparison.

5.3.2 Effects of Changes in Tip Voltages and G1-G2 Fields

In a later run, a new field emission tip was used. This new tip was still placed at 0.15 cm above G1. However, we failed to see the A ion this time[40]. The reason why this happened is not clear. Figure 5.12 shows a detailed investigation of varying the tip voltage. The voltages on G1 and G2 were held constant at -295 V and -300 V, respectively. The tip voltage was varied from -745 to -945 V. The drift field was 46.7 V/cm. The laser was pulsed for 1 msec at time zero, and the PWM duty cycle was 30%. Only A1 and N are seen in the signals. As the tip voltage was increased, the amplitude of the N peak increased first and then decreased. However, it did not disappear as shown in Figure 5.6. The A1 peak followed the same trend. At higher voltages the N peak became weaker than the A1 peak.

[40] The laser beam position was found to have a significant effect on the signal. We did try to change the beam position to reproduce A, but without success.

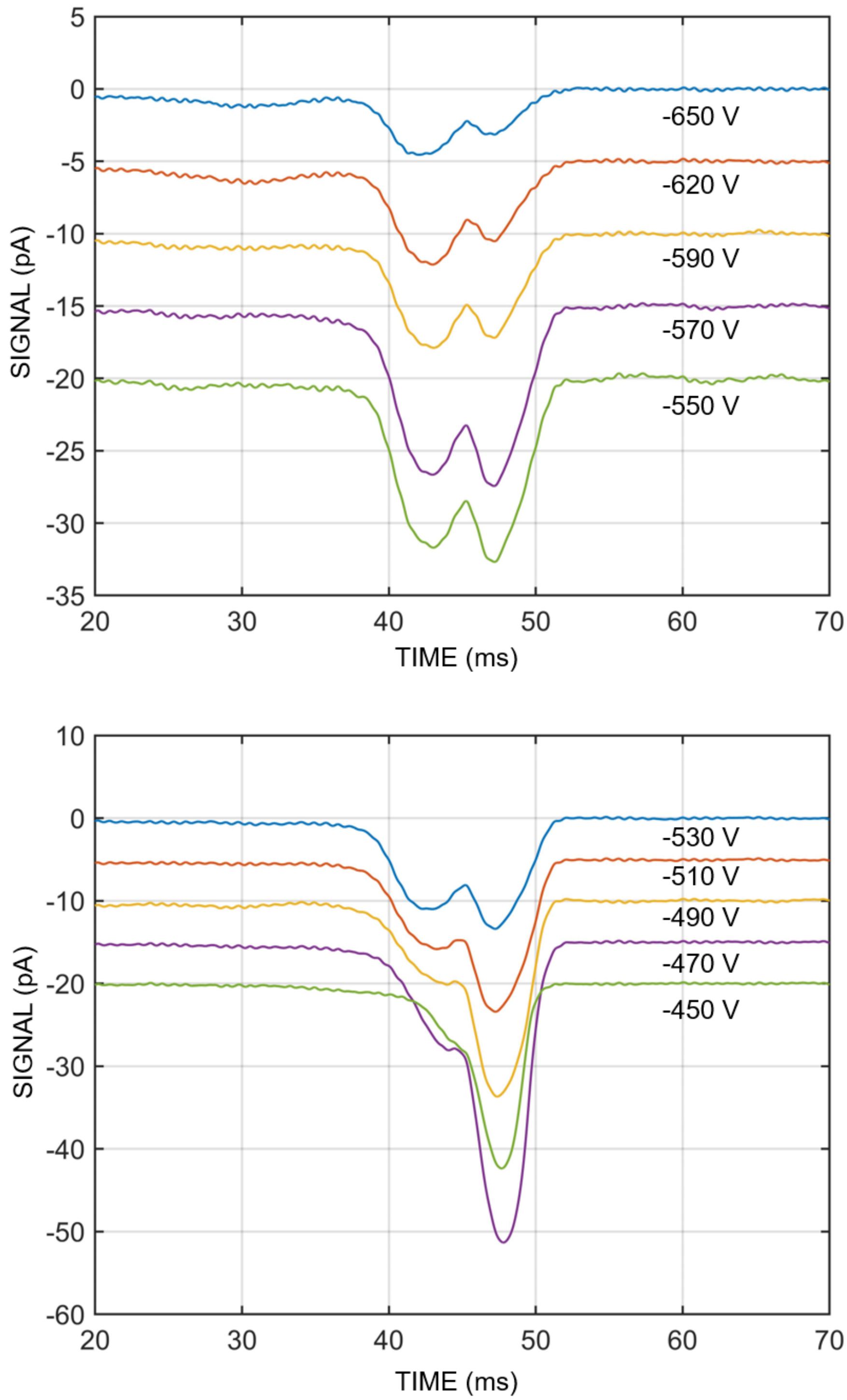

Figure 5.12: Current detected at the collector as a function of time. The curves are labelled by the voltage difference between the tip and G1. The temperature was 1.062 K, and the cell pressure was 24 psi. The curves are offset for clarity.

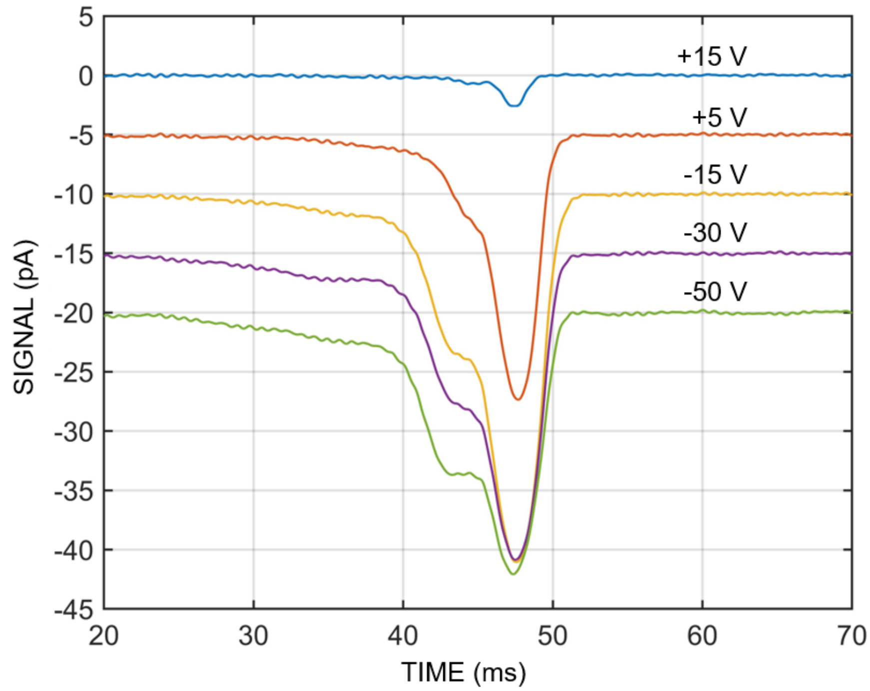

Figure 5.13: Current detected at the collector as a function of time. The curves are labelled by the voltage difference between G1 and G2. The positive sign denotes that the voltage on G1 is more positive with respect to that on G2. The temperature was 1.062 K, and the cell pressure was 24 psi. ΔV_{T-G1} was -450 V.

We also studied the effect of varying the field between G1 and G2. The results are shown in Figure 5.13. The voltage on G2 was held constant at -300 V, and the drift field was 46.7 V/cm. The voltage difference ΔV_{T-G1} between the tip and G1 was kept constant at -450 V. When the voltage difference $\Delta V_{\mathrm{G1-G2}}$ between G1 and G2 was changed from +15 V to -50 V, the N peak first became stronger and then became weaker. The A1 signal was only shown as a “shoulder”. But it did become more apparent when the voltage difference between G1 and G2 was negative. Figure 5.14 shows another dataset taken at

$\Delta V_{T-G1} = -650$ V . One can clearly see that the A1 peak shifted forward as $\Delta V_{\mathrm{G1-G2}}$ changed from +5 V to -15 V. The reason for this is not clear.

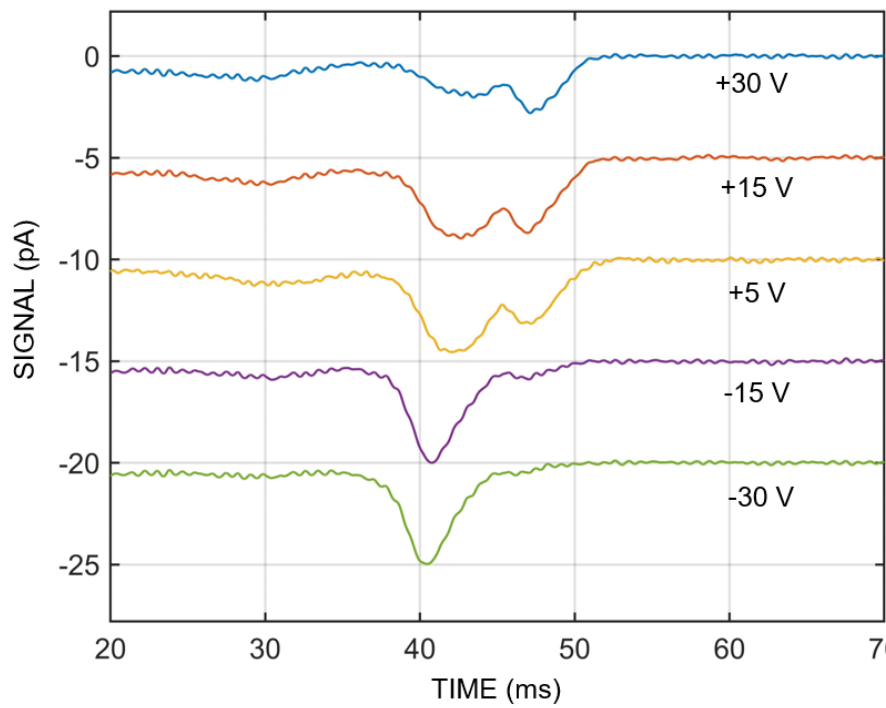

Figure 5.14: Current detected at the collector as a function of time. The curves are labelled by the voltage difference $\Delta V_{\mathrm{G1-G2}}$ between G1 and G2. The positive sign denotes that the voltage on G1 is more positive with respect to that on G2. The temperature was 1.062 K, and the cell pressure was 24 psi. ΔV_{T-G1} was -650 V.

The disappearance of the N signal at $\Delta V_{\mathrm{G1-G2}} = -30$ V in Figure 5.14 might be because electron bubbles trapped on vortices were all held between G1 and G2. Therefore, in the drift region there was nothing for the light to knocked off. However, it is still difficult to understand why the A1 peak was still there.

5.4 Discussion

In this chapter we have reported on our experiments using CO_2 laser to excite electron bubbles from the 1S state to the 1P state. In the experiments we have observed two different peaks/objects in addition to the N peak. The amplitudes of these peaks depend on the experimental conditions in a complicated way. We summarize some principal findings as follows:

(a) These peaks appear before the N peak.

(b) The species of objects seen in the experiments are not consistent. The objects we saw in different runs are not the same. In addition, the objects seen by us are different from those seen by Wei *et al*.

(c) The temperature dependence of the mobility of these objects is almost the same as that of the normal electron bubbles.

(d) The transit time variation with voltage on G2 is smaller for these objects than for the N peak. This was found in the measurements made by varying the voltage on G2 while holding the voltage on H1 constant.

(e) In addition to these peaks, there is a broad pulse at early times. See, for example, Figure 5.6. We found in the experiments that this broad pulse did not have a consistent transit time.

We now discuss some possible explanations. The first two possibilities have been considered by Wei *et* al. [25][136].

I. *Fission Theory*. When normal electron bubbles are excited from 1S to 1P, they could break into smaller bubbles with higher mobilities. However, if this was what happened, bubbles would be supposed to break in a specific way, i.e., break into two equal parts. Then (c) and (e) listed above cannot be explained. In addition, only one peak in addition to the N peak would have been seen if this was the case. But we were able to see two. Wei *et al*. were even able to see more than two.

II. *Electrons starting at different locations.* It is possible that vortices are distributed over the drift region. Then the CO_2 light could reach lower places by scattering and knock off NEBs trapped there. This idea may explain the inconsistency of the ion species seen in the experiments. And it also agrees with (c) and (e). But the difficulty is that there must be some local maximums in the vortex distribution for discrete peaks to appear in the measured signal. One would expect these local maximums would correlate to some special geometry of the cell, such as the edge of a homogenizer disk and a wire grid. However, A1 and A would have to start at a distance above the homogenizer H1. A future work to investigate this idea could be inserting a focusing lens into the optical waveguide to focus the light on a specific spot and then investigating the change in the signal.

III. *New species produced by the light*. Obviously, bubbles of 1P state have a too-short lifetime and thus cannot make any contribution to the signal. Could the CO_2 light knock some impurities off the wall of the cell? It is not clear whether the CO_2 laser would be able to do this. Perhaps it might be possible with a series of light pulses. But this does not explain why different objects are observed in different runs. One may also consider whether the light could break a large charged vortex tangle into small charged vortex rings. These rings are possible to be multiply charged. Then there could be several different objects. The difficulty is that the drift field in our experiments is much too low to make the charged rings stable. In addition, the drift velocity of a charged vortex ring is not supposed to be proportional to the drift field.

Inspired by the present experiment, we would like to discuss another possibility for the future work. It would be interesting to measure the capture cross-section of negative ions by vortex lines in superfluid helium. The capture cross-section is dependent on the ion radius. Thus, the results of cross-section measurements may tell whether the objects seen in the CO_2 laser experiments are normal electron bubbles or not. It may also provide a good test to backgrounds A and B discussed in Chapter 4. For bubbles containing a fraction F of the electron wave function, the capture cross-section should also be a function of F. The capture cross-section could be measured by the ion current attenuation due to vortices, The attenuation is given by $\exp(-L\sigma_{ion}x)$, where σ_{ion} is the capture cross-section (in cm), L is the vortex line density (in cm^{-2}), and x is the distance the ions travel though vortices.

The stochastic theory of ion capture by quantized vortex lines was developed by Donnelly and Roberts [139]. The ion capture cross-section at temperature T and an electric field of E is given by

$$\sigma_{ion} = \pi r_E (1-a)\left[\frac{I_0\left(d/r_E\right)}{K_0\left(d/r_E\right)} + 2\sum_{n=1}^{\infty}(-1)^n \frac{I_n\left(d/r_E\right)}{K_n\left(d/r_E\right)}\right] \tag{5.3}$$

where I_n and K_n are the modified Bessel functions of the first and second kind and $r_E = \dfrac{2k_B T}{eE}$. According to Donnelly and Roberts, the value of d could be estimated by

$$d = \left(\frac{4\rho_s R_{ion}{}^3 \kappa^2}{eE} \right)^{1/3} \tag{5.4}$$

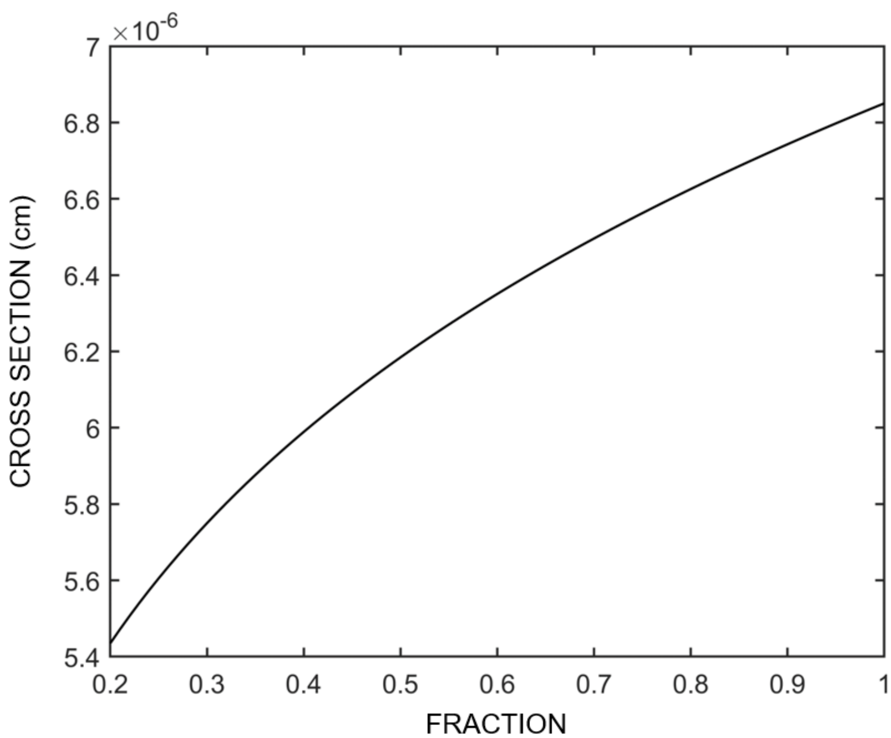

Figure 5.15: Capture cross-section as a function of F calculated from Equations (5.3) and (5.4).

where R_{ion} is the ion radius, ρ_s is the superfluid density, and κ is the circulation h / M_{He}. Note that Equations (5.3) and (5.4) are not supposed to give accurate results at temperatures below 1.3 K or above 1.6 K [140][141]. For a bubble containing a fraction F of the electron wave function, we take the ion radius to be $R_{ion} = F^{1/4} R_{NEB}$, where R_{NEB} is the radius of normal electron bubbles. Previous capture experiments [140][141] for NEBs showed that Equation (5.3) was in reasonable agreement with the measurements when R_{NEB} was taken to be 16 Å. The parameter $(1-a)$ was taken to be 0.48 [141]. At 1.3 K and a field of 50 V/cm, we show the calculated capture cross-section as a function of F in Figure 5.15. For the capture experiment to work, a method to generate vortices in our time-of-flight cell is needed. We would like to mention that people have successfully generated vortices in a time-of-flight cell in superfluid helium by means of ultrasonic sounds [142][143].

Bibliography

[1] J. Wilks, *The Properties of Liquid and Solid Helium*, Clarendon Press, Oxford (1967).

[2] R. J. Donnelly and C. F. Barenghi, J. Phys. Chem. Ref. Data **27**, 1217 (1998).

[3] L. Landau, J. Phys, U.S.S.R. **5**, 71 (1941); **11**, 91 (1947); **8**, 1 (1949).

[4] L. Landau, Phys. Rev. **60**, 356 (1941); **75**, 884 (1949).

[5] D. G. Henshaw and A. D. B. Woods, Phys. Rev. **121**, 1266 (1961).

[6] R. A. Cowley and A. D. B. Woods, Can. J. Phys. **49**, 177 (1971).

[7] R. A. Ferrell, Phys. Rev. **108**, 167 (1957).

[8] G. Careri, F. Scaramuzzi, and J. O. Thomson, Nuovo Cimento **13**, 186 (1959); G. Careri, U. Fasoli, and F. S. Gaeta, Nuovo Cimento **15** 774 (1960).

[9] W. T. Sommer, Phys. Rev. Lett. **12**, 271 (1964).

[10] K. Atkins, Phys. Rev. **116**, 1339 (1959).

[11] L. Meyer and F. Reif, Phys. Rev. **110**, 279 (1958).

[12] L. Meyer and F. Reif, Phys. Rev. Lett. **5**, 1 (1960).

[13] F. Reif and L. Meyer, Phys. Rev. **119**, 1164 (1960).

[14] K. W. Schwarz, Phys. Rev. A **6**, 837 (1972).

[15] G. Baym, R. G. Barrera, and C. J. Pethick, Phys. Rev. Letters **22**, 20 (1969); H. Barrera and G. Baym, Phys. Rev. A **6**, 1558 (1972).

[16] C. S. M. Doake and P. W. F. Gribbon, Phys. Lett. **30A**, 251 (1969).

[17] S. Cunsolo, Nuovo Cimento **21**, 76 (1961).

[18] G. G. Ihas and T. M. J. Sanders, Phys. Rev. Lett. **27**, 383 (1971).

[19] G. G. Ihas, T. M. Sanders, in *Proceedings of the 13th International Conference on Low Temperature Physics*, vol. 1, ed. by K. D. Timmerhaus, W. J. O'Sullivan, E. F. Hammel (Plenum, New York, 1972), p. 477.

[20] G. G. Ihas, *Exotic Ions in Liquid Helium*, Ph.D. thesis, Univ. Michigan, USA (1971).

[21] V. L. Eden and P. V. E. McClintock, Phys. Lett. **102A**, 197 (1984).

[22] V. L. Eden and P. V. E. McClintock in *75th Jubilee Conference on Liquid 4Helium*, ed. by J. G. M. Armitage (World Scientific, Singapore, 1983), p. 194

[23] P. V. E. McClintock, R. M. Bowley, in *Progress in Low Temperature Physics*, vol. 14, ed. by W. P. Halperin (North Holland, Amsterdam, 1995), p. 1

[24] W. Wei, Z.-L. Xie, Y. Yang, G. M. Seidel, and H. J. Maris, Journal of Physics:Conference Series **568**, 012011 (2014).

[25] W. Wei, Z. Xie, L. N. Cooper, G. M. Seidel, and H. J. Maris, J. Low Temp. Phys. **178**, 78 (2015).

[26] W. Wei, *Studies of the Fast and Exotic Ions in Superfluid Helium-4*, Ph.D. thesis, Brown University, 2012.

[27] Z. Xie, *Experimental Investigation of the Exotic Negative Ions in Superfluid Helium-4*, Ph.D. thesis, Brown University, 2016.

[28] Y. Xing and H. J. Maris, J. Low Temp. Phys. **202**, 399 (2021).

[29] A. P. Volodin, M. S. Khaikin, and V. S. Edel'man, JETP Lett. **26**, 543 (1977).

[30] U. Albrecht and P. Leiderer, Europhys. Lett. **3**, 705 (1987).

[31] U. Albrecht and P. Leiderer, J. Low Temp. Phys. **86**, 131 (1992).

[32] J. Fang, A. E. Dementyev, J. Tempere, and I. F. Silvera, Rev. Sci. Instrum. **80**, 043901 (2009).

[33] N. Yadav, P. K. Rath, Z. Xie, Y. Huang, and A. Ghosh, J. Low. Temp. Phys. **201**, 658 (2020).

[34] N. Yadav, Y. Huang, and A. Ghosh, Phys. Rev. B **102**, 054509 (2020).

[35] V. B. Shikin, JETP Lett. **27**, 39 (1978).

[36] M. M. Salomaa and G. A. Williams, Phys. Scr. **T4**, 204 (1983).

[37] D. L. Dexter and W. B. Fowler, Phys. Rev. **183**, 307 (1969).

[38] H. J. Maris, J. Low Temp. Phys. **132**, 77 (2003).

[39] K. W. K. Shung and F. L. Lin, Phys. Rev. B **45**, 7491 (1992).

[40] W. Wei, Z. Xie and H. J. Maris, Phys. Rev. B **89**, 064504 (2014).

[41] W. Wei, Z.-L. Xie, and H. J. Maris, J. Phys.: Conf. Ser. **568**, 012010 (2014).

[42] N. Yadav, P. Sen and A. Ghosh, Sci. Adv. **7**, eabi7128 (2021).

[43] P. Roche, G. Deville, N. J. Appleyard, and F. I. B. Williams, J. Low Temp. Phys. **106**, 565 (1997).

[44] L. Glasser and A. G. Every, J. Phys. A **25**, 2473 (1992).

[45] T. Erber and G. M. Hockney, J. Appl. Phys A **24**, L1369 (1991).

[46] S. Sirisky, Y. Xing, G. M. Seidel and H. J. Maris, J. Low Temp. Phys. **201**, 122 (2020).

[47] S. Sirisky, Y. Xing, G. M. Seidel and H. J. Maris, J. Low Temp. Phys. **201**, 114 (2020).

[48] S. Sirisky, *Studies of Negative and Positive Charge Carriers in Superfluid Helium-4*, Ph.D. thesis, Brown University, 2019.

[49] W. Wei, Z. Xie, G. M. Seidel, and H. J. Maris, J. Phys.: Conf. Ser. **400**, 012042 (2012).

[50] B. Brody, Phys. Rev. B **11**, 170 (1975).

[51] K. W. Schwarz, Phys. Rev. A **6**, 1958 (1972).

[52] G. G. Ihas and T. M. Sanders, Phys. Lett. **31A**, 502 (1970).

[53] W. W. Johnson and W. I. Glaberson, Phys. Rev. Lett. **29**, 214 (1972).

[54] W. I. Glaberson and W. W. Johnson, J. Low Temp. Phys. **20**, 313 (1975).

[55] P. W. Alexander, C. N. Barber, P. V. E. McClintock, and G. R. Pickett, Phys. Rev. Lett. **39,** 1544 (1977).

[56] P. W. Alexander and G. R. Pickett, J. Low Temp. Phys. **34**, 695 (1979).

[57] P. R. Roach, J. B. Ketterson, and P. D. Roach, J. Low Temp. Phys. **34**, 169 (1979).

[58] V. Efimov, K. Obara, D. Ueno, Y. Yamaguchi, and H. Ishimoto, J. Low Temp. Phys. **26**, 121 (2002).

[59] D. Mateo and J. Eloranta, J. Phys. Chem. **118**, 6407 (2014).

[60] J. Poitrenaud and F. I. B. Williams, Phys. Rev. Lett. **29**, 1230 (1972).

[61] C. D. H. Williams, P. C. Hendry, and P. V. E. McClintock, Phys. Rev. Lett. **60**, 865 (1988).

[62] C. M. Muirhead, W. F. Vinen, and R. J. Donnelly, Philos. Trans. Roy. Soc. London, A **311**, 433 (1984), and references therein.

[63] N. M. Lawandy, Phys. Lett. A **383**, 3143 (2019).

[64] V. Elser, J. Low Temp. Phys. **180**, 363 (2015).

[65] A. G. Khrapak and S. Y. Bronin, JETP Lett. **105**, 797 (2017).

[66] E. Parks and R. J. Donnelly, Phys. Rev. Lett. **16**, 45 (1966).

[67] H. J. Maris, J. Low Temp. Phys. **120**, 173 (2000).

[68] W. Wei, Z. Xie, L. N. Cooper and H. J. Maris, J. Low Temp. Phys. **185**, 313 (2016).

[69] G. M. Seidel, T. M. Ito, A. Ghosh and B. Sethumadhavan, Phys. Rev. C **89**, 025808 (2014).

[70] D. G. Onn and M. Silver, Phys Rev. **183**, 295 (1969).

[71] A. G. Khrapak and W. F. Schmidt, Low Temp. Phys. **37**, 387 (2011).

[72] A. G. Khrapak and W. F. Schmidt, Int. J. Mass. Spectrom. **277**, 236 (2008).

[73] Y. Xing, S. Sirisky, W. Wei, L. N. Cooper and H. J. Maris, J. Low Temp. Phys. **207**, 11 (2022).

[74] Y. Xing and H. J. Maris, J. Low Temp. Phys. **201**, 634 (2020).

[75] H. Putnam, Phil. Sci. **28**, 234 (1961).Ito

[76] H. Putnam, Phil. Sci. **31**, 1 (1964).

[77] J. S. Bell, Phys. World **3**, 33 (1990).

[78] H. Margenau, E. P. Wigner, Phil. Sci. **29**, 292 (1962).

[79] E. P. Wigner, Am. J. Phys. **31**, 6 (1963).

[80] H. Margenau, E. P. Wigner, Phil. Sci. **31**, 7 (1964).

[81] L. N. Cooper, D. Van Vechten, Am. J. Phys. **37**, 1212 (1969).

[82] L. N. Cooper, in *The Physicist's Conception of Nature*, ed. by J. Mehra (Reidel, Dordrecht-Holland, 1973), p. 668.

[83] L. N. Cooper, Proc. Am. Phil. Soc. **120**, 37 (1976).

[84] N. D. Mermin, Phys. Today **53**(7), 11 (2000).

[85] L. de Broglie, J. Phys. Radium **8**, 225 (1927).

[86] D. Bohm, Phys. Rev. **85**, 166–180 (1952).

[87] D. Bohm, Phys. Rev. **89**, 458 (1953).

[88] H. Everett, Rev. Mod. Phys. **29**, 454 (1957).

[89] G. C. Ghirardi, A. Rimini, T. Weber, Phys. Rev. D **34**, 470 (1986).

[90] H.-D. Zeh, Found. Phys. **B1**, 69 (1970).

[91] W. H. Zurek, Phys. Rev. D **24**, 1516 (1981).

[92] W. H. Zurek, Phys. Rev. D **26**, 1862 (1982).

[93] A. J. Leggett, Science **307**, 871 (2005).

[94] M. Jammer, *The current interpretation of wave mechanics* (Wiley, New York, 1974), pp. 115–117.

[95] A. Fine, *The Shaky Game: Einstein, Realism, and the Quantum Theory* (University of Chicago Press, Chicago, 1996).

[96] L. de Broglie, J. Phys. Radium **20**, 963 (1959).

[97] L. de Broglie, *The current interpretation of wave mechanics*, pp. 28–29 (Elsevier, Amsterdam, 1964).

[98] J. Gea-Banacloche, Am. J. Phys. **70**, 307 (2002).

[99] C. M. Bender, D. C. Brody, and B. K. Meister, Proc. Roy. Soc, A **461**, 733 (2005).

[100] S. K. Baek, S. D. Yi, and M. Kim, Phys. Rev. A **94**, 052124 (2016).

[101] T. Hayashi, T. Fujisawa, H. D. Cheong, Y. H. Jeong, and Y. Hirayama, Phys. Rev. Lett. **91**, 226804 (2003).

[102] J. R. Petta, A. C. Johnson, J. M. Taylor, E. A. Laird, A. Yacoby, M. D. Lukin, C. M. Marcus, M. P. Hanson, and A. C. Gossard, Science, **309,** 2180 (2005).

[103] J. P. Hernandez and M. Silver, Phys. Rev. **2** 1949 (1970) and J. P. Hernandez, Rev. Mod. Phys. **63**, 675 (1991).

[104] M. Rosenblit and J. Jortner, Phys. Rev. Lett. **75**, 4079 (1995), and J. Phys. Chem A **101**, 751 (1997).

[105] J. Eloranta and V. A. Apkarian, J. Chem. Phys. **117**, 10139 (2002).

[106] V. Elser, J. Low Temp. Phys. **123**, 7 (2001).

[107] A. I. M. Rae and W. F. Vinen, J. Low Temp. Phys. **123**, 1 (2001).

[108] R. Jackiw, C. Rebbi, and J. R. Schriefer, J. Low Temp. Phys. **122**, 587 (2001).

[109] B. Altschul and C. Rebbi, Phys. Rev. A **69**, 032111 (2004).

[110] D. Mateo, M. Pi, and M. Barranco, Phys. Rev. B **81**, 174510 (2010).

[111] G. Greenstein and A. G. Zajonc, *The Quantum Challenge*, (Jones and Bartlett, Boston, 2005).

[112] M. E. Muller, Ann. Math. Statist. **27**, 569 (1956).

[113] S. Redner, *A Guide to First-Passage Processes* (Cambridge University Press, Cambridge, 2001).

[114] M. J. Druyvesteyn and F. M. Penning, Rev. Mod. Phys. **12**, 88 (1940).

[115] E. M. Lifshitz and L. P. Pitaevskii, *Physical Kinetics* (Elsevier Science, Oxford, 1995).

[116] D. E. Golden and H. W. Bandel, Phys. Rev. **138**, A14 (1965).

[117] L. B. Lurio, T. A. Rabedeau, P. S. Pershan, I. F. Silvera, M. Deutsch, S. D. Kosowsky, and B. M. Ocko, Phys. Rev. B **48**, 9644 (1993).

[118] K. Penanen, M. Fokuto, R. K. Heilman, I. F. Silvera, and P. S. Pershan, Phys. Rev. B **62**, 9621 (2000).

[119] J. M. Marin, J. Boronat, and J. Casulleras, Phys. Rev. B **71**, 144518 (2005).

[120] L. D. Landau and I. M. Lifschitz, *Quantum Mechanics*, (Pergamon, Oxford, 1965), p. 79.

[121] M. W. Cole, Phys. Rev. A **1**, 1838 (1970).

[122] E. Cheng, M. W. Cole, and M. H. Cohen, Phys. Rev. B **50**, 1136 (1994); Erratum Phys. Rev. B **50**, 16134 (1994).

[123] N. Ishida, J. Kikuchi, and T. Doke, Jpn. J. Appl. Phys. **31**, 1465 (1992).

[124] T. M. Ito and G. M. Seidel, Phys. Rev. C **88**, 025805 (2013).

[125] J. Classen, C.-K. Su, M. Mohazzab and H. J. Maris, Phys. Rev. **57**, 3000 (1998).

[126] D. Konstantinov and H. J. Maris, Phys. Rev. Lett., **90**, 025302 (2003).

[127] Z. Xie, W. Wei, Y. Yang and H. J. Maris, J. Exp. Theor. Phys. **146**, 1258 (2014).

[128] J. A. Northby and T. M. Sanders, Jr., Phys. Rev. Lett. **18**, 1184 (1967).

[129] J. A. Northby, Ph.D. thesis, University of Minnesota, 1966 (unpublished).

[130] C. L. Zipfel, Ph.D. thesis, University of Michigan, 1969 (unpublished).

[131] C. L. Zipfel and T. M. Sanders, in *Proceedings of the 11th International Conference on Low Temperature Physics*, edited by J. F. Allen, D. M. Finlayson, and D. M. McCall (St. Andrews University, St. Andrews, Scotland, 1969), p. 296.

[132] T. Miyakawa and D. L. Dexter, Phys. Rev. A **1**, 513 (1970).

[133] C. C. Grimes and G. Adams, Phys. Rev. B **41**, 6366 (1990).

[134] C. C. Grimes and G. Adams, Phys. Rev. B **45**, 2305 (1992).

[135] D. Mateo, D. Jin, M. Barranco, and M. Pi, J. Chem. Phys. **134**, 044507 (2011).

[136] W. Wei, Z.-L. Xie, G. M. Seidel and H. J. Maris, J. Low Temp. Phys. **175**, 70 (2014).

[137] K. Kawasaki, K. Tsukagoshi and K. Kono, J. Low Temp. Phys. **138**, 899 (2005).

[138] SYNRAD Series 48 Series Lasers Operator's Manual, Version 5.4, SYNRAD Inc.

[139] R. J. Donnelly and P. H. Roberts, Proc. Roy. Soc. A **312**, 519 (1969).

[140] D. J. Tanner, Phys. Rev. **152**, 121 (1966).

[141] R. M. Ostermeier and W. I. Glaberson, J. Low. Temp. Phys. **20**, 159 (1975).

[142] R. F. Carey, J. A. Rooney, and C. W. Smith, Phys. Lett. **65A**, 311 (1978).

[143] K. W. Schwarz and C. W. Smith, Phys. Lett. **82A**, 251 (1981).